Meso Mechanics and Peridynamic Modelling of Fibrous Through Thickness Reinforcement at High Deformation Rate

by

Hussein Hijazi

Department of Aeronautics
Imperial College London

This thesis is submitted for the degree of Doctor of Philosophy of Imperial College London

2019

Abstract

Numerically modelling Z-pinned laminates is an important step in developing damage tolerant structures using through thickness reinforcement such as Z-pins. This work is concerned with developing a reduced order model (ROM) capable of predicting the Z-pin bridging performance under mixed mode loading and at high deformation rates.

The ROM is derived using the peridynamic formulation of the solid mechanics equations of motion. For this purpose, rod and Timoshenko beam elements in peridynamic formulation were derived from first principles and validated against well established analytical results. The developed Timoshenko beam element is a non-linear element that accounts for moderate beam rotations.

The rod peridynamic element is used as the basis of the Z-pin ROM model for the case of pure mode I loading. Two models were considered; the first model includes all key stages of the Z-pin response under mode I loading, i.e. bonded, debonding and frictional pull-out stages. The second model ignores the bonded and debonding stages and only considers the frictional pull-out stage. Both models yielded excellent prediction capabilities at different loading rates especially in terms of the energy absorbed by the Z-pin. This matched the experimental observation that most of the energy is absorbed during the frictional pull-out stage of the Z-pin response.

The non-linear peridynamic beam element is used as the basis of the Z-pin ROM model for the general case of mixed mode loading. Three key external forces were considered under mixed mode loading; a lateral Winkler foundation type force and an axial sliding and snubbing frictional forces. Ruina's state based friction model was adopted to describe the rate depen-

dent behaviour of the sliding and snubbing frictional forces. The B-K failure criterion has been utilised to predict the fracture failure of the Z-pin. For this purpose, the energy release rate in peridynamic formulation has been developed. The resulting model had a number of parameters that needed to be defined.

The developed model was calibrated against a subset of experimental data obtained from the literature in order to define unknown model parameters. The calibrated model has been validated against a different subset of the experimental data. The model was able to predict the Z-pin bridging performance relatively accurately at different loading rates and mode mixities. More importantly, the model is very computationally efficient with a run time of the order of minutes using a non-optimised Matlab code that run on a desktop computer. This opens up the possibility of modelling Z-pinned laminates using a multi-scale approach where the ROM model is coupled with finite element packages to predict the performance of Z-pinned laminates.

Dedication

To my parents, Sam and Khadijeh, who have been a source of encouragement and inspiration to me throughout my life. A very special thank you for supporting me during my thesis and for the myriad of ways in which, throughout my life, you have actively supported me in my determination to find and realise my potential, and to make this contribution to our world.

Declaration

The work presented within this thesis is the author's own, unless referenced to the contrary in the text, and is the product of research carried out at Imperial College London. No part of this thesis has been submitted elsewhere for any other degree or qualification.

Copyright Declaration

The copyright of this thesis rests with the author. Unless otherwise indicated, its contents are licensed under a Creative Commons Attribution-Non Commercial 4.0 International Licence (CC BY-NC).

Under this licence, you may copy and redistribute the material in any medium or format. You may also create and distribute modified versions of the work. This is on the condition that: you credit the author and do not use it, or any derivative works, for a commercial purpose.

When reusing or sharing this work, ensure you make the licence terms clear to others by naming the licence and linking to the licence text. Where a work has been adapted, you should indicate that the work has been changed and describe those changes.

Please seek permission from the copyright holder for uses of this work that are not included in this licence or permitted under UK Copyright Law.

Acknowledgements

The work presented in this thesis was carried out under the "DYNAPIN" project, funded by EPSRC (grant number: EP/M015319/1), and involving a collaboration with Oxford University and the University of Bristol. The project was supported by Rolls-Royce, BAE and Hexcel. The author would like to gratefully acknowledge the department of Aeronautics at Imperial College for partly sponsoring this work and making this research possible.

I would like to express my deepest gratitude to Dr. Giuliano Allegri for his guidance and supervision during this project, for his constant support and invaluable expertise, for having been a role-model in terms of dedication, passion and hard-work (Meeting me in the office on multiple weekends!).

I would like to gratefully acknowledge the DYNAPIN family for their support during numerous meetings and discussions. I would like to thank Prof. Stephen Hallett, Prof. Nik Petrinic and Prof. Ivan partridge. In particular I would like to thank Dr. Hao Cui who provided the experimental data for the work conducted in this thesis. Also, Dr. Hao Cui spent valuable time listening to my interpretation of the data and provided useful comments.

I would like to express my gratitude to all my colleagues and friends from the Department of Aeronautics at Imperial College London who made the last three years an unforgettable and special period. In particular I would like to thank Karim, Francesco, Arturo, Pedro, and Norberto.

Above all, I would like to express my utmost gratitude for my family, Mum, dad, sister and brother and their families. They have shaped the person I am today and I owe them a great deal that I cannot find words to describe.

Lastly, I would like to acknowledge the contribution of caffeine and sugars as they helped me stay awake for long hours during many sleepless nights.

Contents

1 Introduction **18**
- 1.1 Background . . . 18
- 1.2 Through Thickness Reinforcement (TTR) . . . 20
- 1.3 Objective and Vision . . . 21

2 Literature Review **24**
- 2.1 Introduction . . . 24
- 2.2 Through Thickness Reinforcement Methods . . . 25
  - 2.2.1 Toughened Matrix . . . 26
  - 2.2.2 Interleaving . . . 28
  - 2.2.3 Stitching . . . 29
  - 2.2.4 Tufting . . . 30
  - 2.2.5 Z-pinning . . . 31
  - 2.2.6 3D Laminate Architecure . . . 32
  - 2.2.7 Summary . . . 33
- 2.3 Z-pinning - Comprehensive Review . . . 35
  - 2.3.1 Manufacturing Method . . . 35
  - 2.3.2 Microstructure of Z-pinned Laminates . . . 37
  - 2.3.3 Mechanical Behaviour of Z-pinned Composites . . . 39
  - 2.3.4 Z-pin Energy Absorption Mechanisms . . . 42
  - 2.3.5 Summary . . . 43
- 2.4 Z-pin Models . . . 45
  - 2.4.1 Analytical Models . . . 46
  - 2.4.2 Semi-Analytical Models . . . 47
  - 2.4.3 Numerical Models . . . 52
  - 2.4.4 Summary . . . 57
- 2.5 Conclusions . . . 58

3 Peridynamic Formulation and Validation **60**
3.1 Introduction . . . 60
3.2 Peridynamics - A Review . . . 62
3.3 Peridynamic Model Formulation . . . 67
3.3.1 Rod Formulation . . . 67
3.3.2 Non-linear Timoshenko Beam Formulation . . . 69
3.3.3 Numerical Stability . . . 78
3.4 Peridynamic Numerical Solution Considerations . . . 81
3.4.1 Initial and Boundary Condition Application . . . 82
3.4.2 Volume Correction . . . 83
3.4.3 Surface Correction . . . 84
3.4.4 Adaptive Dynamic Relaxation . . . 84
3.5 Peridynamic Validation . . . 85
3.5.1 Bar Under Uniformly Distributed Tensile Load . . . 85
3.5.2 Cantilever Beam Under Transverse Loading . . . 87
3.6 Summary . . . 89

4 Experimental Results **91**
4.1 Introduction . . . 91
4.2 The Experiment . . . 92
4.2.1 Coupon Configuration . . . 92
4.2.2 Test Set-up . . . 94
4.2.3 Inertia Effects . . . 95
4.3 Results and Discussion . . . 97
4.3.1 Mode I . . . 97
4.3.2 Mode II . . . 103
4.3.3 Mixed Mode . . . 106
4.3.4 Energy Absorbed . . . 113
4.4 Summary . . . 116
4.4.1 Test Matrix Summary . . . 119

5 Mode I Z-pin Bridging Model **120**
5.1 Introduction . . . 120
5.2 Model Formulation . . . 121
5.2.1 Problem Description . . . 121
5.2.2 Governing Equation . . . 123
5.2.3 Lateral Foundation and Frictional Forces . . . 124
5.2.4 Numerical Stability . . . 128

5.2.5 Failure Criterion . . . 131
5.2.6 Convergence and Boundary Condition . . . 132
5.3 Model Calibration . . . 133
5.4 Results . . . 134
5.4.1 Model 1: Including the Debonding Stage . . . 135
5.4.2 Model 2: Ignoring the Debonding Stage . . . 137
5.5 Discussion . . . 140
5.6 Summary . . . 142

6 Mixed Mode Z-pin Bridging Model 144
6.1 Introduction . . . 144
6.2 Model Formulation . . . 145
6.2.1 Problem Description . . . 145
6.2.2 Governing Equation . . . 148
6.2.3 External Forces Model . . . 150
6.2.4 Failure Model . . . 154
6.2.5 Modelling Variability . . . 157
6.2.6 Numerical Considerations . . . 158
6.3 Model Calibration . . . 159
6.4 Results and Discussions . . . 161
6.4.1 Deterministic Model Results . . . 163
6.4.2 Transition Region Non-Deterministic Model Results . . . 169
6.4.3 Energy Dissipation . . . 172
6.4.4 Model Run Time . . . 174
6.5 Summary . . . 175

7 Conclusion and Future Work 177
7.1 Summary . . . 177
7.1.1 Thesis Motivation . . . 177
7.1.2 Peridynamic Formulation and Validation . . . 177
7.1.3 Experimental Results . . . 178
7.1.4 Mode I Model . . . 178
7.1.5 Mixed Mode Model . . . 179
7.2 Overall Conclusion . . . 180
7.3 Future Work . . . 180
7.3.1 Numerical . . . 180
7.3.2 Experimental . . . 181

Appendices **183**

A Classical Timoshenko Beam With Small Rotation **184**

B Riemann's Sum Approximation of Peridynamic Integrals **187**

C Peridynamic Force at a Point **188**

List of Figures

2.1 Impact damaged laminate showing delamination forming at ply interfaces in the through thickness direction, obtained from Ref. [1] . . . 26
2.2 Secondary phase toughening particles in matrix, obtained from Ref. [1] . . . 27
2.3 Delamination in AS4/PEEK material showing significant plastic flow, obtained from Ref. [2] . . . 27
2.4 Schematic illustration of interleaving, obtained from Ref. [3] . 28
2.5 Different Stitch Types, (a) lock stitch, (b) modified lock stitch and (c) chain stitch. Obtained from Ref. [4] . . . 29
2.6 Schematic illustration of (a) the sequential manufacturing steps to inserting a tuft and (b) of partial and full penetration. Adapted from [5] . . . 31
2.7 Z-pin inserted into prepreg laminate. Adapted from [6] . . . 32
2.8 GE Leap fan blade manufacture using 3D weaving in the preform configuration, obtained from Ref. [7] . . . 33
2.9 Illustration of UAZ insertion process. Obtained from Ref. [8] . 35
2.10 (a) Shows fibre waviness and resin rich zone around the Z-pin. (b) Shows the formation of resin channel at high areal density. Obtained from Ref. [6] . . . 37
2.11 Debonding of the Z-pin after curing. Obtained from Ref. [9] . 38
2.12 Schemaitc illustration of loading (a) with the nap and (b) against the nap. . . . 44
2.13 Effect of loading (a) "with the nap" and (b) "against the nap" on titanium Z-pin failure. Obtained from Ref. [10] . . . 44
2.14 (a) Laminate stack view (b) Showing fibre waviness in vicinity of resin pocket. Obtained from Ref. [11] . . . 53

3.1 Illustration of particle interaction in peridynamic theory. . . . 63

3.2 Illustration of pairwise interaction in (a) Bond-based peridynamics (b) Ordinary state-based peridynamics (c) Non-ordinary state based peridynamics. 64
3.3 A rod subject to distributed force p(z). The rod is aligned with the z-axis. 67
3.4 Deformation and force densities for a peridynamic beam. . . 70
3.5 Domain of interest is discretised into equal segments of length Δz with red material (collocation) points in the middle of each segment. Fictitious boundary layer (B_L) can be used to apply boundary condition. B_L has a length of r_h 82
3.6 Illustration for volume correction procedure. 83
3.7 Illustration of surface effect. The blue particle has full horizon interactions while the grey particle at the edge has half horizon interactions. In this case the horizon has a radius $r_h = 3\Delta z$. . 84
3.8 Cantilevered bar subject to uniformly distributed axial load. . 85
3.9 Comparison of peridynamic prediction and analytical results for a prismatic bar under uniformly distributed axial load. . . 87
3.10 Cantilever beam subject to tip load of P. 88
3.11 Comparison of peridynamic prediction and analytic results for a tip loaded beam. (a) Deflection and (b) Cross section rotation along the beam. 89

4.1 Coupon configuration and Z-pin distribution Ref. [12] 93
4.2 Test setup configuration at (a) quasi-static and (b)dynamic loading rate. Ref. [13] 95
4.3 Fixture used in (a) Mode I, (b) Mode II and (c) Mixed Mode Loading. Ref. [12, 13] 96
4.4 The quasi-static bridging response of Z-pins subject Mode I loading. Data adapted from [12]. 97
4.5 The bridging response and corresponding velocity profile in Mode I loading subject to dynamic rate. Data adapted from [12]. 99
4.6 Z-pin surface observed using scan electron microscopy in (a) pristine condition and subject to (b) quasi-static and (c) dynamic loading.Images are courtesy of Dr. Hao Cui. 100
4.7 Hole surface observed using scan electron microscopy after Z-pin pull-out at (a) quasi-static and (b) dynamic rates.Images are courtesy of Dr. Hao Cui. 100

4.8 Tip cross section profile of two different Z-pins in pristine condition. Images are courtesy of Dr. Hao Cui. 101
4.9 A bridging response in dynamic test presented in Ref. [12] . . 102
4.10 Quasi-static mode II response (a) bridging response of Z-pins, (b) velocity profile. Data adapted from Ref. [12]. 104
4.11 High rate mode II response (a) bridging response of Z-pins, (b) velocity profile. Data adapted from Ref. [12] 105
4.12 Mode II bridging response for specimen T3 at quasi-staic loading as a function of (a) Displacement and (b) Time. Data adapted from Ref. [12]. 105
4.13 Scan Electorn Microscopy image of the Z-pin fracture surface under mode II loading at (a) quasi-static and (b) high rates. Images courtesy of Dr. Hao Cui. 106
4.14 The quasi-static bridging response and mode mixity achieved in mixed mode loading with Z-pin mixed mode angle of (a) 15°, (b) 30°, (c) 45°, (d) 60° and (e) 75°, where 0° is pure mode I and 90° is pure mode II. Data adapted from Ref. [13]. 107
4.15 SEM image of the failure surface of Z-pinned laminate subject to quasi-static loading with a mixed mode angle of (a) 15° and (b) 30°. Images are courtesy of Dr. Hao Cui. 108
4.16 SEM image of the failure surface of Z-pinned laminate subject to quasi-static loading under a mixed mode angle of 45°. Image is courtesy of Dr. Hao Cui. 110
4.17 The Velocity profile of the Z-pin response subject to quasi-static loading for a mixed mode angle of 45°. Data adapted from Ref. [13]. 111
4.18 The dynamic bridging response and mode mixity achieved in mixed mode loading with mixed mode angle of (a) 15° and (c) 30° with the corresponding velocity profile attained in (b) and (d) respectively. Data adapted from Ref. [13] 112
4.19 SEM image of the failure surface of Z-pinned laminate subject to dynamic loading under a mixed mode angle of 75°. Image is courtesy of Dr. Hao Cui. 113
4.20 The dynamic bridging response and mode mixity achieved in mixed mode loading with mixed mode angle of (a) 45°, (c) 60° and (e)75° with the corresponding velocity profile attained in (b), (d) and (f) respectively. Data adapted from Ref. [13] . . . 114

4.21 Dynamic bridging response for the three high mixed mode angles of 45°, 60° and 75° plotted on the same graph. Data adapted from Ref. [13]. 115
4.22 Dynamic bridging response for mixed mode angle of 75° and Mode II plotted on the same graph. Data adapted from Ref. [12, 13]. 116
4.23 Energy absorbed as a function of the nominal mixed mode angle for different loading rates. 117

5.1 Reference configurations for the three response stages: (a) bonded Z-pin; (b) de-bonding Z-pin; (c) pull-out 122
5.2 Convergence Study with different number of peridynamic particles (N) 132
5.3 The bridging response at 5m/s obtained from the proposed peridynamic model compared to the experimental results in Ref. [12]. 136
5.4 The bridging response at 12m/s obtained from the proposed peridynamic model compared to the experimental results in Ref. [12]. 136
5.5 The bridging response at quasi-static loading obtained from the proposed peridynamic model compared to the experimental results in Ref. [12]. 137
5.6 The bridging response at quasi-static loading obtained from the proposed peridynamic model compared to the experimental results in Ref. [12]. 138
5.7 The bridging response at 5m/s obtained from the proposed peridynamic model compared to the experimental results in Ref. [12]. 139
5.8 The bridging response at 12m/s obtained from the proposed peridynamic model compared to the experimental results in Ref. [12]. 139
5.9 Energy dissipated by the Z-pin using model 1: Comparison between Numerical prediction and experimental results at different pull-out rates 140
5.10 Energy dissipated by the Z-pin using model 2: Comparison between Numerical prediction and experimental results at different pull-out rates 141

6.1 Reference undeformed (left) and deformed (right) configurations. 146
6.2 Illustration of bonds crossing a failure plane located at point z_f 156
6.3 The experimental and numerical bridging response under quasi static loading for a nominal mixed mode angle of (a) 0°, (b) 9° and (c) 15°. 164
6.4 The experimental and numerical bridging response under quasi static loading for a nominal mixed mode angle of (a) 30°, (b) 45°, (c) 60° and (e) 75°. 165
6.5 The experimental and numerical bridging response under dynamic loading for a nominal mixed mode angle of (a) 0°, (b) 9° with 5m/s rate, (c) 9° with 12m/s rate and (e) 15°. 167
6.6 The experimental and numerical bridging response under dynamic loading for a nominal mixed mode angle of (a) 30°, (b) 45°, (c) 60° and (e) 75°. 168
6.7 The effect of misalignment angle on the Z-pin bridging response for a nominal mixed mode angle of 15°. 170
6.8 The effect of variability in Z-pin strength on Z-pin bridging response for a nominal mixed mode angle of 15°. 170
6.9 The numerical model prediction when including variability compared to experimental results. (a) and (b) correspond to nominal mixed mode angle of 15° and 30° and are under dynamic loading. (c) and (d) correspond to nominal mixed mode angle of 15° and 30° and are under QS loading. 171
6.10 A comparison of predicted and experimental energy dissipated by Z-pin at different nominal mixed mode angles under dynamic loading. 172
6.11 A comparison of predicted and experimental energy dissipated by Z-pin at different nominal mixed mode angles under quasi-static loading. 173

A.1 Deformation and forces for a classical beam. 185

C.1 Illustration for calculating bridging force across a delamination plane. 189

List of Tables

2.1 Advantages and disadvantages of different TTR concepts compared to a baseline of unidirectional laminates. Adapted from Ref. [2] 34
2.2 Summary of the advantages and disadvantages of Z-pinning. . 39
2.3 Failure mechanisms for metallic and composite Z-pins subject to mode II loading. 43

4.1 Summary of the test matrix for quasi-static testing. 119
4.2 Summary of the test matrix for high rate testing. 119

5.1 Mechanical and physical properties of a T300/BMI Z-pin [12]. 134
5.2 Model parameters varying with loading rate 135
5.3 Sliding friction parameters for QS and dynamic friction models. 137
5.4 Sliding friction parameters for QS and dynamic friction models. 138

6.1 Mechanical and physical properties of a T300/BMI Z-pin [12]. 161
6.2 B-K failure criterion parameters for both dynamic and quasi-static loading. 162
6.3 Sliding friction parameters for QS and dynamic friction models. 162
6.4 Lateral force and snubbing friction parameters for QS and dynamic friction models. 163

Chapter 1

Introduction

1.1 Background

Carbon Fibre Reinforced Plastics (CFRP) are types of composite materials made of carbon fibres embedded in a polymeric matrix. The carbon fibre is used as a reinforcing element due to its high strength and stiffness properties. The matrix provides the medium that holds the reinforcing elements together by allowing load transfer through shear. Both elements, the carbon fibre and plastic matrix, are lightweight, yielding a composite material (CFRP) with a high strength/stiffness to weight ratio. However, the aforementioned properties are highly anisotropic with very high strength/stiffness along the fibre direction and relatively low strength/stiffness transverse to the fibre direction. Consequently, CFRP composite structures are usually designed to be loaded along the fibre direction.

Alternatively, CFRP composites can be tailored to specific applications by creating a laminated architecture. This entails manufacturing via stacking CFRP plies, each having the fibre reinforcement along a predefined orientation. This approach allows designers to create quasi-isotropic composite lamiantes, with specific strength and stiffness properties that significantly exceed that of structural alloys, such as Steel and Aluminium.

Therefore, CFRP composites are widely considered a weight saving alternative to conventional alloys in structural applications (Ref. [14]). CFRPs nowadays represent an effective solution for weight-critical applications in

many engineering sectors, including aerospace (aeroplanes, satellites, helicopters etc.), marine (hulls, sailing masts), energy (wind turbine blades) and automotive (car monocoque) (Ref [15–17]). In addition, CFRP composites have excellent fatigue characteristic and good thermal and wear properties. This widens their area of application to rotating shafts, breaks and bearings (Ref [15]). The use of CFRP composites has increased significantly over the past few decades as a result of a better understanding of their in-service performance and overall favourable properties (Ref. [14]). A prominent example is the relative recent entry into service of the Boeing 787 (2011) and the Airbus A350 (2014) aircrafts, which are more than 50% composite made.

On the other hand, CFRP composites suffer from an inherently low through-the-thickness strength, making them susceptible to delamination. The presence of delamination has an adverse effect on the static strengths, fatigue endurance and buckling behaviour (Ref. [18–20]). Impact loading is the main cause of delamination, as it introduces large through-the-thickness stresses.

Aerospace structures may withstand various impact loading conditions, ranging from low-velocity events (a simple tool drop) to high-speed impact (bird impact). Depending on the impact speed, the resulting damage can range from barely-visible flaws (BVID) to substantial delamination and fibre breakage. To ensure safe operation of composite aircrafts, the civil aviation authorities (EASA and FAA) introduced safety standards specifically for composite structures. These safety standards includes certification requirements that addresses the damage tolerance of composites in the presence of delamination (see acceptable means of compliance in AMC 20-29 (EASA) and AC 107-B (FAA)).

The review of the certification process shows that there are two main routes in regards to damage tolerance. The first is based on a "no growth" assumption, while the second is based on a "slow/arrested growth" strategy. The "no growth" paradigm requires the damage (including delamination) size not to grow throughout the life of the aircraft or within inspection intervals, depending on the location of damage. The "slow/arrested growth" allows the damage to grow in a slow and stable manner that allows detection within the time interval between inspections.

Airframe manufacturers usually opt for the "no growth" design philosophy, as it is a more conservative approach (Ref [21]). This may however result in thicker laminates (to reduce stress levels), hence higher weight and sub-optimal structural efficiency. Thus, increasing the through thickness strength, delamination strength and delamination resistance of composite materials should facilitate the shift from "no growth" strategy to "slow growth" strategy. This would improve the structural efficiency of composite structures and allow for a significant weight saving to be achieved.

1.2 Through Thickness Reinforcement (TTR)

Through-thickness reinforcement (TTR) is a well established method of increasing the through-thickness strength and fracture toughness of CFRP composites. Through-thickness reinforcement techniques include stitching, tufting, braiding, z-anchoring and 3D weaving (Ref. [22–24]). The aforementioned techniques are only suitable to be applied to dry fabrics, both two- and three-dimensional. However, primary aerospace structures require high fibre volume fractions coupled with excellent control of the reinforcement alignment, which are attainable through the use of prepreg laminates.

Z-pinning is the only TTR technique suitable to reinforce prepreg laminates. It consists of inserting small diameter pins in the laminate through-thickness direction (usually referred to as the Z-direction, and hence the name Z-pinning) to “lock” the plies together through adhesion and friction. The Z-pins are usually made from high strength and stiffness materials such as metal alloys (titanium and steel) or from fibrous carbon composite.

The use of Z-pins is seen to vastly enhance the damage tolerance and delamination resistance of CFRP composites at different loading rates. Under static loading, Z-pinning dramatically increased the mode I fracture toughness and significantly improved mode II fracture toughness (Ref. [25–27]). In low-speed impact conditions, Z-pinning was seen to reduce the delaminated area by as much as 64% (depending on impact condition - Refs [25, 28, 29]), thus enhancing the delamination resistance of CFRP composites. The reduction in delaminated area translates into an improvement of the post-impact mechanical performance of Z-pinned laminates (Ref. [30–32]). This is particularly evident from the significant increase of the compression-after-impact

(CAI) strength by about 45% in Z-pinned laminates (Refs [18, 19]).

On the other hand, Z-pinning has its drawbacks as well. The insertion of Z-pin displaces the fibres in its neighbourhood, causing fibre waviness, ply crimping and the formation of resin pockets. This in turn results in a reduction of the in the in-plane mechanical properties, such as longitudinal and transversal moduli and strengths. The extent of the reduction in mechanical properties depends on Z-pin diameter and areal density (Ref. [33–35]).

Nonetheless, upon careful design trade-off considerations, Z-pinning was successfully used in industrial applications. For example, Z-pinning have been used on the inlet duct of the F-18 military aircraft ("Superhornet") to replace titanium fasteners. This resulted in significant cost and weight savings (Ref [36]). In addition, Z-pins are used in high performance sports to reinforce crash structures and improve safety. For instance, the Z-pins are used to reinforce roll-bar hoop structures on Formula 1 cars (Ref. [37]).

1.3 Objective and Vision

Although Z-pinning has been utilised in specific engineering applications, the wider industrial adoption of this technique remains limited. For example, a clear industrial application is to use Z-pins as "micro-fasteners" as recently suggested (Ref. [38]). Such applications allow the shift from the "no-growth" design paradigm to a "slow growth" approach, resulting in higher structural efficiency and weight savings.

The lack or inadequacy of modelling capabilities for Z-pinned laminates is one of the reasons for the lack of a wider industrial adoption of through-the-thickness reinforcement. Z-pins have sub-millimeter diameters, while typical aerospace structures have characteristic dimensions in the order of meters. Hence, in large-scale engineering applications there would typically be thousands of Z-pins inserted into composite components. Clearly, individual Z-pins cannot be modelled at the structural scale and suitable scale-bridging homogenisation techniques must be introduced to predict the effect of through-thickness reinforcement on the mechanical performance of composite components. This thesis proposes the use of a multi-scale approach to

model Z-pinned laminates.

At the core of the multi-scale approach is a reduced order model (ROM) that is able to predict the Z-pin bridging action, i.e. the traction forces exerted by the Z-pin as function of the crack opening and sliding displacements. This thesis proposes a ROM model that is computationally cheap and efficient, while providing a relatively accurate prediction. The developed model is capable of predicting bridging performance under mixed-mode loading and across a range of loading rates. Currently, there is no such ROM models available in the literature, as it will be discussed in chapter 2.

The ROM model can then be used in a multi-scale modelling approach as follow:

1. Meso-level 1 (Objective): The ROM model at this level is required to predict and characterise the bridging performance of a single Z-pin embedded in a delaminated composite coupon.

2. Meso-level 2 (Objective): At this modelling level the array bridging response of multiple Z-pins is obtained. This is particularly important where variability in input parameters alters the observed bridging response of Z-pin array compared to individual Z-pins.

3. Macro-scale (Vision): At this scale full structures are considered where Z-pins are used in selective regions that are prone to delamination damage. The output from the ROM model is input into the main simulation as both run concurrently in real time. Alternatively, the ROM model can be used to create bridging maps as a function of mode mixity and loading rate. The ROM model allows the creation of such a map in a reasonable time. Then the Z-pinned laminate can be modelled in finite element packages with the Z-pin contribution interpolated from the created bridging map.

With the aforementioned objective in mind, the thesis has the following structure:

1. Chapter 2: Presents a literature review of through thickness reinforcement techniques with a particular focus on Z-pinning. A review of current modelling techniques and approaches is also presented.

2. Chapter 3: Introduces the developed peridynamic rod and beam formulations which are used as the basis for the ROM model. The developed formulations are then verified by comparing the model outcome to well established analytical results.

3. Chapter 4: Presents the experimental setup and procedure used to characterise the bridging performance of the Z-pin under quasi-static and dynamic loading. The obtained results are presented and discussed in this chapter. These are the results that are later used to calibrate and validate the developed ROM model.

4. Chapter 5: The mode I rate dependent bridging performance of Z-pin is developed in this chapter. The Ruina's rate dependent friction model is adopted to model the friction acting on the Z-pin as it slides out of the CFRP laminate. The obtained results are presented and compared to experimental results.

5. Chapter 6: The mixed mode rate dependent bridging performance of Z-pin is developed in this chapter. Two models are presented: a deterministic model and non-deterministic model. The deterministic model does not take into account the variability in the Z-pin misalignment angle and strength. The deterministic model yields poor performance in the transition region where the Z-pin is sensitive to the variability observed. The non-deterministic model takes into account the variability of the Z-pin misalignment angle and strength across an array of Z-pins and obtain an averaged response equivalent to that observed in the experimental results. The obtained results are then presented and compared against the available experimental results.

6. Chapter 7: A summary of the work conducted in the thesis is available in this chapter. In addition, a suggestion is made for future work.

Chapter 2

Literature Review

2.1 Introduction

The susceptibility of Polymer Matrix Composites (PMC) to delamination crack is the main challenge for applications where damage resistance and damage tolerance are paramount. It is necessary to distinguish between damage resistance and damage tolerance as these are two different aspects that lead to different design philosophies. Damage resistance refers to the ability of a structure/component to withstand a certain level of loading while sustaining minimal damage. On the other hand, damage tolerance refers to a structure being able to withstand a certain level of damage with minimal impact on structural performance.

Through thickness reinforcement (TTR) techniques were developed and are being used to improve the damage resistance and tolerance of laminated composite structures. These techniques are reviewed and briefly discussed in the first section of this chapter.

The second section provides a more detailed review of a particular form of TTR, namely Z-pins. The review includes manufacturing methods of Z-pinned laminates, advantages and disadvantages of Z-pinning and experimental results under different loading modes and subject to different loading rates. A discussion of the Z-pin failure mechanisms is presented to explain the observed increase in the apparent fracture toughness of Z-pinned laminates. The understanding of Z-pin failure mechanisms forms the basis of the

Z-pin model developed later in this thesis.

Lastly, the literature is surveyed for the different modelling approaches that have been developed to simulate the response of Z-pinned laminates. The models developed range from analytical to numerical models describing the Z-pin bridging performance at multi-scales ranging from meso-1 level to macro-scale. The modelling review has two purposes. The first purpose is to learn from the approaches developed and build upon them where appropriate. The second purpose is to identify a knowledge gap in order to formulate a research question that this thesis addresses.

The knowledge gap identified in the literature review is that the literature is void of a reduced order model (ROM) capable of simulating Z-pin bridging performance under dynamic loading conditions. Therefore, this thesis is concerned with understanding the dynamic bridging performance of Z-pins. This understanding is then used to develop a ROM model that is both accurate and computationally cheap. The method used to develop the reduced order model is called Peridynamics, which is a relatively new branch of mechanics. Peridynamics will be discussed in details in chapter 3 of this thesis where the model formulation is developed.

2.2 Through Thickness Reinforcement Methods

Laminated composites are manufactured by laying plies to form a laminate. Once cured the plies are held together by the matrix which is the weakest component in PMCs. Therefore, the through thickness strength of laminated composites is usually significantly lower than the strength in the other directions which have reinforcing fibre elements. Thus when laminated composites are loaded, they tend to delaminate at the ply interface in the through thickness direction (see fig. 2.1).

Many methods have been developed to improve the through thickness strength of laminated composites, in order to address their susceptibility to delamination. These methods include matrix based techniques such as toughened resins and interleaving, addressing matrix brittleness and the quality



Figure 2.1: Impact damaged laminate showing delamination forming at ply interfaces in the through thickness direction, obtained from Ref. [1]

of the fibre/matrix interface. Alternatively, introducing reinforcing elements in the through thickness direction has been utilised to improved the through thickness strength, these include techniques such as stitching, tufting and Z-pinning. Changing the architecture of the composite material from the standard unidirectional laminae (ply) has been investigated. This include using 3D composite architecture as a possible mean of improving through thickness strength. A change in the architecture can be achieved through various manufacturing routes such as weaving, braiding and knitting. These TTR methods results in either an improvement in damage resistance, damage tolerance or both and are discussed in more detail in the following sections.

2.2.1 Toughened Matrix

Intuitively, delamination resistance can be improved by enhancing the toughness of the matrix. Improvement in matrix toughness can be achieved by incorporating a secondary toughened phase (see fig. 2.2) into the matrix. During fracture, the introduced secondary phase causes crack blunting, plastic flow and void coalescence; mechanisms which absorbs significant amount of energy resulting in improved toughness.

Alternatively, changing matrix from thermosetting (such as epoxy) to

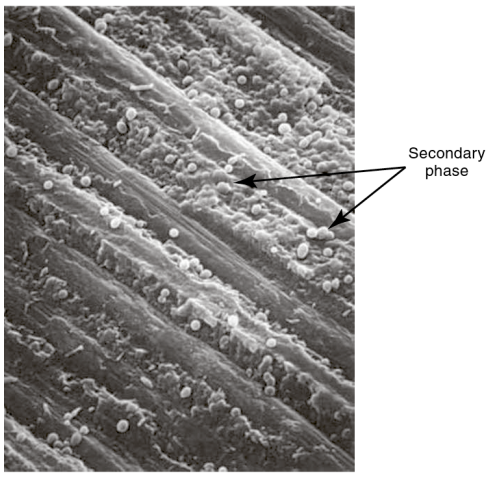


Figure 2.2: Secondary phase toughening particles in matrix, obtained from Ref. [1]

thermoplastic can enhance the fracture toughness. Thermoplastic matrix (such as PEEK) can absorb significant amount of energy through plastic flow (see fig. 2.3) as suggested in Ref. [39].

Although improving the fracture toughness of the matrix enhances the delamination resistance of PMCs, it does come at a cost. Generally, tougher matrix systems tend to cause a reduction in other mechanical properties. tougher resins are more compliant which tend to reduce the compression dominated properties. There is evidence in literature that increased tough-

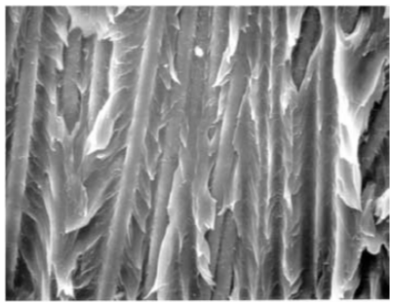


Figure 2.3: Delamination in AS4/PEEK material showing significant plastic flow, obtained from Ref. [2]

ness results in reduced fatigue performance (Ref. [40]). In addition, using secondary phase toughened resins is shown to result in larger variability at structural response level as discussed in Ref. [41]. This is due to inhomogeneity in secondary phase particle dispersion. Thus unlike at coupon level where delamination is initiated at a predefined location, at structural location delamination tend to initiate at unknown location prior to loading. If the toughening particles conglomerate in certain places, then delamination will occur in places void of the toughening particles which limits the benefit of the secondary phase toughened matrix. On the other hand, the processing route for tougher thermoplastic matrices is different than conventional materials causing manufacturing difficulty when having to attach two substructures manufactured through different routes.

2.2.2 Interleaving

Interleaving includes the incorporation of a thin layer between composite plies (see fig. 2.4 for illustration) to improve the toughness at the interface, resulting in enhanced damage resistance and tolerance of composites. Interleaving can be categorized into three classes: nanofiber, particle and film interleaving (Ref. [3]).

The most basic interleaving can be achieved by increasing the interface thickness through the use of additional matrix resin. Using this method with an interleave layer thickness of 0.2mm, fracture toughness improvement of 70% and 200% for G_{IC} and G_{IIC} respectively was reported in Ref. [42–44]. Various studies of the effect of the thickness of different interleaving films

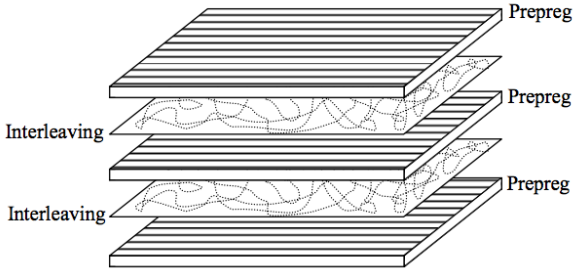


Figure 2.4: Schematic illustration of interleaving, obtained from Ref. [3]

showed that the mode I and II fracture toughness was significantly increased by interleaving (Ref. [45–47]).

Another method of providing an effective interleave layer is through the use of polymer particles, nano fibres and short fibres. These methods were reported to result in an increase in fracture toughness of 28% and 260% in mode I and II respectively (Ref. [48, 49]). The advancement of nano-technology resulted in several studies into the possible use of nano-fibres as interleave material (Ref. [50–56]). A novel technique developed in Ref [50,51] allowed the aligning of carbon nano-tubes in the through thickness direction facilitating their use as interleave materials. Their use resulted in 300% increase in mode I and II fracture toughness.

Although introducing interleave materials is shown to improve delamination resistance in composite laminates, they cause detrimental effects on other composite properties. For example, it tends to reduce global stiffness and fibre volume fraction which leads to a consequent weight penalty (Ref. [57,58]). The use of nano-particles as interleave layers can prove to be prohibitively expensive at an industrial scale.

2.2.3 Stitching

Stitching, similar to that in textile, consists of inserting a needle into fabric preform or prepreg laminate to introduce a high tensile strength yarn (usually kevlar, carbon or glass) in the through thickness direction. Stitching has been used to improve the through thickness fracture toughness, delamination resistance and damage tolerance (Ref. [59–63]). In addition, stitching is a cost-effective method to join fabric cloths that improves handling prior to

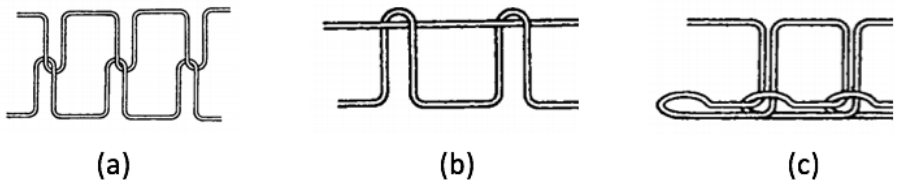


Figure 2.5: Different Stitch Types, (a) lock stitch, (b) modified lock stitch and (c) chain stitch. Obtained from Ref. [4]

liquid moulding (Ref. [64–67]).

Stitching requires access to both sides of the laminate in order to create different types of stitches. Three main types of stitches are shown in fig. 2.5, each having pros and cons discussed in Ref. [4]. In addition to stitch type, different stitching parameters influence the behaviour of stitched composites. These parameters include the stitch density (number of stitches per area), stitch pattern and span and material properties of the thread fibre. Consequently, this will increase the design parameters for optimisation making the design process of stitched composite more complex (Ref. [63]).

The process of inserting the needle during stitching causes fibre damage and fibre breakage. In addition, the inserted thread causes the main load bearing fibres to spread around the stitch. This causes a misalignment in the load bearing fibre around the stitch ranging from 2.5° to 20° in CFRP and stitched woven glass fabric respectively (See Ref. [68, 69]). The damage caused by stitching affect the in-plane mechanical properties of FRP composite, which is reviewed comprehensively in Ref. [62]. Most notably is that the in-plane compressive properties are degraded by a factor of 5% to 55% depending on various parameters (see Ref. [62]).

Although prepreg laminates can be stitched, the level of damage caused by the needle insertion is significant. The increased observed damage in prepreg laminates is due to the relative inability of the fibre to move out of the way of the needle inserting the through thickness thread because of the high resin viscosity. The degradation in mechanical properties due to stitching of prepreg laminates outweighs the potential improvement in delamination resistance and damage tolerance. Therefore, stitching is not a suitable method for through thickness reinforcement of prepreg laminates.

2.2.4 Tufting

Tufting is the process of using a needle to insert a thread (called tuft) in the through thickness direction, creating a loop on the other side of the preform as shown in fig. 2.6a. Although, tufting does not tie or interlock the loops, the tufts remain in position purely due to the action of friction between the tuft and the preform. The tuft can either be fully or partially inserted into the preform as shown in fig. 2.6b. Unlike the conventional stitching methods,

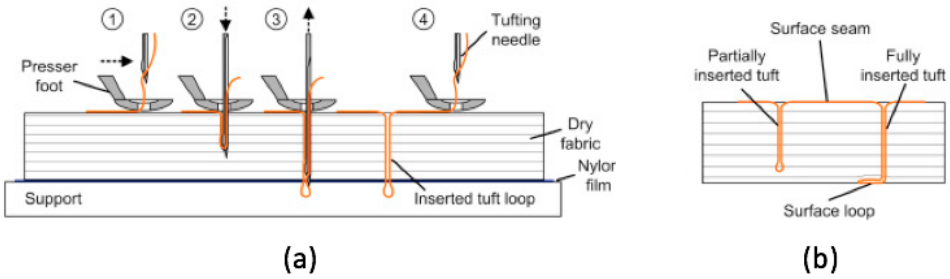


Figure 2.6: Schematic illustration of (a) the sequential manufacturing steps to inserting a tuft and (b) of partial and full penetration. Adapted from [5]

tufting can be achieved through one sided access to the preform (Ref. [5]), advantageous from manufacturing point of view. However, tufting is limited in application to dry preforms as discussed in Ref. [5] where the manufacturing process is reviewed in detail.

Tufting has been shown to improve the delamination response at quasi-static and dynamic loading rates in both mode I and II loading (Ref. [70,71]). Tufting has improved the fracture toughness in mode II and mode I by 2 and 5 folds respectively. Nonetheless, due to the insertion of the tuft in the through thickness direction, the main load bearing fibres in the preform will become slightly misaligned, a resin rich eyelet is formed and some fibres are broken. Inevitably, this results in reduction of in plane properties, less than 10% as presented in Ref. [72]. However, the improvement in delamination resistance and damage tolerance tends to outweigh the reduction in in-plane properties. For more details on the mechanical response of tufted composite the reader can consult Refs. [70–73].

2.2.5 Z-pinning

Z-pinning consists of inserting a rod in the through thickness direction (the Z-direction) of laminated composites, hence the name Z-pinning. The Z-pin effectively nails the laminate plies causing them to lock together through a combination of adhesion and friction (see fig. 2.7). Unlike stitching and tufting, Z-pinning is the only through thickness reinforcement method suitable for use on prepreg laminates.

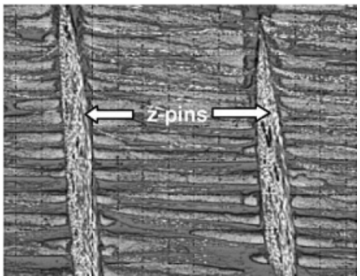


Figure 2.7: Z-pin inserted into prepreg laminate. Adapted from [6]

In addition to the use of Z-pins as through thickness reinforcement to improve damage tolerance, there is a drive to consider Z-pins as micro-fasteners to join different sections together (Ref. [38]). A prominent example is the use of Z-pins to reinforce stiffener-to-skin T-joints (Ref. [74]).

Although interleaving and toughened matrix can be used with prepreg laminates, the use of Z-pinning is shown to have a significant improvement in damage tolerance compared to these two methods (Ref. [41]). An in depth review of the Z-pinning concept including mechanical performance, manufacturing method and modelling techniques is presented in the next section of this chapter.

2.2.6 3D Laminate Architecure

Textile manufacturing methods such as weaving, braiding and knitting have been copied across to manufacture 3D composite structures. The through thickness reinforcing fibres volume fraction in full 3D composites exceed the maximum of 5% used in tufting, stitiching and Z-pinning.

The 3D architecture is usually constructed as fibre preforms where the matrix is later introduced through resin infusion. Thus components manufactured through weaving, braiding and knitting tends to achieve near net shapes (Ref. [75]). Consequently, a complex shape manufacturing could potentially be simpler and less expensive with these methods. Complex components such as the fan blade in the GE Leap engines have been successfully manufactured using 3D weaving (see fig. 2.8).

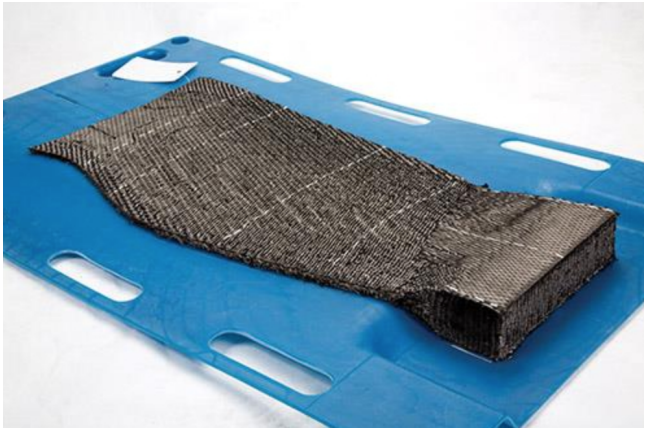


Figure 2.8: GE Leap fan blade manufacture using 3D weaving in the preform configuration, obtained from Ref. [7]

Increasing the fibre content in the through thickness dimension is advantageous for damage resistance and damage tolerance for impact velocities ranging from a simple tool drop up to ballistic speeds (Ref. [2, 75]). However, the through thickness fibres can act as crack initiating sites leading to a reduction in the undamaged mechanical performance. For example, compressions stiffness and strength is reduced due to higher proportion of fibres not being aligned with the main loading direction (Ref. [2]).

2.2.7 Summary

The susceptibility of laminated composites to delamination necessitates the development of through thickness reinforcement. Various methods have been developed over the past few decades to enhance the through thickness strength. These methods can be summarised as:

1. Matrix based methods such as toughened matrix and interleaving
2. Introducing through thickness fibres in small proportions (typically less than 5% of total fibre volume) using methods such as stitching, tufting and Z-pinning.
3. Utilising weaving, braiding and knitting to produce fully 3D composite architecture.

Concept	Advantages	Disadvantages
Toughened Matrix	Same architecture as baseline Usually similar costs and time scales No need for redesign Usually the same processing- route	Reduced Fatigue and compression properties Increased sensitivity to processing Can require different processing route Inhomogeneity in toughened particles-dispersion at structural level
Interleaving	Undamaged properties as baseline Similar processing route	May reduce compressive performance Increased thickness may lead to redesign required Adds parasitic weight and extra cost
Stitching	Same processing route Offers fail safe design	Can reduce undamaged properties Difficult to fabricate with stiffeners Not suitable for use on prepreg laminate
Tufting	Same processing route	Can reduce undamaged properties Not suitable for use on prepreg laminate
Z-pinning	Same processing route optimisation can limit drop in-undamaged properties offers fail safe design Suitable for use in prepreg laminate	Can reduce in-plane properties relatively high cost
3D composite	Achieves near net shape Concept becoming fairly mature	Requires redesign and re-qualification Reduce undamaged properties Can require expensive machine to be designed

Table 2.1: Advantages and disadvantages of different TTR concepts compared to a baseline of unidirectional laminates. Adapted from Ref. [2]
.

Toughened matrix shows enhanced fracture toughness at coupon level. However, this does not necessarily translates to structural level due to inhomogeneity in toughening particles distribution. On the other hand, stitching, tufting and Z-pinning have been shown to result in improvement in damage tolerance but the use of these methods degrades the undamaged in-plane properties of laminated composites. Nonetheless, Z-pinning is reported to be the only method suitable for use in prepreg laminates. Three dimensional architecture composite shows promise in improving delamination resistance and damage tolerance but it reduces the undamaged performance of composites. In addition, 3D architecture requires the development of specialised machine which could prove to be prohibitively expensive. The advantages and disadvantages of each method is summarised in Table 2.1.

An assessment of different through thickness reinforcement method of stiffened aerospace structure by Greenhalgh et al. (Ref. [2]) concluded that Z-pinning is the most promising reinforcement technique when compared to other methods such as tougher matrix, 2D and 3D weaving and stitching.

2.3 Z-pinning - Comprehensive Review

The manufacturing of Z-pinned laminates requires the insertion of Z-fibre into the composite structure. The inserted Z-pin "nails" the laminate together while pushing the in-plane fibres apart. Consequently, Z-pinned laminate have better damage tolerance but reduced in-plane properties when compared to pristine (unpinned) laminate. This section reviews Z-pin insertion process, effect on micro-structure of laminated composite, mechanical performance and energy absorption mechanisms.

2.3.1 Manufacturing Method

Early Z-pin insertion process (early 1970s to late 1990s) was fairly rudimentary consisting of manually pushing individual Z-pins into the composite laminate (Ref. [25, 76, 77]). These methods were imprecise and slow which hindered their adoption at an industrial scale.

By late 1990s a new Z-pin insertion process known as Ultrasonic Assisted Z-fibre (UAZ) was developed and patented (Ref. [78]). This process is currently the most adopted method for insertion of Z-pins into laminated com-

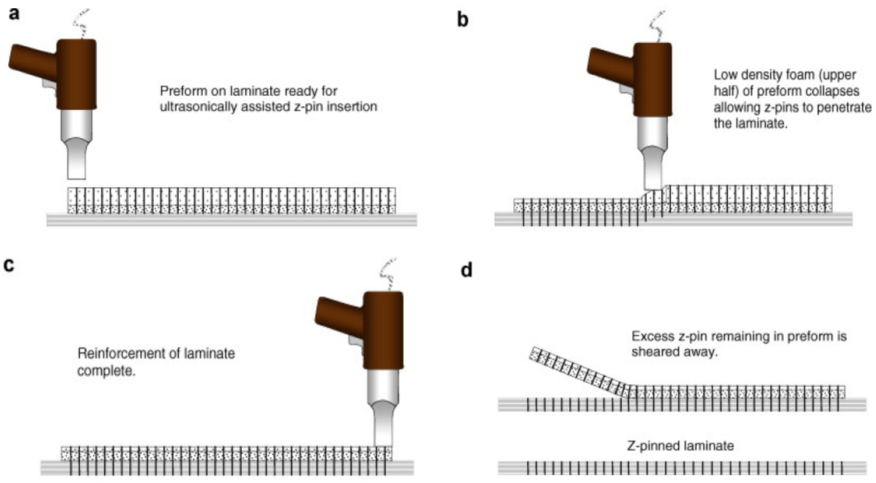


Figure 2.9: Illustration of UAZ insertion process. Obtained from Ref. [8]

.

posites. The process involves Z-pins placed in crushable foam which is placed over the laminate and driven into the prepreg with a combination of pressure and ultrasonic vibration. The foam provides lateral support to the Z-pin as they are driven into the laminate. The ultrasonic vibration causes mild heating of the resin increasing its viscosity and easing the insertion process. Once the Z-pins are inserted, the crushed foam can be easily removed from the surface and excess Z-pin length is machined off. A schematic illustration of the insertion process is presented in fig. 2.9. After Z-pin insertion, the laminate is cured via the conventional process i.e. vacuum bagging and autoclave. Consequently, there is no need for radical change in the processing route of Z-pinned laminate; only an additional step in the manufacturing process. The insertion process can be semi-automated for wide area reinforcement of composite laminate. However, this process lacks the ability to control the Z-pin insertion angle and may induce both Z-pin splitting and out of plane fibre crimping (Ref. [6, 11, 79]). The insertion angle is the angle that the Z-pin makes with the orthogonal direction (i.e. the z-axis). When the insertion angle deviates from the intended angle it is referred to as misalignment angle.

More recently, a new method for Z-pin insertion has been developed and patented by Rolls-Royce (Ref. [79]). This method is known as the direct insertion method. The key stages in this process can be summarised as:

1. The uncured material is heated to a predetermined temperature. This temperature is unique to each matrix material and depend on various factors such as matrix material curing parameters, rheology and gelation time. For more details the reader is referred to Ref. [79].

2. Once the whole laminate reaches the predetermined temperature, a sharpened needle with conical insertion tip is inserted into the laminate and then removed to create a hole. The needle diameter should be larger than the diameter of the reinforcing rod.

3. The reinforcing rod is inserted into the laminate at the location where the hole was created.

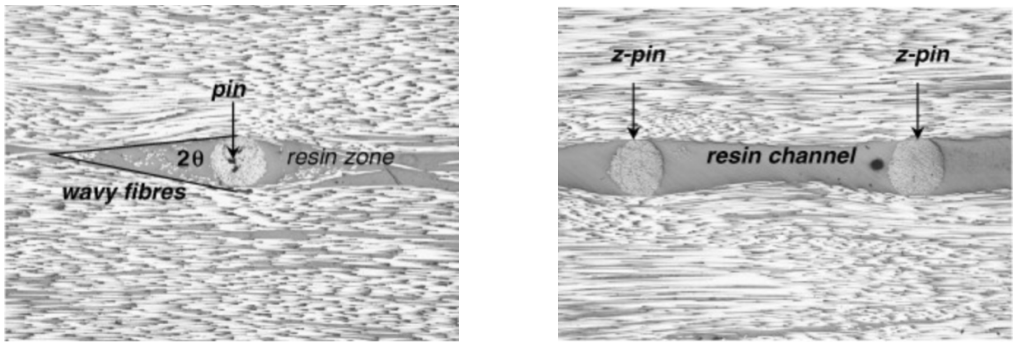
The direct insertion method can achieve high precision in the insertion angle of the Z-pin. It has been reported that a negligible misalignment angle has been achieved using the direct insertion method (Ref. [13]). In addition,

the direct insertion process can be fully automated capable of inserting Z-pins at an industrial scale.

Common to all Z-pin insertion methods, certain manufacturing parameters need to be selected. This includes the Z-pin materials, diameter, insertion angle and areal density to be used. The Z-pin is usually made from high strength and modulus material such as steel, titanium or pultruded fibrous rods. The diameter generally ranges from 0.15mm to 1mm (See Ref [6]). The areal density is the area covered by Z-pins as a percentage of the laminate surface area. The areal density dictates the distance between adjacent Z-pins and usually ranges between 0.5% to 2%.

2.3.2 Microstructure of Z-pinned Laminates

The insertion of Z-pin results in changes to the micro-structure of laminated composites. The inserted Z-pin pushes the fibre aside resulting in fibre waviness in the vicinity of the Z-pin (see fig. 2.10a). During cure the resin flows into the voids around the Z-pin creating a resin rich area (see fig. 2.10a) in the form of an eyelet around the Z-pin. Intuitively, the larger the Z-pin diameter the larger the waviness angle and the bigger the resin rich area. In fact a study conducted by Paul Chang (Ref. [8]) showed that the waviness



(a) (b)

Figure 2.10: (a) Shows fibre waviness and resin rich zone around the Z-pin. (b) Shows the formation of resin channel at high areal density. Obtained from Ref. [6]

.

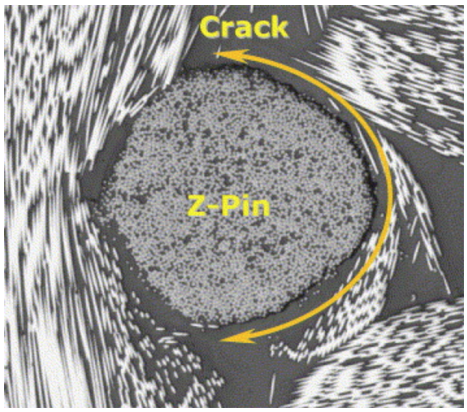


Figure 2.11: Debonding of the Z-pin after curing. Obtained from Ref. [9]
.

angle increases linearly with the Z-pin diameter. The larger the Z-pin areal density (i.e. the closer the Z-pins to each other) the more likely it is for the resin rich areas to coalesce to form a resin channel (see fig. 2.10b).

The effective "nailing" together of the laminates by the Z-pin results in fibre crimping as shown in fig. 2.7. Furthermore, the force required to insert the Z-pin may result in fibre breakage (Ref. [80]). However, the level of fibre fracture and volume fraction of crimped fibres is significantly less than that experience by other reinforcing methods such as 3D weaving, knitting and stitching (Ref. [81, 82]).

The thermal mismatch between the Z-pin and the host laminate causes thermal stresses during the cure process resulting in partial Z-pin debond from the laminate as seen in fig. 2.11. A finite element analysis by Zhang et al. (Ref. [11]) showed that after the cure cycle the Z-pin is partially bonded to the host laminate, with the bonded region forming a helical shape.

Additionally, Z-pin insertion causes swelling in the host laminate in order to accommodate the presence of the Z-pin. The swelling in the host laminate results in a reduction of the average fibre volume content (Ref. [6]).

2.3.3 Mechanical Behaviour of Z-pinned Composites

A detailed review of the effect of Z-pinning is presented by Mouritz in Ref. [6]. Thus a brief discussion of the pros and cons of Z-pinning is presented below with a summary of key points in table 2.2.

Through thickness reinforcement via Z-pinning improves the through thickness elastic properties such as through thickness Young's Modulus and compressive strength. In addition, Z-pinning significantly improves the inter-laminar fracture toughness subject to mode I and II loading. Consequently, the impact response of Z-pinned laminate is greatly improved with noticeable enhancement in delamination damage resistance.

On the other hand, the presence of Z-pin distorts the micro-structure of laminated composite as presented in the previous section. The changes caused by the presence of the Z-pin; such as fibre waviness, fibre crimp, resin rich area and reduced fibre volume fraction; reduces the in-plane mechanical properties. For example, Z-pinning is reported to reduce the in-plane elastic and/or shear modulus, in-plane tensile, compressive and bending strengths and to reduce the fatigue life of Z-pinned laminate.

Advantages	**Disadvantages**
Effective at resisting propagation of long delamination cracks	Ineffective at suppressing short delamination (less than 2mm)
Improved apparent Mode I and II fracture toughness	Reduces in-plane compressive, tensile and bending strength
Stabilises crack propagation in brittle matrix laminates	Complicates the design phase due to need of compromise between improved fracture toughness and reduced in-plane properties
Reduces impact damage area and increases post impact compression strength	Ineffective at raising threshold impact energy for damage initiation
Can be used as microfasteners avoiding the need to drill holes and use metal fasteners; evenly distributing load over joint	Reduces in-plane young's modulus and/or shear modulus depending on the laminate layup.
Large improvement in fatigue life and ultimate strength of lap joint and can be used to strengthen fastener holes in aircraft	Adversely affect the fatigue life of laminated composite (although it improves fatigue life of bonded joints)

Table 2.2: Summary of the advantages and disadvantages of Z-pinning.

Most of the studies presented in the review paper in Ref. [6] are based on larger scale testing arrays of Z-pins in DCB, ENF or MMB coupons. While

the single Z-pin tests did not account appropriately for the misalignment angle. In addition, these test were based mainly on unidirectional (UD) laminate structure which are not used in practical engineering applications.

A study conducted by Yasaee et al. (Ref. [83]) addressed the above issues. In this study the bridging performance of single Z-pin made from T300/BMI composite material was experimentally characterised taking into account the misalignment angle. The experimental characterisation was conducted for UD and quasi-isotropic (QI) laminates subjected to mode I, II and mixed mode (I/II) loading at quasi-static (QS) rate. The Z-pin bridging response was seen to differ when embedded in UD as opposed to QI laminates. Namely, in mode I, the Z-pin embedded in UD laminate showed a clear initial elastic response followed by debonding and pull-out while in the QI laminate the Z-pin response was smoother (lacking the peak force corresponding to elastic response). The peak forces reached in the UD laminate during the pull-out stage was larger than that in QI laminate. This was attributed to the thermal mismatch between the laminate and the pins damaging the bonding interface. The Z-pin/laminate interface will be weaker in the QI layup due to the presence of multiple ply orientations inhibiting the contraction of the laminate in these respective fibre directions. Under Mode II loading, the Z-pin was seen to rupture in shear-out failure.

The study in Ref. [83] showed the presence of transitional behaviour as the mode mixity load increased from mode I to mode II. A transition region is a region where the Z-pin might fail by either complete pull-out or fracture at random. The transition region starts at a corrected mixed mode angle of 11° and 33° in UD and QI laminate respectively. The transition region occured earlier in the UD laminate due to the bond quality (as discussed earlier) and combined with enahnced friction arising from the punch resistance of the rotated pin against host laminate. The enhanced friction is known as "snubbing" and is discussed in detail by Cox in Ref. [84]. The snubbing effect resulted in an enhanced bridging response of the Z-pin as the mixed mode angle was increased from mode I up to the transition region in the QI laminate. This was not observed in the UD laminate due to the transition region occurring at low mixed mode angle.

Yasaee et. al. (Ref. [85]) has shown that the transition region is influenced by the Z-pin embedded length. In the aforementioned study, Z-pins of

various embedded length (1mm to 10mm) were tested at a range of mixed mode angles. The Z-pin with 1mm embedded length was seen to completely pull-out at mixed mode angle of 30° while the one with 10mm embedded length was seen to fail by fracture. Thus, it can be said that the longer the Z-pin embedded length, the earlier the transition region occur.

Metallic Z-pins inserted orthogonal to the laminate, Contrary to carbon fibre based ones, are much more effective at bridging mode II delamination than mode I delamination (Ref. [86–89]). This is the case because of the difference in failure behaviour. Metallic Z-pins have poor interfacial bonding with the host laminate due to relatively large residual thermal stresses arising from laminate curing process. Also, the sliding friction during pull-out (prominent in mode I loading) is very low. However, under mode II, metallic Z-pins undergo large plastic deformation allowing them to absorb significantly more energy then there carbon fibre based counterparts. M'memebe et al. (Ref. [87]) investigated the use of metallic Z-pins as TTR, in particular the use of inclined metallic Z-pins was examined. Inclining the metallic Z-pin in an array of $\pm 45°$ significantly improved the apparent fracture toughness at both mode I and mode II loading. The improvement in energy absorption at mode I was caused by enhanced friction due to snubbing combined with the plastic deformation of the Z-pin. It was found that inclined metallic Z-pin (stainless steel) was far better than any other alternative identified in literature (including carbon fibre Z-pin) at enhancing mode I fracture toughness. On the other hand, inclined metallic Z-pin was found to be slightly less effective then orthogonally inserted Z-pin in mode II but more effective than their carbon fibre counterparts.

Despite the presence of literature regarding the impact performance of Z-pinned laminates, very little work addressing the dynamic bridging performance of Z-pins is available. Liu et al. (Ref. [90]) tested the mode I delamination of Z-pinned laminates at velocities of up to 100mm/min. However, this is hardly representative of impact velocities witnessed by aircraft in service. Nonetheless, the study (Ref. [90]) did show a noticeable dependency of Z-pin response on loading rate. More recently, a comprehensive study was conducted by Cui et. al. (Ref. [12, 13]) to characterise the bridging performance of Z-pin at dynamic loading rate of the order of meters per second. The outcome from these studies is discussed in detail in Chapter 4.

2.3.4 Z-pin Energy Absorption Mechanisms

The fracture energy improvement in Z-pinned laminated is the result of different micro-mechanisms that absorb energy as the delamination progresses. The energy absorption mechanism depends on Z-pin material, loading mode, loading rate and substrate material and layup (Ref. [1, 10, 41]).

An orthogonally inserted Z-pin subject to pure mode I loading, absorbs energy in three main mechanisms (Ref. [1, 10, 41]):

1. Tension develops in the Z-pin along its axis as it is being pulled out.
2. The Z-pin debonds from the laminates in which it is embedded in.
3. The Z-pin pull-out from the laminate resisted by friction which dissipate energy

The Z-pin material (metallic or carbon fibre) influences the bond quality and adhesion between the Z-pin and laminate. A metallic Z-pin has much weaker bond to the laminate compared to carbon fibre based Z-pin. Consequently, a metallic Z-pin reaches a much lower peak load in the elastic phase and dissipates little energy in the debonding phase. In addition, the level of friction that develops in metallic Z-pins during the pull-out phase is significantly lower than the carbon fibre based counterparts (Ref [87]). Furthermore, the loading rate affects the sliding friction response and consequently the energy absorbed (Ref. [12, 13]). The effect of loading rate is discussed in details in Chapter 4. In mode I loading, where the Z-pin fails by complete pull-out from the embedded laminate, the energy absorbed in the pull-out phase constitutes more than 95% of the total energy absorbed. Thus the energy absorbed in the elastic and debonding phases is negligible (Ref. [10, 12, 83]).

Under mode II loading, an orthogonally inserted Z-pin tends to fail by fracture. The failure process leading to fracture depends on the Z-pin material. The failure process for carbon fibre and metallic Z-pins is summarised in table 2.3 (Ref. [1]).

As the mixed mode loading increases from pure mode I, the Z-pin would tend to push laterally against the laminate. Thus, when the Z-pin is being

Carbon Fibre Z-pin	Metallic Z-pin
The Z-pin undergoes bending.	
Internal shear stress in the Z-pin causes splitting	The Z-pin undergoes Plastic deformation
Transverse shear causes Z-pin shear out	The Z-pin undergoes ductile Failure

Table 2.3: Failure mechanisms for metallic and composite Z-pins subject to mode II loading.

pulled out, there will be an additional enhanced friction acting on the Z-pin which stabilises the pull-out process. This enhanced friction is referred to as "snubbing" (Ref. [10]). Increasing the mixed mode loading angle increases the snubbing effect. At a certain mixed mode angle the forces developing in the Z-pin due sliding and snubbing friction exceeds the Z-pin strength causing the Z-pin to rupture. The variability in the properties of the Z-pin (strength, void content etc.), causes a spread in the mixed mode angle where the Z-pin might fail by fracturing. This mixed mode angle range is referred to as the transition region. In the transition region some Z-pins might fail by fracture while others fail by complete Z-pin pull-out. This transition region was first discussed by Yasaee et. al. in Ref. [83].

Additionally, the loading direction being "with the nap" or "against the nap" (see fig. 2.12 for illustration) affects the failure process (Ref. [10]). This is particularly the case in mixed mode loading. Loading against the nap would induce large shear stresses that could cause fibre rupture and consequently shear out failure (in case of carbon fibre Z-pin) and tensile necking failure (in case of metallic Z-pin). While for the same mode mixity loading with the nap would cause the Z-pin to pull-out from the laminate. This phenomena is illustrated in fig. 2.13 which shows a titanium Z-pin failing by pull-out when loaded "with the nap" and by tensile necking when loaded "against the nap" (Ref. [10]).

2.3.5 Summary

Currently, two main manufacturing methods are used to insert Z-pins into composite materials, Ultrasonic Assisted Z-fibre insertion (UAZ) and the direct insertion (DI) method. UAZ is widely known and used but it lacks high fidelity control of the Z-pin insertion angle. The DI method has been developed more recently by Rolls-Royce. The DI method allows for high fidelity

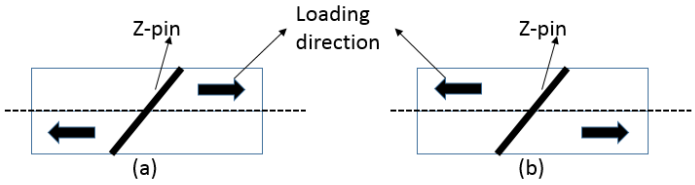


Figure 2.12: Schemaitc illustration of loading (a) with the nap and (b) against the nap.

control of the Z-pin insertion angle and can be easily scaled for industrial use.

The insertion of the Z-pin changes the micro-structure of laminated composites. Z-pin presence induces fibre waviness, creates resin rich area and causes fibre crimp. Inserting Z-pin at high areal density can cause the resin rich areas to coalesce to create a resin channel.

Z-pinned laminates has much higher mode I and II fracture toughness compared to unpinned laminates. Also, Z-pins reduces the post impact delaminated area and improves the compression after impact strength. Nonetheless, the changes in the micro-structure caused by the Z-pin reduces the in-plane properties such as in-plane tensile, compressive and bending strengths. On the other hand, Z-pins has shown promise as micro-fasteners increasing the fracture toughness and fatigue life of different types of joints (T-joints, L-joints, etc.).

The failure mechanism of Z-pins depends on different factors such as Z-

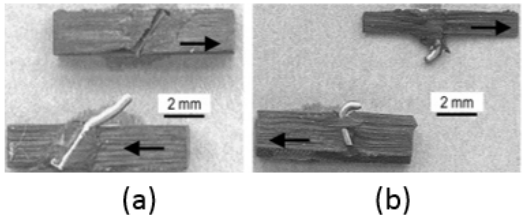


Figure 2.13: Effect of loading (a) "with the nap" and (b) "against the nap" on titanium Z-pin failure. Obtained from Ref. [10]

pin material, loading mode, loading rate and loading direction. The Z-pin tends to fail by complete pull-out at pure mode I and low mode mixity. When the Z-pin fails by complete pull-out most of the energy (more than 95%) is absorbed during the sliding friction phase. At mode II loading the Z-pin tends to fail by shear out (carbon fibre Z-pin) or tensile necking (metallic Z-pin). Under mixed mode loading, snubbing tends to enhance the friction force as the Z-pin slides out of the laminate.

2.4 Z-pin Models

Extensive experimental work has shown that Z-pinning is effective through thickness reinforcement method. The development of accurate modelling tools that aid design and analysis of Z-pinned laminates is necessary for the wider adoption of Z-pinning at industrial level. As the Z-pin is an order of magnitude smaller than the laminate it is embedded in, a multi-scale approach (Ref. [38]) might be necessary to efficiently simulate the crack bridging performance of Z-pins. The levels of this multi-scale approach can be defined as:

1. Meso-1: Characterising and predicting the bridging performance of a single Z-pin embedded in a delaminated composite.

2. Meso-2: Modelling the performance of Z-pin arrays in bridging delamination. At this scale the variability in Z-pin properties should be taken into account. Additionally, a level of homogenisation is required to smear the mechanical properties of the interacting Z-pins.

3. Macro-scale: The bridging performance of Z-pins is considered at full structural level. At this scale it is necessary to introduce further homogenisation to reduce the computational cost.

Depending on the scale that the Z-pin performance is being captured, different modelling approaches can be used. These approaches can be summarised into three main categories as:

1. Analytical model: Where a closed form analytical solution was derived to describe the bridging performance of Z-pins.

2. Semi-Analytical model: Where a mathematical equation has been developed to describe the bridging performance of the Z-pin, but these equations does not have a closed form solution and need to be solved numerically.

3. Numerical models: The Z-pin and the laminate are explicitly modelled using techniques such as Finite Elements or Peridynamics.

The different approaches used (Analytical to Detailed models) at different scales (meso-1 to macro) has been extensively reviewed and are presented in the upcoming sections. It is worth noting that models for simulating the bridging response of stitches as well as Z-pins were reviewed due to the similarity between the bridging response of the two through thickness reinforcing methods.

2.4.1 Analytical Models

The sophisticated mechanisms governing the bridging performance of through thickness reinforcement results in a sophisticated solution space even for the most generally posed problem. However, in a very limited and certain cases a closed form analytical solution can be attained.

Cox (Ref. [91]) proposed a model for Mode II crack bridging performance of a fibrous tow (a rod or stitch). The model assumes that the tow is inserted perfectly orthogonal and the loading is a pure mode II loading. A pure mode II loading is practically impossible to achieve as some opening displacement will be present. However, this is a good enough approximation for high mode mixity values.

A subsequent paper (Ref. [92]), demonstrated that it is possible to obtain a closed form solution for the bridging law in the case when the debond region (called "slip zone" in the paper) does not reach the end of the rod. However, this is a very limited and specific region in the bridging mechanism. Moreover, the Z-pin remain bonded to the laminate at very small displacements while most of the energy dissipated by Z-pin is through bending deformation up to failure under mode II loading. Although this analytical model is a computationally efficient method, it has very limited practical application

when looking at Z-pin bridging performance.

Dickinson et al. (Ref. [93]) highlighted the presence of empirical models to predict performance of stitched materials. These empirical models predicted tension, compression and compression after impact to a good degree of accuracy. However, these models did not address the through thickness bridging performance of the fibrous stitch. Thus apart from the closed form solution presented in Ref. [92], the literature is devoid from any other closed form analytical solution to describe the bridging performance of through thickness reinforcement.

2.4.2 Semi-Analytical Models

Several semi-analytical models have been proposed to describe the bridging performance of through thickness reinforcement (stitch, rod etc.) at meso level 1 and 2 scales. Since stitching was developed earlier than Z-pinning, the earlier semi-analytical models address the bridging performance of stitches. However, the bridging mechanism for stitch and Z-pins are similar allowing modelling knowledge for stitches to be read across to Z-pinning.

Meso-1 level

Jain et al. (Ref. [61]) proposed a simple micro-mechanical model to study the mode I bridging performance of through thickness fibrous reinforcement (specifically stitching) in double cantilever beam (DCB). Two versions of the same model were presented in Ref. [61], the difference between the two versions is the assumption of whether the stitches are interconnected. To remove surface in-plane waviness, stitching loops may be ground off and hence supporting the assumption that the stitches are not interconnected. The model proposed does take into account the elastic extension of the stitch, debonding and frictional pull-out. Initially, the stitch is assumed to be perfectly bonded to the laminate. Thus debonding crack is assumed to propagate cylindrically around the stitch as a pure mode II crack. To model the sliding friction response, the friction shear stress is assumed to have a constant value which is not accurate. In particular constant friction force is invalid when modelling Z-pin bridging force due to the presence of "snubbing" as well as experimentally observed non constant friction in pure sliding (i.e. without

snubbing). Although the model developed was successfully used to examine stiching parameters (such as stitch density, thread diameter etc), it was not validated against experimental results.

Dransfield et. al. (Ref. [94]) validated the model developed in Ref. [61] against experimental results. The model showed good correlation with experimental results in predicting improvement in mode I delamination toughness.

The first model addressing Z-pin bridging performance was proposed by Cox in Ref. [91]). The model in Ref. [91] described the traction-displacement response of Z-pins subject to pure mode II loading. This model was further developed in Ref. [92] to model the bridging performance taking into account the through thickness reinforcement insertion angle and mixed mode loading cases. The model proposed by Cox in Ref [92] assumes that the through thickness reinforcement can carry axial force, but the shear behaviour is perfectly plastic. Moreover, it models the interaction between the insert and the laminate as that of a rigid punch through a perfectly plastic medium. However, composite Z-pins undergo brittle failure when subject to mixed mode loading beyond the transition region rendering the assumption of plastic shear behaviour of the TTR invalid in this case. In addition, assuming that the laminate is perfectly plastic when modelling the interaction would only be valid in unidirectional laminate assuming that the Z-pin only ploughs through the resin pocket. Furthermore, the model in Ref. [92] assumes that the friction is uniform along the fibrous reinforcement length which is not the case in practice. Assumption of uniform friction is particularly invalid for Z-pins, as snubbing can result in significant enhancement in the friction value. The model was used to study the effect of different parameters on the bridging response but was not validated against experimental results.

The model proposed in Ref. [92] was further developed in Ref. [84] to include the effect of snubbing which is of significant importance when modelling Z-pin bridging performance. The Z-pin in Ref. [84] is assumed to be fully debonded with friction acting along its length. The friction acting along the Z-pin is split into two zones, an initial friction zone (τ_i in the undeflected portion of the Z-pin and an enhanced friction zone (τ_e) in the deflected part of the Z-pin. By defining the enhancement ratio (μ_e) and the initial friction value (τ_i), the enhanced friction (τ_e) value can be obtained (see eq. (2.1)). Although, modelling the enhanced friction term adds an important level of

detail, the assumption of uniform friction is not valid particularly along the deflected portion of the Z-pin. In addition, the model was not validated under pure mode I or mixed mode loading (below transition region) were friction can be of primary importance. However, the model was validated against experimental results under mode II loading and showed good agreement.

$$\mu_e = \frac{\tau_e}{\tau_i} \tag{2.1}$$

A conceptually similar model to that by Cox et al. (Ref. [84]) was proposed by Plain et al. (Ref. [95]). The model proposed is specifically developed for a stitch TTR where the rope-like behaviour is assumed (i.e. no ability to support axial bending). Although such an assumption is feasible for a stitch, it is not appropriate for Z-pins where the bending stiffness is relatively high.

A different approach was developed by Tong et al. (Ref. [96,97]) to model the bridging performance of a metallic Z-pin. The model assumes that the TTR rod behaves as an Euler-Bernoulli beam embedded in an elastic-plastic foundation. However, the solutions were only presented for pure mode I and II loading. The model studied the effect of different parameters but was not validated against experimental results. A similar approach was followed by Bianchi et al. (Ref. [98]) to model single-pin pull-out under pure mode II loading, where the Z-pin material was T300/BMI (i.e. composite Z-pin).

For a multi-directional laminate, it is important to observe that the Z-pin might not be able to plough through the laminate as the Z-pin is supported by ply fibres in all directions. Thus it is expected that the laminate behaves as an elastic foundation for the TTR, especially that the fibres are linear elastic up to failure. Allegri et al. (Ref. [99]) developed a novel model to describe the traction-displacement response of Z-pin inserted at an angle to the delamination plane and subjected to mixed mode loading. The model represent the Z-pin as an Euler-Bernoulli beam embedded in elastic foundation. Both residual and snubbing friction were incorporated into the model. The residual friction was modelled based on an empirical relationship. The "snubbing" friction enhancement was proportional to the punch resistance force arising from the Z-pin pushing against the laminate fibres. The punch resistance force is linearly proportional to the deflection of the Z-pin relative to the laminate (elastic foundation assumption). The results obtained were validated against experimental results and were found to be in good

agreement. Additionally, the model was able to predict the transition region observed experimentally. However, the model neglected the rotation of the Z-pin (linearised assumption when deriving governing equation) and hence does not take into account the potential coupling between axial and lateral forces developing in the Z-pin.

The model in Ref. [99] was further simplified by Yasaee et al. (Ref. [85]) reducing the number of required material parameters. In this model, a power law empirical relationship was used to model the tangential friction force per unit length in order to capture the Z-pin frictional performance as a function of its embedded length. The proposed model is able to predict relatively accurately the bridging performance of the Z-pin at different loading modes and for various composite laminate thickness.

All of the models discussed above are concerned with the bridging performance under quasi-static loading. The literature does not have any TTR model that captures the dynamic response. However, Zhang et al. (Ref. [100]) and Liu et al. (Ref. [101]) presented a rate dependent model for a single fibre pull-out. The model is not for a through thickness reinforcement nor can it be used for mixed mode or mode II loading. Nonetheless, the physics presented is applicable to through thickness reinforcement particularly under mode I loading. Friction is known to be rate dependent (Ref. [100, 102]) and thus rate effects need to be taken into account when modelling single fibre pull-out response. The rate dependent friction was modelled using Rice's friction model (Ref. [102]). The parameters for the rate-dependent friction model were not obtained based on experimental results but rather presented as suitable values for a numerical example. Thus the model was used to investigate the effect of increasing loading rate but was not validated. In addition, the loading rates presented in Ref. [100] are of the order of mm/mins, which is not representative of the level of loading rate that could be witnessed by an aircraft in service, for example as a result of a bird impact.

Meso-2 level

Z-pinned coupons such as double cantilevered beam (DCB), end notch flexure (ENF) and mixed mode bending (MMB) have been used to investigate the array behaviour of Z-pins at larger scale, namely meso-2 level. Different models have been developed to study the array behaviour of Z-pins in order

to compliment the experimental work.

Dransfield et al. (Ref. [94]) used the micro-mechanical model developed by Jain et al. (Ref. [61]) to predict the improvement in mode I fracture toughness in stitched DCB samples. The model prediction of mode I fracture toughness as a function of stitch density and diameter was accurate for the case of a Kevlar stitch but less accurate for the case of Carbon fibre stitch. The author attributed the underestimation of mode I fracture toughness in case of carbon fibre to either lower thread strength value or high thread stiffness value.

A simple model was proposed by Ratcliffe et al. (Ref. [103]) to describe the mode I bridging performance of Z-pins in a DCB coupon. The Z-pins were modelled as discrete springs connecting both arms of the DCB coupon. Progressive stiffness degradation was used to model the pull-out response of the Z-pins while the energy release rate associated with delamination growth in the coupons was computed through the use of linear elastic fracture mechanics. The results obtained from the simulation were compared to experimental result from literature and were found to be in good agreement. A similar model was developed by Byrd et al. (Ref. [104]) to study the effect of Z-pins on the energy release rate and fatigue. However, the model developed is limited to relatively short cracks.

Robinson et al. (Ref. [105]) developed a mode I bridging performance model of Z-pin in DCB coupon to investigate the validity of data reduction methods for Z-pinned coupon. The Z-pin pull-out is modelled based on experimental data and not based on a Z-pin bridging model. A bilinear bridging model is obtained by ensuring that the area under load-displacement graph is the same as that of its experimental counterpart. The model showed good prediction capability in the developed zone (zone in which both the trailing edge and the leading edge of the bridged zone are advancing), but the prediction was poor in the developing phase (more Z-pins becoming engaged by the crack) of the bridging response.

A similar model was developed by Song et. al (Ref. [106]) to model the bridging performance of Z-pinned DCB coupons. The bridging traction was smeared along the Z-pin row with the consequent methodology similar to other models discussed. The outcome of the model was compared to experi-

mental and finite element results and was seen to be in good agreement.

Most of the Meso-2 level semi-analytical models available in the literature were seen to be mainly concerned with mode I delamination bridging performance with a lack of Mode II and mixed mode semi-analytical models. In addition, none of the models proposed address the dynamic bridging performance of Z-pinned laminates. Nonetheless, these semi-analytical models offers instructive insight into the bridging performance of Z-pinned laminate while being computationally cheap relative to other alternatives.

2.4.3 Numerical Models

Numerical methods can be an alternative to semi-analytical approach, providing more detailed insight into the bridging behaviour but at a rather increased computational cost. Finite element is a well established numerical technique used to simulate structural response. A more recently developed method known as Peridynamics can also be used to model Z-pinned laminates. Peridynamics is discussed in detail in chapter 3. Based on these methods, various modelling approaches were developed to simulate the Z-pin bridging performance at meso-1 and meso-2 level.

Meso-1 level

Meo et al. (Ref. [107]) developed a finite element model to simulate the mode I bridging response of a single Z-pin. In this model both the Z-pin and the laminate were meshed using solid elements. The thermal stress was modelled by imposing an initial pressure contact between the TTR and the matrix. During the pull-out response the friction model consisted of two parts, the residual friction part (being a constant value) and the coulomb enhancement part (accounting for friction enhancement due to lateral deflection). The shear stress value was limited to a maximum value (τ_{max}), thus when τ_{max} is reached sliding is assumed to start. The results obtained from the analysis was in good agreement with experimental results.

Cui et al. (Ref. [108]) developed a finite element model capable of simulating Z-pin bridging performance under mixed mode loading. The model was able to capture many details of the Z-pin bridging response. This include modelling the resin pocket, splitting of the Z-pin, snubbing, pull-out

and shear out failures. In order to model splitting, cohesive elements were used to seed candidate splitting planes. However, the actual position of the splitting plane is a function of the stress field. Consequently, an inherent drawback of this model is its mesh dependency (the final result depends on the assumed splitting density and its relative positioning). Furthermore, the bridging performance was modelled based on a Z-pin inserted orthogonally in a UD laminate. Practical application of composite materials usually use multi-directional laminate layup (typically quasi-isotropic). The behaviour of Z-pin in multi-directional laminate are known to be different to that in UD laminate (Ref. [83]). The author in Ref. [108] attempted to model Z-pin inserted in cross ply laminate by giving the resin pockets the properties of a 90° ply, but this is not ideal as the resin pocket properties are very different from that of cross ply. In addition, the model did not take into account the misalignment of the Z-pin. Nonetheless, the model was validated against mode I and II experimental results and shown to be in good agreement.

Zhang et al. (Ref. [11]) developed a 3D finite element model to predict the bridging performance of Z-pin inserted into muli-directional laminate and subjected to mixed mode loading. A star-like ply-level mesh (see fig. 2.14) was used to describe the in-plane micro-structure of Z-pinned laminate. This allowed capturing detailed features such as misalignment angle, resin pocket and the fibre waviness surrounding the resin pocket. In addition, progressive debonding of Z-pin/laminate interface; friction post debonding stage and

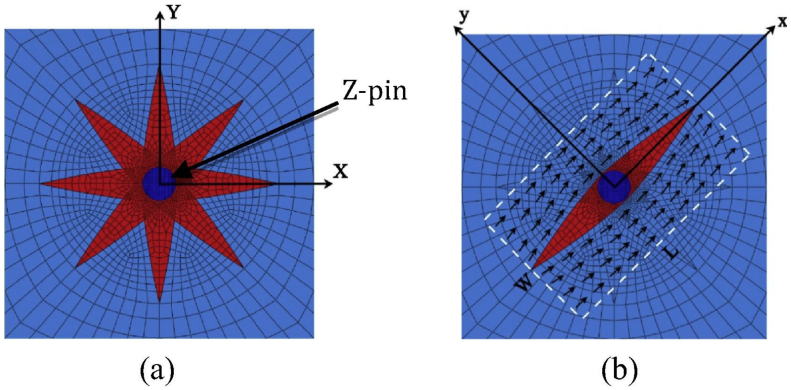


Figure 2.14: (a) Laminate stack view (b) Showing fibre waviness in vicinity of resin pocket. Obtained from Ref. [11]

splitting of the Z-pin were taken into account. Interestingly, this model also considered the post cure cool down effect which shows that thermal stresses arising from the post cure cool can damage the Z-pin laminate interface. Consequently, the Z-pin interface to the laminate is not perfectly bonded but rather largely weakened and partially failed. The model was validated against experimental results and shown to be in good agreement. However, it is limited to quasi-static loading and computationally expensive; the model took 4 days to run on 64 core supercomputer.

A meso-1 level FE model is a highly practical method of complimenting experimental observation to capture complex Z-pin behaviour. Additionally, it is useful in assessing the relative influence of different failure mechanisms under different loading configurations. However, the computational costs associated with such models is significantly larger than that associated with semi-analytical models. The significance of such cost becomes clear given that meso-1 model is just a pre-requisite to meso-2 level and macro-scale models where the number of Z-pins inserted ranges from tens to thousands of Z-pins. Therefore, there is a need for a trade-off between physical accuracy and computational resource available. Hence the need for a "reduced-order" semi-analytical method developed as part of a multi-scale approach becomes more appealing.

Meso-2 level

At meso-2 level two main features need to be considered when modelling the bridging performance of Z-pins:

1. The presence of Z-pins do not influence the onset of delamination (Ref. [32, 109–111]).
2. Large scale bridging is exerted over multiple rows of inserted Z-pins.

Therefore, a correct representation of damage sequence in pinned laminates is required; this is represented by ply interface fracture (unaffected by Z-pins) followed by large scale bridging that develops as the crack grows.

Cartie (Ref. [32]) presented an FE model capable of simulating the bridging performance of Z-pinned ASTM standard coupon. In this model, the Z-pins were modelled as non-linear springs with progressive softening response

during the pull-out stage. The j-integral method was used to evaluate the energy release rate, which links the meso-1 and meso-2 level analysis. A similar approach was followed by Grassi et al. (Ref. [112]) where the Z-pins were modelled as non-linear springs, however, the energy release rate was computed using the virtual crack closure technique. To model the response of Z-pinned joints, similar FE model formulation was devised by Allegri et al. (Ref. [113]). This method incorporated a meso-1 level constitutive Z-pin bridging model. The FE simulation was validated against experimental results yielding satisfactory agreement.

On the other hand, the possibility of using nodal forces to model the bridging action of Z-pins was demonstrated by Cartie et al. in Ref. [110]. This potentially offers the possibility of more efficient multi-scale approach by using semi-analytical models at meso-1 level to develop bridging maps that can be used at meso-2 level. Yan et al. (Ref. [114, 115]) developed FE models to simulate the Z-pin bridging performance subject to mode I and II loading by using DCB and ENF specimens respectively. The Z-pins were modelled as non-linear springs with critical opening displacement criterion used to switch from debonding to pull-out response. The model was verified against experimental results and shown to be in good agreement. Dantuluri et al. (Ref. [116]) presented an FE model to simulate the performance of Z-pinned DCB coupons. Initially, the Z-pin was modelled as discrete non-linear spring element. However, to reduce computational time the author introduced an equivalent cohesive model to substitute the non-linear springs. Similarly, Kravchenko et al. (Ref. [117]) used non-linear spring to model the Z-pin bridging performance in pinned laminate. In this model, the bridging performance of individual Z-pin was characterised experimentally and used at the meso-2 level to conduct the FE analysis. Using a physically based semi-analytical model can reduce the dependency on conducting experimental testing to obtain the bridging performance of individual Z-pin. The Z-pin bridging performance would need to be simulated in variety of cases under different loading condition. Therefore, conducting individual Z-pin testing each time to use in higher scale modelling would not be practical.

Bianchi et al. (Ref. [98, 118]) modelled the bridging response of Z-pinned DCB and ENF specimens by using two different cohesive element properties. Enhanced toughness was given to the cohesive elements in the Z-pinned region to exemplify the bridging action exerted by the Z-pins; while other

cohesive elements had the standard properties of the unreinforced laminate. The cohesive zone model in the Z-pinned region was obtained from a traction-separation law based on meso-mechanical model for Z-pin pull-out. Such an approach avoids the application of concentrated loads. Hence, mesh dependency is removed and computational cost is reduced, however, accuracy might be compromised. A similar approach was followed by Cui et al. (Ref. [108]) to model mixed mode response of Z-pinned laminates.

Mohamed et al. (Ref. [119]) implemented a multi-scale approach to model the Z-pin bridging performance under mode I, mode II and mixed mode loading using DCB, ENF and MMB coupons respectively. In this multi-scale approach, single pin testing was conducted to characterise the bridging performance of Z-pins. The testing outcome is used to calibrate and validate a semi-analytical model. The semi-analytical model is used to create a bridging map that consists of the bridging force applied by the Z-pin as a function of the opening and sliding displacements. The bridging map is used to create a special purpose cohesive element with a generalised traction-displacement characteristics. The cohesive zone formulation is based on superposition of cohesive response of the base resin and the bridging response of the Z-pin which is deployed in a smeared sense over the fracture surface. The bridging performance predicted by the model was in excellent agreement with experimental results in the mode I (DCB) and mode II (ENF) loading cases. In the mixed mode loading (MMB) there is a good agreement between experimental and numerical results. However, the model was less able to capture the maximum load and displacement at failure. This was attributed to the deterministic nature of the model where the variability of the input data was not accounted for. The model presents a suitable multi-scale modelling approach to simulate the performance of Z-pinned laminates. Such an approach is more computationally efficient then explicitly modelling individual Z-pins. Nonetheless, the model was only tested under quasi-static loading due to the absence of semi-analytical model capable of capturing the bridging performance under dynamic loading.

More recently, Baber et al. (Ref. [120]) adopted a new approach to model Z-pinned laminates subject to impact loading. The new method is based on Peridynamic theory, a non local formulation that allows damage initiation and propagation at multiple sites, with arbitrary paths inside the material. Essentially, damage is part of the constitutive model in Peridynamic formulation (discussed in details in Chapter 3). In this approach, the fibre, matrix

and Z-pins are represented explicitly allowing individual plies to be modelled. Therefore, this approach allows the modelling of laminate with arbitrary fibre orientation. The resin eyelet around the Z-pin is assumed to be cylindrical in order to simplify the modelling attempt. The model was able to predict the delaminated area to a satisfactory degree with acceptable match between the model and experimental results. Nonetheless, the model did not take into account the observed failure mechanisms of Z-pins and their response under different loading modes. In the proposed modelling approach, Z-pins can only fail by breaking of bonds within the Z-pin or with surrounding matrix, hence allowing debonding, splitting and shear out failures. However, under mode I loading the Z-pin tends to pull-out and dissipates significant energy due to friction. Although, under impact loading prominent crack propagation occur in mode II, making it reasonable to use proposed approach, the absence of mode I pull-out and consideration of friction renders this model in need of further development. In addition, the proposed method required 140,000 points to model a small plate which is computationally expensive. Thus, such an approach is prohibitively expensive when modelling larger Z-pinned structures.

2.4.4 Summary

Different modelling approaches have been proposed in literature to capture the Z-pin bridging performance at different scales, namely meso-1, meso-2 and macro levels.

Analytical models were found to be very limited and applicable in very specific cases. Despite the computational efficiency of this approach, they cannot capture the full spectrum of Z-pin bridging performance under different loading conditions.

Various semi-analytical models were proposed in literature to capture the bridging performance of Z-pinned coupons. The models reviewed can capture performance at different scales and some models are able to predict performance under mixed mode loading. However, none of the models developed were suitable for predicting the dynamic bridging performance of Z-pins.

Numerical models proposed in literature were able to capture the complex

behaviour of Z-pins under different loading conditions. The majority of these models were based on finite element analysis while one model was based on Peridynamic formulation, which is a new method still in its academic infancy. While numerical models provided a detailed analysis of Z-pinned laminates, it is agreed that such an approach is computationally expensive without utilising a multi-scale approach. The computational cost hinders the adoption of numerical models at larger scales for the analysis and design of Z-pinned structures.

2.5 Conclusions

Laminated composite materials are susceptible to delamination as the plies are bonded together through the matrix which is the weak component of carbon fibre reinforced composites. Many methods are available in literature to provide through the thickness reinforcement of laminated composites. The majority of these methods consists of inserting a fibre in the through thickness direction. The known TTR techniques include 3D weaving , braiding, knitting, stitching, tufting and Z-pinning. The later (Z-pinning) is the only method suitable for use in prepreg composites which are more suited for use where high fibre volume fraction is needed.

Z-pins are orthogonally inserted rods in the through thickness direction. Two main methods were found in literature to insert Z-pins. The more widely known method is the Ultrasonice Z-fibre Insertion (UAZ) process, which can be used at industrial scale but lacks control of the Z-pin insertion angle. The other technique is known as the Direct Insertion (DI) method developed and patented by Rolls-Royce. The DI method can achieve a more controlled insertion angle and is suitable for application at industrial scales.

The Z-pins effectively nails the laminate together improving the through thickness strength. Extensive experimental investigation of the performance of Z-pinned laminates is available in literature. The Z-pins were shown to significantly improve mode I fracture toughenss (20 folds increas reported) and moderately improve mode II fracture toughness (5 folds increase reported). In addition, Z-pinned laminate had reduced delamination damage compared to unpinned laminate for the same impact energy. The level of delamination

damage reduction depends on impact energy, but as much as 64% reduction in delamination damage is reported in literature. Consequently, Z-pinned laminate are reported to have higher compression after impact strength. On the other hand, Z-pinning alters the micro-structure of laminated composites introducing fibre waviness and creating resin rich eyelet in the vicinity of the Z-pin. These changes degrade the in-plane properties of Z-pinned laminates such as in-plane compressive strength. Thus a compromise is necessary when deciding the Z-pinning areal density. Generally, it is accepted that a 2% Z-pin areal density can achieve optimal trade-off between improved fracture toughness and reduction in in-plane properties.

Different modelling approaches were presented in literature to simulate the bridging performance of Z-pins. A multi-scale modelling approach is identified when reviewing literature. A meso-1 level modelling is concerned with simulating the performance of a single Z-pin. While meso-2 level modelling addresses the array behaviour of Z-pins. This is particularly important where the mixed mode loading is taking place in the transition region. Macro-scale modelling is used at full structural level, where homogenisation is introduced to reduce the computational cost. Although, it was clear in literature that Z-pin response is rate sensitive, particularly in mode I upto the transition region, the literature is devoid of any reduced order model capable of simulating Z-pin bridging response under high rate loading. Consequently, the main objective of this thesis is to understand the meso-mechanics of Z-pin bridging response at high loading rate. In addition, a suitable model is developed to capture the Z-pin bridging performance at high rate and subject to different mixed mode loadings. Furthermore, the model developed is capable of capturing array behaviour of Z-pins at a reduced computational cost.

Chapter 3

Peridynamic Formulation and Validation

3.1 Introduction

Solid mechanics equations of motion can be solved by using either local or non-local formulations. In local formulation, a material point is assumed to interact only with other material points in it's immediate vicinity. Classical continuum mechanics is a very well known application of the local formulation, where the stress at a point depends on the state of deformation at that point only. The resulting mathematical structure of classical mechanics assumes that the body remains continuous as it deforms. Consequently, the presence of discontinuity (such as crack) causes the mathematical structure to break down. The mathematical breakdown is attributed to the use of spatial partial derivatives in the local formulation which are not defined at discontinuities. Therefore, crack initiation and propagation are not part of the governing equations in classical continuum mechanics.

The classical continuum theory has been successfully applied to a wide range of engineering problem, especially by employing the Finite Element Method (FEM). However, the applicability of the locality assumption is questionable across different length scales. The atomic theory makes it clear that long-range forces exist causing the assumption of locality to break down. The validity of the local assumption can also be questionable even at the macro-scale where the presence of certain features and micro-structures can

influence the entire macro-structure. These shortcomings motivates the development of non-local formulation.

In non-local formulation, a material point can interact with other material points within a certain radius r_h as shown in fig. 3.1. The material points within the radius r_h of point z are known as the family of z, H_z. Thus the non-local formulation establishes a connection between molecular and classical continuum mechanics. In the limit as the radius r_h tends to infinity, the non-local theory becomes a continuous version of molecular dynamics. In the limit as the radius becomes infinitely small the non-local theory would approach the classical continuum mechanics model.

Many non-local theories have been proposed over the past decades. The proposed theories can be generally split into two types. The first type involves some form of higher order displacement gradient and spatial integrals as introduced by Eringen (Ref. [121]) and Eringen et al. (Ref. [122]). The presence of derivatives in this type of non-local theory retains the spatial derivative in the mathematical formulation. Thus the description of discontinuity (such as cracks) remains problematic. The second type avoids this difficulty by using displacement fields instead of their derivatives. This type of non-local theory was first developed by Kunin (Ref. [123]) and Rogula (Ref. [124]). Both of these proposals were derived for one dimensional cases. Recently, a more general formulation was proposed by Silling (Ref. [125]). This new formulation is known as Peridynamics theory. The Peridynamics theory does not require spatial derivatives, is applicable in two and three dimensional spaces, provides non-linear material response in regards to displacements and includes damage as part of the non-local formulation.

Peridynamic theory is used in this thesis to formulate the reduced order model for the bridging response of the Z-pin. This chapter presents a review of peridynamic theory, its advances and areas of application. In addition, the peridynamic rod and Timoshenko beam formulations are derived and presented in this chapter. These formulations forms the basis of the reduced order model describing the Z-pin bridging response. Thus, the derived formulation is validated to be correct as presented in this chapter. It is worth noting that the peridynamic beam formulation presented here results in slightly different bond constants to that presented in literature. The formulation presented in this chapter is the correct one.

3.2 Peridynamics - A Review

Peridynamic theory is a reformulation of the solid mechanics equations of motion into an integro-partial differential form. The use of displacements instead of displacement derivatives coupled with employing spatial integral equation in peridynamic theory results in the equation of motion being defined at discontinuities such as cracks. In addition, material damage forms an integral part of the constitutive laws in peridynamic theory. The peridynamic theory, being defined at discontinuities with damage integral to constitutive laws, allows for crack initiation and propagation with an arbitrary path without the need for special crack growth treatment. Consequently, the peridynamic theory is better able to model cases where crack location is not known a priori.

The peridynamic theory was first proposed by Silling (Ref. [125]) in the year 2000. In the proposed theory a material point ($\mathbf{z}$) interacts with other material points ($\mathbf{z}'$) within a certain distance known as the horizon ($\mathbf{H_z}$). As shown in fig. 3.1, the material body is divided into a set of points, the particles within a distance r_h from the point of interest z (colored red in fig. 3.1) forms the horizon of z (H_z). The material points in the horizon of z are referred to as z' (colored orange in fig. 3.1). All material points in the horizon of z exchange momentum with material point z. Thus, the general governing equation in peridynamic formulation becomes:

$$\rho(\mathbf{z})\frac{\partial^2 \mathbf{u}(\mathbf{z},t)}{\partial t^2} = \int_H \left[\mathbf{t}_{\mathbf{z}\mathbf{z}'} - \mathbf{t}_{\mathbf{z}'\mathbf{z}}\right] dH + \mathbf{b}(\mathbf{z},t) \tag{3.1}$$

Where, ρ is the material density, $\mathbf{u}(\mathbf{z},t)$ is deformation vector at location $\mathbf{z}$, $\mathbf{t}_{\mathbf{z}\mathbf{z}'}$ is the force density per unit volume squared exerted by $\mathbf{z}$ on $\mathbf{z}'$, $\mathbf{t}_{\mathbf{z}'\mathbf{z}}$ is the force density per unit volume squared exerted by $\mathbf{z}'$ on $\mathbf{z}$, $\mathbf{b}(\mathbf{z},t)$ is the body force per unit volume acting on material point $\mathbf{z}$, and H in the integral limit refers to integration over the horizon of material point $\mathbf{z}$. The integral on the right hand side of eq. (3.1) is the principal difference in the expression of the governing equation when compared to the partial spatial derivative in the classical continuum mechanics.

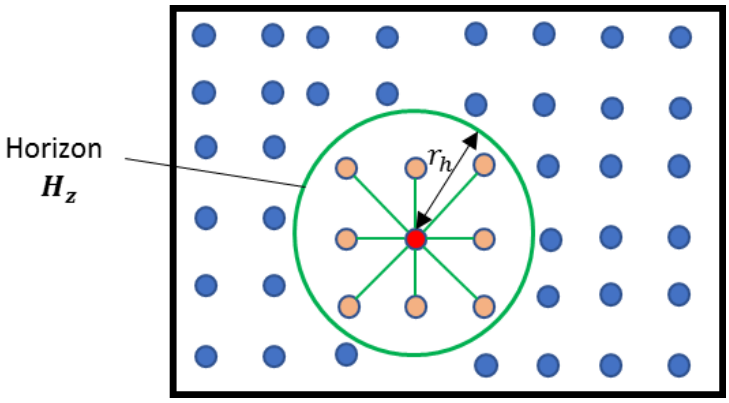


Figure 3.1: Illustration of particle interaction in peridynamic theory.

In the original formulation proposed by Silling (Ref. [125]), later coined the "bond based" peridynamic, the vectors of force density per unit volume ($\mathbf{t_{zz'}}$ and $\mathbf{t_{z'z}}$) are assumed to be equal in magnitude and parallel to the position vector in deformed state as shown in fig. 3.2a. This assumption was used to satisfy the requirement for balance of angular momentum. Such an assumption resulted in a constraint on material properties requiring the Poisson's ratio to be equal to 0.25 for isotropic material. Also, it is not suitable to capture plastic incompressibility as it is not able to distinguish between distortional and volumetric deformation.

To address the limitations arising from bond-based peridyanmics, Silling et al. (Ref. [126]) proposed a more general formulation, coined the state-based peridynamics. In state-based peridynamics the deformation of a material point depends collectively on the deformation of all bonds connected to the point. Consequently, the force densities arising from the pairwise interaction does not necessarily have to be equal and opposite. The general case where the pairwise force density are of unequal magnitude and not parallel to the deformed position vector (see fig. 3.2c) is referred to as "non-ordinary state-based" peridynamics. The case where the pairwise force density vectors have unequal magnitude but are parallel to the deformed position vector (see fig. 3.2b) is referred to as the "ordinary state-based" peridynamics. The state-based peridynamics formulation has successfully addressed the limitations of bond based peridynamics, allowing for materials with any Poisson's ratio and able to capture the plastic incompressibility condition.

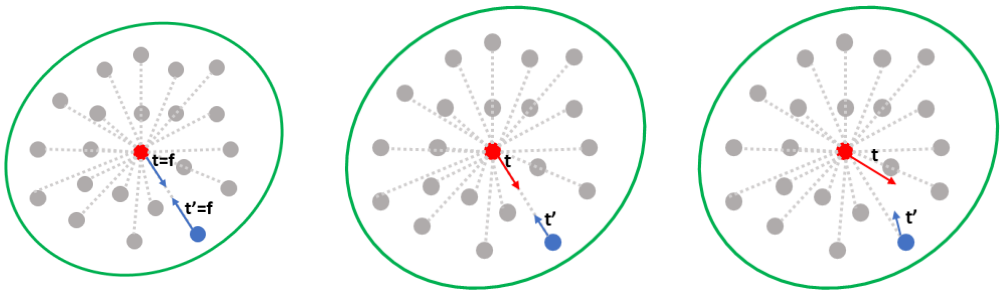


Figure 3.2: Illustration of pairwise interaction in (a) Bond-based peridynamics (b) Ordinary state-based peridynamics (c) Non-ordinary state based peridynamics.

Although the peridynamic (PD) theory have been proposed relatively recently, a significant amount of work has been conducted to develop and implement the theory. In terms of material behaviour, peridynamics has been successfully used to model linear and non-linear elastic behaviour (Ref. [127]), plastic behaviour (Ref. [126,128]), viscoelastic (Ref. [129–131]) and viscoplastic (Ref. [131, 132]) material behaviours. Another important consideration is the choice of the horizon size. The horizon defines the degree of non-locality in PD theory. Bobaru et al. discussed the meaning and selection of the horizon in Ref. [133]. The horizon should be chosen to represent a characteristic length dimension as discussed by Silling et al. (Ref. [134]). At nano-scales the horizon size is chosen to represent the maximum distance of physical interaction between molecules/atoms. However, at the macro-scale, the horizon does not have a physical correspondence and can be chosen at convenience (Ref. [135]). A benchmark study was conducted in Ref. [135] to determine the optimal size for the horizon at macro-scale. Based on this study it was recommended to use a horizon size $r_h = 3\Delta$ where Δ is the grid spacing.

Analytical solutions are difficult to obtain in PD theory due to the integro-differential mathematical structure. Nonetheless, few analytical solution for very specific cases exist in the literature. An example of analytical solution using PD theory is that presented in Ref. [136] for an infinite bar subjected

to a self-equilibrated load distribution. Due to the difficulty obtaining an analytical solution, numerical methods are more widely used to solve the governing equation in PD theory. Silling et al. discussed techniques that can be used to solve the PD equations, stability criterion for convergence and degree of accuracy for a uniform grid discretisation in Ref. [134]. To improve the accuracy and computational efficiency of the numerical method various ideas have been investigated. These ideas include using a mixed explicit-implicit time integration scheme (Ref. [137]), using non-uniform grid and non-uniform horizon (Ref. [138, 139]), and using adaptive trapezoidal integration scheme (Ref. [140]). In addition, various studies (Ref. [141–144]) had proposed different ways of combining the PD theory and local theory in order to improve computational performance. The motivation behind these proposals is that the numerical solution for the PD theory governing equations is more computationally expensive than those based on local theories such as FEM.

The presence of inertial terms in the PD theory makes it inherently suitable for dynamic problems. However, using a suitable scheme to obtain the steady state solution of the dynamic response makes it possible to use PD theory to solve quasi-static problems. Killic et al. (Ref. [145]) has presented an extension of the dynamic relaxation method to obtain steady-state solution of non-linear peridynamic equations in the shortest possible time. This method is referred to as the adaptive dynamic relaxation (ADR).

Damage prediction is part of the constitutive formulation in PD theory. Crack initiation, coalescence and propagation can be easily prescribed without the need for external criterion by failing individual bonds. For the original brittle material, Silling et al. (Ref. [134]) defined a critical stretch by relating it to the critical energy release rate. Once the critical stretch is exceeded the PD bond is deleted. Foster et al. (Ref. [146]) defined an alternative critical energy density by relating it to the critical energy release rate. Similar to the approach by Silling et al. (Ref [134]), once the critical energy density is exceeded the bond interaction is broken.

The developments in PD theory allowed for practical engineering models to be constructed and tested. The PD simulations were able to:

1. successfully predict the crack growth observed in the Kalthoff-Winkler

experiment (Ref. [136]).

2. capture dynamic fracture characteristics such as crack path instability, asymmetries of crack paths, crack branching and successive branching (Ref. [147])

3. model extreme loading of structures such as aeroplane impacting reinforced concrete (Ref. [148])

In addition, PD theory is particularly appealing to model composite materials. This is due to the susceptibility of laminated composites to delamination at locations that are not known a priori. Also, crack propagation (whether delamination, inter or intra laminar cracks) paths are rather arbitrary making it difficult to be captured in the classical continuum approach. PD theory was used to model the low velocity impact damage of laminated composites (Ref. [149, 150]). The results from these simulations showed very good correlation with experimental results while predicting the delamination and matrix damage process in detail. Askari et al. (Ref. [151]) investigated both high and low energy hail impact against a toughened-epoxy, intermediate-modulus, carbon-fibre composite using PD theory framework for the model. Other models presented in literature demonstrated the effectiveness of the PD approach to model and predict damage in composite materials (see Ref. [152–155]). Nonetheless, many of these models are based on detailed 3D modelling proving to be computationally expensive and requiring supercomputers to run the simulations. This motivates the development of reduced order modelling from a peridynamic point of view.

In summary, PD theory is proving to be effective in modelling damage nucleation and crack propagation. Significant amount of work has been done to develop and advance the PD theory but it remains relatively new to the academic world and can be considered to be in its academic infancy. The purpose of this chapter is to formulate and validate the PD framework that will be used to develop the reduced order Z-pin bridging model in later chapters.

3.3 Peridynamic Model Formulation

Developing a reduced order model capable of predicting the Z-pin bridging performance under dynamic loading is the main objective of this thesis. Although full 3D modelling can predict the Z-pin bridging performance, the computational cost remains prohibitively high. In this work, a reduced order 1D model will be used to predict the Z-pin bridging performance. The main 1D elements of interest in this case are the rod and beam elements. Therefore, it is necessary to formulate the peridynamic rod and Timoshenko beam governing equations.

Bond-based PD will be used instead of state-based PD to formulate the governing equations of rod and Timoshenko beam elements. This is motivated by the lower computational cost of bond-based PD when compared to state-based PD. In addition, the limitations of bond-based PD do not concern the proposed modelling approach. The limitation on Poisson's ratio in bond-based PD is not important when opting for a 1D model. Also, the inability of bond-based PD in capturing plastic incompressibility is inconsequential since carbon fibre based Z-pins fail in brittle manner. Thus, using the bond-based PD the rod and Timoshenko beam elements will be formulated in the subsequent sections. These elements will be used in the next chapters to formulate the reduced order Z-pin model.

3.3.1 Rod Formulation

Consider a rod aligned with the z-axis and subjected to a distributed axial load $p(z)$ as shown in fig. 3.3. The deformation of the rod is described by the axial displacement w along the rod z-axis. The bond-based peridynamic

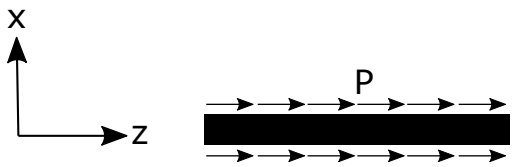


Figure 3.3: A rod subject to distributed force p(z). The rod is aligned with the z-axis.

equation for a rod subject to a distributed axial force $p(z)$ is written as follows [125]:

$$\rho A\ddot{w} + b_w\dot{w} = \int_{H_z} f\left[w(z',t) - w(z,t), z'-z\right] dz' + p(z) \tag{3.2}$$

where $\ddot{w} = \frac{\partial^2 w}{\partial t^2}$, $\dot{w} = \frac{\partial w}{\partial t}$, f in the integral on the right hand-side denotes a pair-wise force density between the material particle occupying the position z and another material particle in the horizon of z occupying position z'; f has the dimension of a force per unit length squared. The domain H_z in Eq. 3.2 denotes the "horizon" of the material particle positioned at z; assume that such a domain is represented by a segment of total length $2r_h$, centred at the particle z, with r_h representing the radius of the horizon. Assuming that the rod has micro-elastic behaviour [134, 136], the pair-wise force f can be expressed as:

$$f = c_a s_w \tag{3.3}$$

where c_a is the axial bond stiffness constant having dimensions of a force per unit length squared and s_w is the "axial stretch" of the PD bond between the material particles. Stretch is the mean of describing the deformation of the PD bond. The axial stretch is defined as:

$$s_w = \frac{w' - w}{|z' - z|} \tag{3.4}$$

where $w' = w(z')$. Assuming the horizon becomes infinitesimally small and using Taylor series expansion, w' can be expressed as:

$$w' = w + w^I(z'-z) + \frac{1}{2}w^{II}(z'-z)^2 + O[(z'-z)^3] \tag{3.5}$$

where O means order of. Substituting eq. (3.5) into eq. (3.4), the axial stretch s_w can be expressed as:

$$s_w = w^I\frac{z'-z}{|z'-z|} + \frac{1}{2}w^{II}|z'-z| + O[(z'-z)^2] \tag{3.6}$$

As the horizon size becomes smaller, the higher order term in eq. (3.6) can be neglected. Substituting eq. (3.6) into eq. (3.3) and neglecting higher order terms, the force density can be expressed as:

$$f = c_a \left[w^I \frac{z' - z}{|z' - z|} + \frac{1}{2} w^{II} |z' - z| \right] \tag{3.7}$$

Adding horizon limits, the integral in eq. (3.2) becomes:

$$\int_{z-r_h}^{z+r_h} f dz' = c_a \int_{z-r_h}^{z+r_h} w^I \frac{z' - z}{|z' - z|} + \frac{1}{2} w^{II} |z' - z| \, dz' = \frac{1}{2} c_a w^{II} r_h^2 \tag{3.8}$$

Substituting the result in eq. (3.8) into eq. (3.2), the PD governing equation becomes:

$$\rho A \ddot{w} + b_w \dot{w} = \frac{1}{2} c_a w^{II} r_h^2 + p(z) \tag{3.9}$$

The derivation of eq. (3.9) was only possible by taking the limit of the horizon going to zero in order to use the Taylor expansion. The limit as the horizon goes to zero converges to the classical continuum formulation. The rod governing equation in classical continuum formulation is:

$$\rho A \ddot{w} + b_w \dot{w} = E A w^{II} + p(z) \tag{3.10}$$

Comparing eq. (3.10) and eq. (3.9), the axial bond stiffness constant can be obtained to be:

$$c_a = \frac{2EA}{r_h^2} \tag{3.11}$$

Thus, substituting the axial bond stiffness in eq. (3.11) into eq. (3.3) and using the axial stretch definition in eq. (3.4), the governing PD equation of motion for a rod element is:

$$\rho A \ddot{w} + b_w \dot{w} = \frac{2EA}{r_h^2} \int_{H_z} \frac{w' - w}{|z' - z|} dz' + p(z) \tag{3.12}$$

3.3.2 Non-linear Timoshenko Beam Formulation

Consider a long prismatic beam of length L made of homogeneous material. The beam is collinear with the z axis of the global zx reference frame shown in fig. 3.4. In bond-based peridynamics, a particle located at z has bonds with all the material points within a characteristic sub-domain H_z denoted

as "horizon". The horizon is the locus of material points with coordinate z' whose distance from the particle at z is less than a characteristic radius r_H, i.e. $H_z \equiv \{z' | z' \in [z - r_H; z + r_H]\}$.

Virtual Work Principle

The deformation of the peridynamic bonds is described by means of stretches, which, generally speaking, give the relative displacements and rotations normalised with respect to the distance separating the material points in the undeformed reference configuration. As shown in Figure 3.4, the deformation of a peridynamic Timoshenko beam is described by two displacement components, i.e. w with respect to z and u with respect to x, and a cross-sectional rotation, which is from now on denoted with θ. It is hereby assumed that cross-section rotations θ are small, but not negligible, i.e. $\theta << 1$. Thus, the derived formulation is that of a Timoshenko beam with moderate rotations and hence referred to as non-linear. Similarly, the displacements are also assumed to be small, i.e. $w, u << L$, together with the associated peridynamic stretches in global coordinates. Considering the deformed configuration of the beam, one can introduce a curvilinear abscissa r spanning the axis. Given the assumptions above, the length of an infinitesimal arc on the deformed beam axis is expressed as:

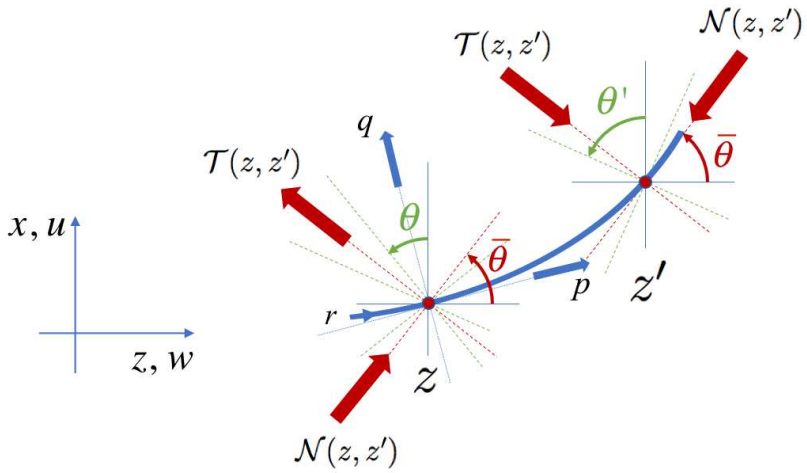


Figure 3.4: Deformation and force densities for a peridynamic beam.

$$dr = \sqrt{(dz + dw)^2 + du^2} \approx dz. \tag{3.13}$$

In the case of a Timoshenko beam and assuming micro-elastic bonds among material particles, the stretches associated with the curvature s_χ, the shear distortion s_γ and the axial deformation s_w respectively are (Ref. [134, 156]):

$$s_\chi = \frac{\theta' - \theta}{|z' - z|}, \quad s_\gamma = \frac{u' - u}{|z' - z|} - \frac{1}{2}(\theta' + \theta)\frac{z' - z}{|z' - z|}, \quad s_w = \frac{w' - w}{|z' - z|}, \tag{3.14}$$

where, in order to simplify the notation, it has been assumed that, for any arbitrary function $f(z)$:

$$f' := f(z'). \tag{3.15}$$

The internal virtual work for a peridynamic beam undergoing axial stretching, bending and shear can be expressed as follows (Ref. [134, 156]):

$$\delta W_{int} = \frac{1}{2}\int_0^L \int_{H_z} \left[\mathcal{Z}(z, z')\,\delta s_w + \mathcal{X}(z, z')\,\delta s_\gamma + \mathcal{M}(z, z')\,\delta s_\chi\right] |z' - z|\, dz' dz, \tag{3.16}$$

where $\mathcal{Z}$ and $\mathcal{X}$ are the peridynamic force densities associated with the $\{z, z'\}$ bond in the global z and x directions, respectively (see fig. 3.4). Similarly, $\mathcal{M}$ is the peridynamic bending moment density occurring between the particles z and z'. The notation $\mathcal{Z}(z, z')$ indicates the force density at the point z due to the presence of the $\{z, z'\}$ bond. It is worth stressing that the peridynamics force densities have dimensions of forces per unit length squared; similarly, the peridynamic moment density is expressed as a moment per unit length squared. Based on eq. (3.14), the virtual stretches can be expressed as:

$$\begin{aligned} \delta s_w &= \frac{\delta w' - \delta w}{|z' - z|}, \\ \delta s_\gamma &= \frac{\delta u' - \delta u}{|z' - z|} - \frac{1}{2}(\delta\theta' + \delta\theta)\frac{z' - z}{|z' - z|}, \\ \delta s_\chi &= \frac{\delta\theta' - \delta\theta}{|z' - z|}. \end{aligned} \tag{3.17}$$

It is worth pointing out that the virtual stretches in eq. (3.17) in principle comprise two different sets of virtual fields, which represent displacement/rotations separately evaluated at the locations z and z'. Substituting eq. (3.17) into eq. (3.16) and collecting the virtual displacements yields:

$$\begin{aligned}\delta W_{int} = -\frac{1}{2}\int_0^L \int_{H_z} \Big\{ \mathcal{Z}\left(z,z'\right)\delta w + \\ + \mathcal{X}\left(z,z'\right)\left[\delta u + \frac{1}{2}\left(z'-z\right)\delta\theta\right] + \mathcal{M}\left(z,z'\right)\delta\theta \Big\} dz'dz + \\ + \frac{1}{2}\int_0^L \int_{H_z} \Big\{ \mathcal{Z}\left(z,z'\right)\delta w' + \mathcal{X}\left(z,z'\right)\left[\delta u' + \frac{1}{2}\left(z-z'\right)\delta\theta'\right] + \\ + \mathcal{M}\left(z,z'\right)\delta\theta' \Big\} dz'dz.\end{aligned} \tag{3.18}$$

For equilibrium to be satisfied using bond-based PD, the bond force/moment between z and z' must be equal and opposite to that between z' and z, hence:

$$\mathcal{Z}(z,z') = -\mathcal{Z}(z',z),\ \mathcal{X}(z,z') = -\mathcal{X}(z',z),\ \mathcal{M}(z,z') = -\mathcal{M}(z',z) \tag{3.19}$$

Substituting eq. (3.19) into the expression of the internal virtual work in eq. (3.18), it is immediate to observe that the second integral is equal and opposite to the first one, since the integration variables z and z' can be swapped, one gets:

$$\begin{aligned}\delta W_{int} = -\int_0^L \int_{H_z} \Big\{ \mathcal{Z}\left(z,z'\right)\delta w + \mathcal{X}\left(z,z'\right)\delta u + \\ + \left[\frac{1}{2}\mathcal{X}\left(z,z'\right)\left(z'-z\right) + \mathcal{M}\left(z,z'\right)\right]\delta\theta \Big\} dz'dz.\end{aligned} \tag{3.20}$$

Similarly, the external work performed by the distributed external forces $p(z)$ and $q(z)$ along the Z-pin axis shown in fig. 3.4 is expressed as follows:

$$\delta W_{ext} = \int_0^L \left[\left(p - q\phi\right)\delta w + \left(q + p\phi\right)\delta u\right] dz. \tag{3.21}$$

where $\phi = \partial u/\partial z$ is the slope of the beam at point z.

Constitutive Ansatz

In the linear peridynamic Timoshenko beam theory derived with respect to the undeformed reference configuration [156], the axial $\mathcal{N}$ and shear $\mathcal{T}$ force densities and the bending moment density $\mathcal{M}$ are expressed as linear functions of the associated stretches, i.e. :

$$\begin{aligned} \mathcal{N} &= c_a s_w, \\ \mathcal{T} &= c_s s_\gamma, \\ \mathcal{M} &= c_b s_\chi, \end{aligned} \tag{3.22}$$

The constitutive equations in eq. (3.22) imply that the third of eq. (3.19) is satisfied, but also that:

$$\begin{aligned} \mathcal{N}(z,z') &= -\mathcal{N}(z',z), \\ \mathcal{T}(z,z') &= -\mathcal{T}(z',z). \end{aligned} \tag{3.23}$$

In order to ensure that both the first two eq. (3.19) and eq. (3.23) are simultaneously satisfied, it is here assumed that the axial force density $\mathcal{N}$ in the deformed configuration forms an angle $\bar{\theta} = 1/2\,(\theta + \theta')$ with the global z-axis. Similarly, the shear force density forms an angle $\pi/2 + \bar{\theta}$ with the z-axis (see fig. 3.4). Hence, the average cross-sectional rotation for particles belonging to a bond governs the transformation of the force densities in global coordinates. This ansatz allows writing the transformation equations among the force densities for small rotations as follows:

$$\begin{aligned} \mathcal{Z}(z,z') &= \mathcal{N}(z,z') - \mathcal{T}(z,z')\bar{\theta}, \\ \mathcal{X}(z,z') &= \mathcal{T}(z,z') + \mathcal{N}(z,z')\bar{\theta}, \end{aligned} \tag{3.24}$$

by which the conditions in eq. (3.19) and eq. (3.23) are satisfied. Substituting eq. (3.24) into the expression of the internal virtual work from eq. (3.20) leads to:

$$\begin{aligned} \delta W_{int} = -\int_0^L \int_{H_z} \Big\{ \big[\mathcal{N}(z,z') - \mathcal{T}(z,z')\bar{\theta}\big]\,\delta w \\ + \big[\mathcal{T}(z,z') + \mathcal{N}(z,z')\bar{\theta}\big]\,\delta u + \\ + \left\{ \frac{1}{2}\big[\mathcal{T}(z,z') + \mathcal{N}(z,z')\bar{\theta}\big]\,(z'-z) + \mathcal{M}(z,z') \right\} \delta\theta \Big\}\, dz'dz. \end{aligned} \tag{3.25}$$

Imposing $\delta W_{int} = \delta W_{ext}$ for any arbitrary set of virtual displacement/rotation fields $\{\delta w,\, \delta u,\, \delta\theta\}$ leads to the following set of non-linear peridynamic governing equations:

$$\begin{aligned}
&\int_{H_z} \left[\mathcal{N} - \mathcal{T}\bar{\theta}\right] dz' + p - qu^I = 0,\\
&\int_{H_z} \left[\mathcal{T} + \mathcal{N}\bar{\theta}\right] dz' + q + pu^I = 0,\\
&\int_{H_z} \left\{\mathcal{M} + \frac{1}{2}\left[\mathcal{T} + \mathcal{N}\bar{\theta}\right](z'-z)\right\} dz' = 0.
\end{aligned} \tag{3.26}$$

Hence, substituting the constitutive equations from eq. (3.22) into eq. (3.26) and invoking the d'Alambert's principle for the inertial forces, one gets:

$$\begin{aligned}
\rho A\ddot{w} &= \int_{H_z} c_a s_w dz' - \int_{H_z} c_s s_\gamma \bar{\theta} dz' + p - qu^I,\\
\rho A\ddot{u} &= \int_{H_z} c_s s_\gamma dz' + \int_{H_z} c_a s_w \bar{\theta} dz' + q + pu^I,\\
\rho I\ddot{\theta} &= \int_{H_z} c_b s_\chi dz' + \frac{1}{2}\int_{H_z} \left[c_s s_\gamma + c_a s_w \bar{\theta}\right](z'-z)\, dz'.
\end{aligned} \tag{3.27}$$

Vanishing Horizon Limit

In the limit as the horizon tends to zero the PD governing equation in eq. (3.27) must revert to their classical continuum counterpart in eq. (A.10) (see Appendix A) . Thus the PD equation obtained in eq. (3.27) will be derived in the limit as the horizon tends to zero. The obtained equations will then be compared to there classic counterparts in eq. (A.10) in order to obtain the bond constants c_a, c_s and c_b.

Let r_H denote the radius of the horizon associated with a peridynamic particle belonging to the beam. This radius is here considered as a characteristic constant. In the limit as $r_H \to 0$, the field variables within the horizon of an arbitrary particle can be approximated via a Taylor expansion truncated at the second order. Hence, one has the following approximation

as $r_H \to 0$:

$$\begin{aligned} u' &\approx u + u^I (z' - z) + \tfrac{1}{2} u^{II} (z' - z)^2 + O(z' - z)^3 \\ w' &\approx w + w^I (z' - z) + \tfrac{1}{2} w^{II} (z' - z)^2 + O(z' - z)^3 \\ \theta' &\approx \theta + \theta^I (z' - z) + \tfrac{1}{2} \theta^{II} (z' - z)^2 + O(z' - z)^3 \end{aligned} \tag{3.28}$$

Substituting the Taylor expansion of the displacements (eq. (3.28)) into the stretch definition in eq. (3.14), the following $O(z' - z)$ approximated expressions of the stretches are obtained:

$$\begin{aligned} s_\chi &\approx \theta^I \frac{z' - z}{|z' - z|} + \frac{1}{2} \theta^{II} |z' - z| , \\ s_\gamma &\approx \left(u^I - \theta\right) \frac{z' - z}{|z' - z|} + \frac{1}{2} \left(u^{II} - \theta^I\right) |z' - z| , \\ s_w &\approx w^I \frac{z' - z}{|z' - z|} + \frac{1}{2} w^{II} |z' - z| . \end{aligned} \tag{3.29}$$

For the derivations that follow, it is worth observing that:

$$\int_{H_z} \frac{z' - z}{|z' - z|} dz' = 0, \quad \int_{H_z} |z' - z| \, dz' = r_H^2. \tag{3.30}$$

The calculation of the integrals in eq. (3.27) in the limit $r_H \to 0$ is here carried out considering only the leading terms of order $O(1)$ and $O(z' - z)$ in the integrands. This follows from the fact that, as mentioned above, the stretches have been approximated as $O(z' - z)$ in eq. (3.29). From eq. (3.29) and eq. (3.30) it immediately follows that:

$$\begin{aligned} \int_{H_z} c_b s_\chi dz' &\approx \frac{1}{2} c_b r_H^2 \theta^{II}, \qquad \int_{H_z} c_a s_w dz' \approx \frac{1}{2} c_a r_H^2 w^{II}, \\ \int_{H_z} c_s s_\gamma dz' &\approx \frac{1}{2} c_s r_H^2 \left(u^{II} - \theta^I\right), \\ \frac{1}{2} \int_{H_z} c_s s_\gamma (z' - z) \, dz' &\approx \frac{1}{2} c_s r_H^2 \left(u^I - \theta\right). \end{aligned} \tag{3.31}$$

Moreover, considering the second integral on the right hand side of the first of eq. (3.27), one can write:

$$\int_{H_z} c_s s_\gamma \bar{\theta} dz' \approx$$

$$\approx c_s \int_{H_z} \left[\left(u^I - \theta\right) \frac{z'-z}{|z'-z|} + \frac{1}{2}\left(u^{II} - \theta^I\right)|z'-z| \right] \left[\theta + \frac{1}{2}\theta^I \left(z'-z\right) \right] dz' \tag{3.32}$$

$$\approx \frac{1}{2} c_s \int_{H_z} \left[\left(u^{II} - \theta^I\right)\theta + \theta^I \left(u^I - \theta\right) \right] |z'-z| \, dz'$$
$$= \frac{1}{2} c_s r_H^2 \left[\theta \left(u^I - \theta\right) \right]^I .$$

Developing the second integral on the right hand side of the second of eq. (3.27) yields:

$$\int_{H_z} c_a s_w \bar{\theta} dz' \approx$$

$$\approx c_a \int_{H_z} \left[w^I \frac{z'-z}{|z'-z|} + \frac{1}{2} w^{II} |z'-z| \right] \left[\theta + \frac{1}{2}\theta^I \left(z'-z\right) \right] dz' \tag{3.33}$$

$$\approx \frac{1}{2} c_a \int_{H_z} \left(w^I \theta^I + w^{II} \theta \right) |z'-z| \, dz' = \frac{1}{2} c_a r_H^2 \left(w^I \theta \right)^I .$$

Finally, the last integral that needs to be evaluated appears in the third of eq. (3.27) and it is:

$$\frac{1}{2} \int_{H_z} c_a s_w \bar{\theta} \left(z'-z\right) dz' \approx$$

$$\approx \frac{1}{2} c_a \int_{H_z} \left[w^I \frac{z'-z}{|z'-z|} + \frac{1}{2} w^{II} |z'-z| \right] \left[\theta + \tfrac{1}{2}\theta^I \left(z'-z\right) \right] \left(z'-z\right) dz' \tag{3.34}$$

$$\approx \frac{1}{2} c_a \int_{H_z} w^I \theta \, |z'-z| \, dz' = \frac{1}{2} c_a r_H^2 w^I \theta .$$

Substituting eqs. 3.31-3.34 into the peridynamic equilibrium equations eq. (3.27) leads to the following approximation of the governing PD equation as $r_H \to 0$:

$$\begin{aligned}
\rho A\ddot{w} &= \frac{1}{2}c_a r_H^2 w^{II} - \frac{1}{2}c_s r_H^2 \left[\theta\left(u^I - \theta\right)\right]^I + p - qu^I, \\
\rho A\ddot{u} &= \frac{1}{2}c_s r_H^2 \left(u^{II} - \theta^I\right) + \frac{1}{2}c_a r_H^2 \left(w^I\theta\right)^I + q + pu^I, \\
\rho I\ddot{\theta} &= \frac{1}{2}c_b r_H^2 \theta^{II} + \frac{1}{2}c_s r_H^2 \left(u^I - \theta\right) + \frac{1}{2}c_a r_H^2 w^I\theta.
\end{aligned} \tag{3.35}$$

The peridynamic equations in the vanishing horizon limit in eq. (3.35) must be equal to those for a classical Timoshenko beam given in eq. (A.10). Thus comparing eq. (3.35) and eq. (A.10), the expressions of the peridynamic bond constants are:

$$c_a = \frac{2EA}{r_H^2}, \quad c_s = \frac{2\kappa GA}{r_H^2}, \quad c_b = \frac{2EI}{r_H^2}. \tag{3.36}$$

It is worth noting that the peridynamic bending bond stiffness c_b derived by Diyaroglu et al. (Ref. [156]) is $c_b = \frac{2EI}{r_h^2 A^2} + \frac{1}{4}\frac{kG}{A}$ for a prismatic 3D beam element. This contradicts the value obtained in this derivation as per eq. (3.36). It is believed that the value obtained in this derivation is the correct one. This is supported by a very recent paper by Nguyen et al. (Ref. [157]) where the derived 3D peridynamic bending stiffness is found to be $c_b = \frac{2EI}{Ar_h^2}$ for a 3D prismatic beam, which reduces to the 1D counterpart in eq. (3.36) when multiplied by the cross sectional area A.

The Governing Equations

The governing equation for a Timoshenko beam with small rotations using the peridynamic formulation is obtained by substituting the bond constants in eq. (3.36) into eq. (3.27) :

$$\rho A\ddot{w} = \frac{2EA}{r_H^2}\int_{H_z} s_w dz' - \frac{2\kappa GA}{r_H^2}\int_{H_z} s_\gamma \bar{\theta} dz' + p - qu^I,$$

$$\rho A\ddot{u} = \frac{2\kappa GA}{r_H^2}\int_{H_z} s_\gamma dz' + \frac{2EA}{r_H^2}\int_{H_z} s_w \bar{\theta} dz' + q + pu^I, \tag{3.37}$$

$$\rho I\ddot{\theta} = \frac{2EI}{r_H^2}\int_{H_z} s_\chi dz' + \frac{1}{2}\int_{H_z}\left[\frac{2\kappa GA}{r_H^2}s_\gamma + \frac{2EA}{r_H^2}s_w\bar{\theta}\right](z'-z)\,dz'.$$

3.3.3 Numerical Stability

Analytical solutions of the developed PD equations is limited to very specific cases as discussed in section 3.2. The vast majority of problems, including the ones in this thesis, are solved by employing numerical schemes. The use of numerical schemes introduces truncation errors that must be bounded to obtain convergent results. This motivates the need for the numerical stability analysis conducted in this section.

For simplicity the 1D rod governing equations (see eq. (3.12)) will be examined here. The estimated stable time step based on the analysis conducted here can be multiplied by a safety factor less than 1 to ensure stability in cases of non-linear governing equations such as that in eq. (3.37).

Let the rod be divided in M segments, each having length $\Delta z = L/M$ and let it be assumed that the displacement field $w(z)$ is constant within each of the segments. This leads to a "meshfree" discretization of the rod (Ref. [134]), whereby a peridynamic particle is located at the centre of each segment. Hence, the position of the i-th peridynamic particle is $z_i = \Delta z\left(i - \frac{1}{2}\right)$, $i =$ 1, 2, ..., M. The integro-differential equation in (3.12) can therefore be discretised as follows:

$$\rho A\ddot{w}_i + b_w\dot{w}_i = I_i + p_i, \tag{3.38}$$

where $\ddot{w}_i = \ddot{w}(z_i)$, $p_i = p(z_i)$. The integral on the rights hand side of eq. (3.12) is approximated via a Riemann sum [134], i.e.

$$I_i = \frac{2EA\Delta z}{r_h^2}\sum_{\substack{j\neq i\\ j=i_1}}^{i_N}\frac{w_j - w_i}{|z_j - z_i|}, \tag{3.39}$$

where i_1, i_2, ..., i_N are the N particles in the horizon H_{z_i} of the i-th particle.

Introducing an explicit discretisation with respect to time via a second-order centred finite difference scheme [134, 156], eq. (3.38) leads to:

$$\rho A \frac{w_i^{(n+1)} - 2w_i^{(n)} + w_i^{(n-1)}}{\Delta t^2} + b_w \frac{w_i^{(n+1)} - w_i^{(n-1)}}{2\Delta t} = I_i^{(n)} + p_i^{(n)}, \tag{3.40}$$

where Δt is the time step and the superscript (n) denotes the n-th time instant. Substituting eq. (3.39) into eq. (3.40) and solving with respect to $w_i^{(n+1)}$ yields the following time-marching solution:

$$w_i^{(n+1)} = \frac{4w_i^{(n)} - (2 - \chi_w \Delta t)\, w_i^{(n-1)} + 4\left(\frac{\Delta t}{t_h}\right)^2 J_i^{(n)} + 2\Pi_i^{(n)}}{2 + \chi_w \Delta t} \tag{3.41}$$

where:

$$\begin{gathered} \chi_w := \frac{b_w}{\rho A}, \quad t_h := r_h \sqrt{\tfrac{\rho}{E}}, \\ J_i^{(n)} := \Delta z \sum_{\substack{j \neq i \\ j=i_1}}^{i_N} \frac{w_j^{(n)} - w_i^{(n)}}{|z_j - z_i|}, \quad \Pi_i^{(n)} := \frac{p_i^{(n)} \Delta t^2}{\rho A}. \end{gathered} \tag{3.42}$$

Considering the time-marching scheme from eq. (3.41), let the round-off error be defined as $e_i^{(n)} = \hat{w}_i^{(n)} - w_i^{(n)}$, where $\hat{w}_i^{(n)}$ is the exact numerical solution, while $w_i^{(n)}$ is the actual displacement field obtained due to the presence of truncation errors. Let it be assumed that the damping coefficient in eq. (3.41) is zero, i.e. $\chi_w = 0$, and that the external applied force is zero i.e. $p(z) = 0$. Expressing the actual numerical solution as $w_i^{(n)} = \hat{w}_i^{(n)} - e_i^{(n)}$ and substituting the latter into eq. (3.41) lead to the following error-evolution equation:

$$e_i^{(n+1)} = 2e_i^{(n)} - e_i^{(n-1)} + \left(\frac{\Delta t}{t_h}\right)^2 \left[2\Delta z \sum_{\substack{k \neq i \\ k=i_1}}^{i_N} \frac{e_k^{(n)} - e_i^{(n)}}{|z_k - z_i|} \right]. \tag{3.43}$$

where advantage has been taken of the fact that $\hat{w}_i^{(n)}$ exactly satisfies the algebraic equation representing the numerical scheme. Following Von Neumann's approach to stability analysis [134, 135], the error due to truncation can be expressed in the general form

$$e_i^{(n)} = \zeta^{n\Delta t} e^{jk_m i \Delta z}, \tag{3.44}$$

where ζ is in general a complex number, while k_m is a real wave-number; j denotes the complex unit number, i.e. $j = \sqrt{-1}$. For the sake of this analysis, let us assume that the peridynamic particles are numbered in order with an increasing z; the i-th peridynamic particle has in general $N + 1$ particles in its horizon, including itself. The indexes of these particles will be $i - (N-1)/2$, ..., $i - 1$, i, $i + 1$, ..., $i + (N-1)/2$. Substituting eq. (3.44) into eq. (3.43) and considering the reordering of the particles described above yield:

$$\zeta^{\Delta t} = 2 - \zeta^{-\Delta t} + 2\left(\frac{\Delta t}{t_h}\right)^2 \sum_{\substack{r \neq 0 \\ r=-(N-1)/2}}^{(N-1)/2} \frac{e^{jk_m r\Delta z} - 1}{|r|}. \tag{3.45}$$

Euler's formula established the relation between complex exponentials and the sine and cosine functions as: $e^{jx} = cosx + jsinx$. For an even (i.e. symmetric) function the sine component of Euler's formula can be dropped (since the sine function is odd). Therefore, noting the symmetry of the terms that appear in the series on the right hand side, eq. (3.45) can be equivalently expressed in the following form:

$$\zeta^{\Delta t} = 2 - \zeta^{-\Delta t} - 4\left(\frac{\Delta t}{t_h}\right)^2 \sum_{r=1}^{(N-1)/2} \frac{1 - \cos(\kappa_m r)}{r}, \tag{3.46}$$

where $\kappa_m = k_m \Delta z$. Let us define:

$$S_m := \sum_{r=1}^{(N-1)/2} \frac{1 - \cos(\kappa_m r)}{r} \tag{3.47}$$

One can immediately observe that, by virtue of the last definition:

$$S_m \leq 2 \sum_{r=1}^{(N-1)/2} \frac{1}{r} = 2H_{(N-1)/2} \tag{3.48}$$

where $H_{(N-1)/2}$ denotes the $(N-1)/2$-th harmonic number. The n-th harmonic number is define as:

$$H_n = 1 + \frac{1}{2} + \frac{1}{3} + ... + \frac{1}{n} = \sum_{r=1}^{r=n} \frac{1}{r} \tag{3.49}$$

Rearranging eq. (3.46)) leads to the following quadratic algebraic equation in $\zeta^{\Delta t}$:

$$\zeta^{2\Delta t} - 2\left[1 - 2\left(\frac{\Delta t}{t_h}\right)^2 S_m\right]\zeta^{\Delta t} + 1 = 0, \tag{3.50}$$

The above equation can be solved for $\zeta^{\Delta t}$ using the quadratic formula resulting in:

$$\zeta^{\Delta t} = 1 - 2\left(\frac{\Delta t}{t_h}\right)^2 S_m \pm \sqrt{\left[1 - 2\left(\frac{\Delta t}{t_h}\right)^2 S_m\right]^2 - 1} \tag{3.51}$$

The stability of the numerical scheme in eq. (3.41) is guaranteed by ensuring that the truncation error remains bounded. The truncation error remains bounded if the amplitude term in eq. (3.44) does not grow as time progresses i.e. by imposing $\left|\zeta^{\Delta t}\right| \leq 1$, which is guaranteed by:

$$\left|1 - 2\left(\frac{\Delta t}{t_h}\right)^2 S_m\right| \leq 1, \tag{3.52}$$

that is satisfied for:

$$\left(\frac{\Delta t}{t_h}\right)^2 S_m \leq 1. \tag{3.53}$$

Hence, for the time step one obtains:

$$\Delta t \leq \frac{t_h}{\sqrt{S_m}}. \tag{3.54}$$

It is interesting to note that t_h in the above equation represents the time taken by an elastic wave to travel across half the horizon of a particle. Thus the stable time step size is limited by the horizon size rather than the grid spacing (Δz) as is the case in classical continuum formulations.

3.4 Peridynamic Numerical Solution Considerations

The solution of the PD governing equation is constructed using numerical techniques for time and spatial integration. The integro-differential format

in PD formulation give rise to specific issues that require special treatment in the solution procedure. These issues and the treatments used are discussed in this section.

3.4.1 Initial and Boundary Condition Application

Collocation method is used to perform spatial integration where the region of interest is divided into domains. Each domain is assigned a material (collocation) point with a specific volume (see fig. 3.5). This approach is mesh free in the sense that there are no geometrical connections between the material points.

The PD equations provide the acceleration of the material point. Integrating the acceleration is necessary to obtain velocity and consequently displacement. Thus it is necessary to specify initial displacement and velocity. This can be easily done by specifying the initial displacement and velocity for all material points.

On the other hand, the use of spatial integration in PD formulation as opposed to spatial derivative in classical continuum mechanics means that the application of a boundary condition (B.C.) is not generally required to solve the PD equations of motion. Nonetheless, if imposing B.C. is necessary then this can be applied in a "fictitious material layer" at the boundary. Numerical experiments conducted by Macek et al. (Ref. [158]) suggests that the fictitious material layer should be equal to the horizon radius , r_h, to adequately ensure that the prescribed boundary condition is reflected on the actual material region (See fig. 3.5).

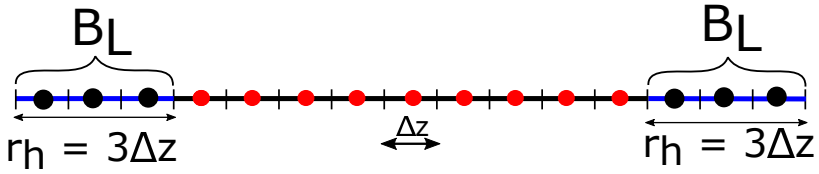


Figure 3.5: Domain of interest is discretised into equal segments of length Δz with red material (collocation) points in the middle of each segment. Fictitious boundary layer (B_L) can be used to apply boundary condition. B_L has a length of r_h

3.4.2 Volume Correction

For a given material point (z_i), the governing PD equation includes integration over the volume of material points (z_j) in its horizon. Numerically, the integration involves summation over the volume of material points in the horizon of z_i. However, the volume of material point z_j is not necessarily embedded in its entirety in the horizon of material point z_i. This is particularly the case towards the edge of the horizon where the volume of material point z_j is truncated. This issue becomes clear by the illustration presented in fig. 3.6 where it is evident that the particle at the horizon edge only has half of the volume embedded in the horizon.

Thus instead of using the entire volume of each particle in the horizon of z_i, a volume correction can be applied to improve the approximation (Ref. [135]). The full material volume is considered for material points z_j where $\delta_{ij} = |z_j - z_i| \leq r_h - r$ in which $r = \Delta z/2$. However, for material points z_j where $r_h - r \leq \delta_{ij} \leq r_h$, a volume correction factor $v_{c(j)} = (r_h + r - \delta_{ij}) / (2r)$ is introduced. Hence, for a uniform grid discretization the volume correction factor varies between 1 and 1/2 depending on the location of material point z_j relative to the horizon boundary. Consequently, the discretized solution of the general PD equation presented in eq. (3.1) is given by eq. (3.55), i.e. the volume correction factor $v_{c(j)}$ multiply the volume of each particle in the horizon to ensure that the appropriate volume is used during integration.

$$\rho(\mathbf{z_i})\ddot{\mathbf{u}} = \sum_{H_z} \left(\mathbf{t}_{\mathbf{z_i},\mathbf{z_j}} - \mathbf{t}_{\mathbf{z_j},\mathbf{z_i}}\right) v_{c(j)} V_j + \mathbf{b}(\mathbf{z_i}, t) \tag{3.55}$$

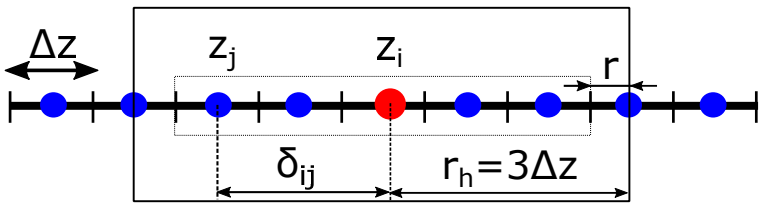


Figure 3.6: Illustration for volume correction procedure.

3.4.3 Surface Correction

The peridynamic bond constants c_a, c_b and c_s in section 3.3.2 were derived based on a material point with a fully embedded horizon within the domain of interest. Nonetheless, a material point close to the surface might not have a full horizon as shown in Figure 3.7. Therefore, a correction is needed for a material point that is close to a free surface. This correction will be referred to as the surface correction factor (SCF).

To obtain the SCF, the PD strain energy density (ϵ_{PD}) at each material point is computed numerically for a simple loading condition. This is then compared to the strain energy density ($\epsilon_{classical}$) obtained using the classical continuum method. Thus, the SCF for a material point at z_i is defined by eq. (3.56). An example of a simple loading condition is a bar subject to axial extension (Ref. [135]).

$$SCF(z_i) = \frac{\epsilon_{classical}(z_i)}{\epsilon_{PD}(z_i)} \tag{3.56}$$

3.4.4 Adaptive Dynamic Relaxation

The PD equation of motion is inherently formulated for a dynamic problem. Although it is possible to use explicit time integration to solve for a quasi-static problem, the computational cost for such an approach is prohibitively expensive. In order to solve the PD equation for a quasi-static problem, Adaptive Dynamic Relaxation (ADR) is used (Ref. [159]).

ADR is based on the fact that the static solution is the steady state component of the transient response. Artificial damping is used to guide the dynamic solution to the steady state response as quickly as possible. The

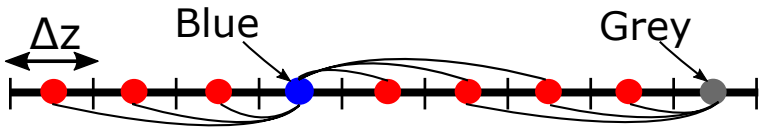


Figure 3.7: Illustration of surface effect. The blue particle has full horizon interactions while the grey particle at the edge has half horizon interactions. In this case the horizon has a radius $r_h = 3\Delta z$.

optimal damping coefficient is calculated at each time step using the ADR scheme introduced by Underwood in Ref. [159].

ADR is used in this thesis to solve quasi-static problems. The solution procedure is based on the work conducted by Kilic et al (Ref. [160]). For details of the mathematical procedure the reader is advised to consult the work in Ref. [160].

3.5 Peridynamic Validation

The developed rod and beam peridynamic equations of motion are validated in this section. The validation provides confidence that the developed formulation is correct before being used later to model the Z-pin bridging performance. For this purpose, simple structures subjected to quasi-static loading will be solved using the developed peridynamic equations. The obtained solution is then compared against well established analytical results as a mean of validating the developed equations.

3.5.1 Bar Under Uniformly Distributed Tensile Load

Consider a prismatic bar subjected to uniformly distributed axial load $f = 200N/m$ as shown in fig. 3.8. The bar is built in at one end (i.e. cantilevered bar), has a length $L = 1m$, a square cross section of $1mm \times 1mm$ and made from steel with a Young's modulus of $200GPa$.

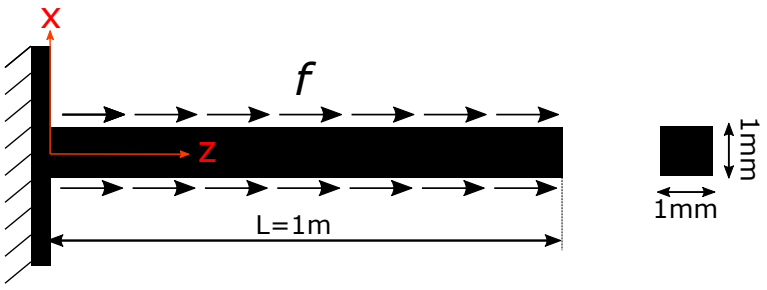


Figure 3.8: Cantilevered bar subject to uniformly distributed axial load.

An analytic solution to the above problem can be obtained using the classical continuum formulation as:

$$w(z) = \int_0^z \frac{P(z)}{EA} dz \tag{3.57}$$

where, $w(z)$ and $P(z)$ are the bar extension and force acting on the cross section at point z respectively. E and A are the Young's modulus and cross sectional area respectively. For a uniformly distibuted load f, the force acting on the cross section is $P(z) = fz$. Thus the extension w at any location along the beam is obtained as:

$$w(z) = \frac{fz^2}{2EA} \tag{3.58}$$

The developed peridynamic rod formulation in eq. (3.12) is solved numerically to obtain the bar extension. The bar is discretized uniformly into 200 particles (i.e. $\Delta z = 5 * 10^{-3} m$). The horizon radius used is $r_h = 3\Delta z$. A boundary layer equal to the horizon radius (i.e. $3\Delta z$) is added to the built in end to allow for boundary condition application as discussed in section 3.4.1 (see fig. 3.5). The displacement of the particles in the boundary layer is set to zero as the boundary condition. The generic i-th segment is a peridynamic particle that interacts with a further N_h particles with indices $i_1, i_2, ..., i_{N_h}$. Thus approximating the integral in eq. (3.12) as a Riemann sum (Ref. [134, 156]) and applying volume correction factor (v_c), the discretized governing equation becomes:

$$\rho A \left(\ddot{w}_i + \chi_w \dot{w}_i\right) = \frac{2EA}{r_h^2} \sum_{j=i_1}^{i_{N_h}} \left[\frac{w_j - w_i}{|z_j - z_i|} v_{c(j)} \Delta z\right] + b(z_i) \tag{3.59}$$

Where, χ_w is the mass-proportional viscous damping used in the ADR procedure (Ref. [160]) to obtain the static solution. The convergence to the static solution using ADR is guaranteed by ensuring that the ratio of the kinetic to elastic energy of the system is less than a certain tolerance (1E-8 in this case).

Since, the deformed shape takes the form $w(z) = \beta z^2$ (see eq. (3.58)), then the appropriate peridynamic body force ($b(z_i)$) is given by (Ref. [161]):

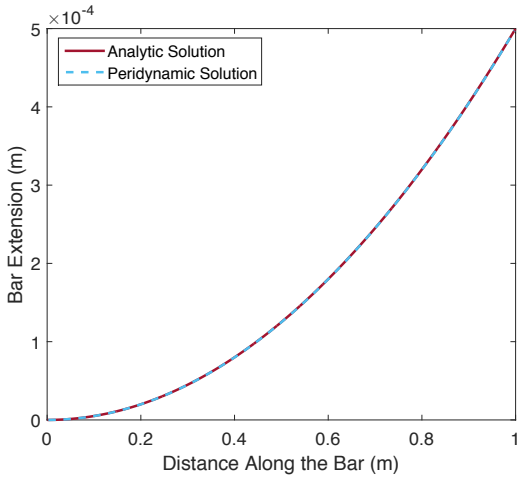


Figure 3.9: Comparison of peridynamic prediction and analytical results for a prismatic bar under uniformly distributed axial load.

$$b(z_i) = \begin{cases} -f & z_i \in (0, L - r_h] \\ f\left(4z_i r_h - r_h^2 + 3z_i^2 - 2z_i L - L^2\right) & z_i \in (L - r_h, L] \end{cases} \tag{3.60}$$

The body load within a distance of r_h from the edge takes a slightly different form to that within the body of the bar due to surface effect as discussed earlier.

Based on the above, the obtained peridynamic and analytical results are seen to be in excellent agreement as shown in fig. 3.9.

3.5.2 Cantilever Beam Under Transverse Loading

Consider a prismatic cantilever beam subjected to tip load $F = 5000N$ as shown in fig. 3.10. The beam has a length $L = 1m$ and a square cross section of $0.1m \times 0.1m$. The beam material is steel such that Young's (E) and shear (G) modulus has a value of $200GPa$ and $80GPa$ respectively. The reference axis is placed at the built in end with the beam lying in the $z - x$ reference (see fig. 3.10).

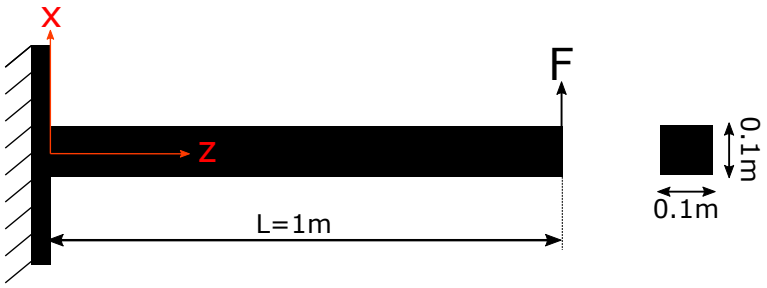


Figure 3.10: Cantilever beam subject to tip load of P.

The deflection (u) and cross section rotation (θ) for the above problem is analytically obtained by solving the classical Timoshenko beam equations (Ref. [162]) as:

$$\begin{aligned} \theta(z) = &\quad \tfrac{F}{2EI}\left(2Lz - z^2\right) \\ u(z) = &\quad \tfrac{Fz}{\kappa GA} - \tfrac{F(L-z)}{6EI}\left(2L^2 + 2Lz - z^2\right) + \tfrac{FL^3}{3EI} \end{aligned} \tag{3.61}$$

Where, A and I are the cross sectional area and moment of inertia respectively. κ is the Timoshenko shear correction factor which is 5/6 for a rectangular cross section.

The peridynamic solution for the same problem is obtained by numerically solving eq. (3.37). For this purpose, the same spatial discretization, horizon radius and boundary condition application as that in section 3.5.1 is used. Thus approximating the integral in eq. (3.37) as a Riemann sum (Ref. [134, 156]), and applying volume (v_c) and surface (SCF) correction factors, the discretized governing equation (eq. (3.37)) becomes:

$$\begin{aligned} \rho A\left(\ddot{w}_i + \chi_w \dot{w}_i\right) &= I_{ij}^{(1)} - q_i \phi_i, \\ \rho A\left(\ddot{u}_i + \chi_u \dot{u}_i\right) &= I_{ij}^{(2)} + q_i, \\ \rho I\left(\ddot{\theta}_i + \chi_\theta \dot{\theta}_i\right) &= I_{ij}^{(3)}, \end{aligned} \tag{3.62}$$

Where the I_{ij}^m entries are given in AppendixB; χ_w, χ_u and χ_θ are the mass-proportional viscous damping coefficients introduced to accelerate convergence towards the quasi-static solution as proposed by Kilic in Ref. [160].

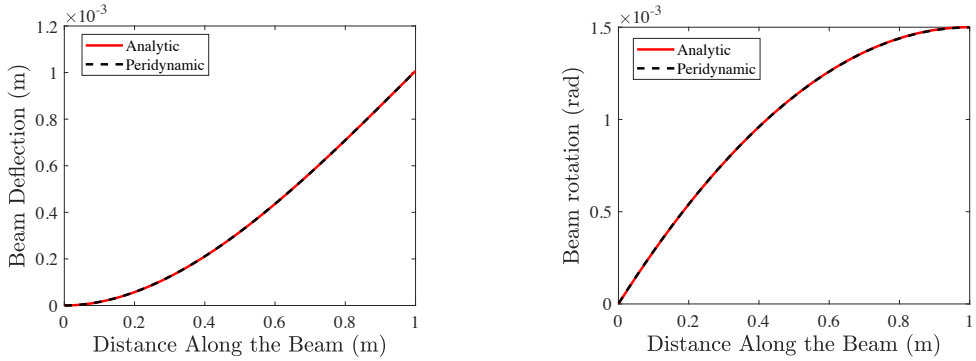


Figure 3.11: Comparison of peridynamic prediction and analytic results for a tip loaded beam. (a) Deflection and (b) Cross section rotation along the beam.

Finally, in eq. (3.62), $\phi_i = u_i^I$ denotes the slope of the beam axis.

The applied tip load (F) is a point load while the force q_i in eq. (3.62) is a body load with units of N/m. Consequently, the force q_i in eq. (3.62) is zero except for the particle at the tip where $q_{tip} = F/\Delta z$.

Time integration of eq. (3.62) is performed using the ADR technique (Ref. [160]). Convergence to the static solution is guaranteed by ensuring that the ratio of the kinetic to elastic energy of the system is less than a certain tolerance (1E-8 in this case).

Based on the above, the obtained peridynamic and analytical results presented in fig. 3.11 are seen to be in excellent agreement. Consequently, it can be asserted that the derived peridynamic governing equations (eq. (3.37)) are correct.

3.6 Summary

Peridynamic theory is a non-local formulation of the equations of motion. In peridynamic theory a particle at location z interacts with other particles

within a predefined distance known as the horizon. In contrast, classical continuum mechanics (a local theory) assumes that a particle at location z only interacts with other particles in its immediate vicinity.

A review of key advancements in PD theory and its applications is presented in section 3.2. The initial form of PD theory proposed by silling (Ref. [125]) is known as "bond-based" peridynamics. In "bond-based" peridynamics the Poisson's ratio of the material is limited to 0.25. To overcome this limitation, Silling et al. (Ref. [126]) developed the "state-based" peridynamics. Both forms of PD theory, "bond-based" and "state-based" has been used in various applications. A particularly favourable application is in prediction of damage initiation and propagation. This is the case, because PD theory has the damage model inherent to the mathematical formulation. Consequently, crack initiation and propagation can be arbitrary instead of following a predefined path.

The peridynamic rod and beam formulation are developed in this chapter. The developed beam formulation is based on Timoshenko beam and assumes that the cross sectional rotation are small but not negligible. Consequently, the proposed model allows for coupling between axial and transverse deformation. Hence, it was referred to as "non-linear Timoshenko beam".

The developed peridynamic equations are mostly solved using numerical schemes. Certain considerations need to be taken into account when solving the peridynamic equation numerically. This include adding a fictitious boundary layer equal to the horizon radius to apply boundary conditions. When performing spatial integration appropriate volume and surface corrections need to be applied. Lastly, the PD equations are inherently formulated for dynamic problems. However, adaptive dynamic relaxation procedure can be applied on PD equations to solve static problems. ADR assumes that the static solution of PD equation is the steady-state solution of the dynamic problem. Consequently, optimal damping is applied at each time step to reach the steady-state solution in the shortest possible time.

The developed PD equations have been validated by comparing the numerically obtained peridynamic results against well established analytical solution of simple structures under quasi-static loading.

Chapter 4

Experimental Results

4.1 Introduction

The development of a peridynamics-based reduced-order model to simulate Z-pin bridging performance requires the calibration of characteristic parameters from experimental data. Furthermore, the parameter calibration must be tested to validate the prediction capabilities of the model developed. This validation process requires comparison of the model response to experimental data, which are independent of those data used in the calibration process. Consequently, obtaining a set of experimental data that characterises the bridging response of Z-pins is an essential step towards achieving the aim of creating a reduced order model.

A reliable set of experiments characterising the bridging response of Z-pins at loading rates ranging from quasi-static conditions to pull-out speeds of 12m/s exist in the literature. These tests were conducted by Dr. Hao Cui at Oxford university as part of the DYNAPIN project, which the author was part of. The outcomes of these experimental testing have been published in Ref. [12, 13]. These experimental results are employed in this thesis to calibrate and validate the reduced-order model describing the rate-dependent single Z-pin behaviour.

The raw experimental data obtained from Ref. [12, 13] will be used to produce the post-processed results presented in this chapter. This will allow the reader to be familiar with the experimental data that are used in

the subsequent chapters. In addition, some additional results including Scan Electron Microscopy (SEM) images will be presented here for the first time to provide an explanation of the observed Z-pin response.

In this chapter, the method with which the experiment is conducted will be explained; the experimental set-up and coupon configuration will be illustrated. The results are presented and discussed in a way that highlights important issues underpinning the behaviour of the Z-pinned coupons. The key features of the experimental results will prove to be instrumental in developing an appropriate reduced-order model.

4.2 The Experiment

4.2.1 Coupon Configuration

The test coupon consists of two composite laminates, separated by a PTFE film and connected together by Z-pins, as shown in fig. 4.1. The PTFE film used at the mid-plane between the two laminates creates an artificial delamination. Hence, the bridging force measured during the experiment is completely due to the Z-pins. The specimen cut from Z-pinned plates measured 10x10mm, with a total thickness of 8mm (see fig. 4.1).

The Z-pin is made of T300/BMI material, while the laminates are made from IM7/8552 prepreg with a quasi-isotropic layup. A quasi-isotropic layup was chosen as it is the most widely used configuration in industrial applications. The bridging response of Z-pins is known to depend on the material and configuration of the embedding laminate (Ref. [10, 163]). The top laminate layup is $[0/45/90/-45]_{4s}$, while the bottom laminate has a $[90/-45/0/45]_{4s}$ stacking sequence. A 90° interface was placed at the mid-plane in order to avoid nesting between plies across the delamination, thus ensuring that any bridging force was due only to the presence of reinforcing Z-pins.

The Z-pins used had a diameter of 0.28mm, so they are relatively small compared to the coupon. This makes the bridging response measurement particularly challenging at high rates using the Split Hopkinson Tension Bar (SHTB) test setup (disucssed in detail in section 4.2.2). To overcome this

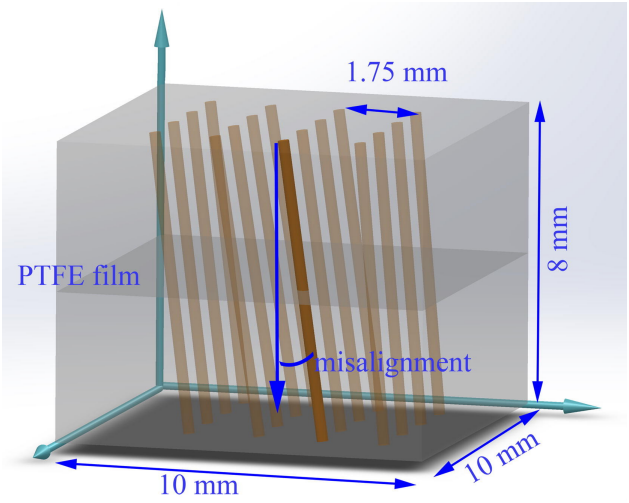


Figure 4.1: Coupon configuration and Z-pin distribution Ref. [12]

difficulty, it was decided to use a 4x4 array of Z-pins corresponding to an areal density of 2%, i.e. a separation distance of 1.75mm between Z-pins.

The Z-pinned coupons were manufactured at the University of Bristol for the Mode I and II experiments, manually inserting the through-thickness rods (TTR). The mixed-mode coupons were manufactured at the National Composite Centre, using the automated direct insertion method patented by Rolls-Royce. In Ref. [12], the authors reported an average misalignment angle of $9°\pm3°$ for the mode I and II coupons. However, for the mixed-mode angle coupons, Ref. [13] reported a negligible misalignment angle. The direct insertion process used for the mixed mode coupons can indeed achieve an almost perfectly orthogonal insertion prior to cure. However, during cure the resin flow will induce some misalignment for the inserted Z-pins. Even if the author in Ref. [13] reported that the vertical offset angle was too small to be measured, it is reasonable to assume there will always be some amount of misalignment for the inserted Z-pins. Following a discussion with Dr. Yusuf Mahadik, who was responsible for the manufacturing of these Z-pinned samples (Ref. [164]), it was established that the Z-pin misalignment angle can vary between 1° and 9° from the vertical depending on the insertion method adopted (i.e. manual or direct), but an average of $0°\pm3°$ provides a reasonable description of the characteristic offset angle seen in directly-

inserted TTR.

4.2.2 Test Set-up

Quasi-static testing was conducted using a ZwicK Roell 250 test machine at a loading rate of 0.01mm/s. The load cell was used to measure the bridging force response. However, when the samples fail abruptly due to the rupture of the Z-pins, particularly in mode II and at high mode-mixities, the load cell acquisition rate is not sufficient to capture the falling trend of the force versus displacement response. Thus, a low impedance 0.9m long aluminium tube was attached between the load cell and the sample tested (see fig. 4.2a). This arrangement ensured that the full progressive drop of the bridging force could be measured before the reflected wave from the load cell end had reached the strain gauge mounted on the tube.

Dynamic test were conducted using a Split Hopkinson Tension Bar (SHTB) system, as shown in fig. 4.2b. The striker is projected at high speed, up to 12m/s, impacting the loading bar and generating a stress pulse with duration of 1ms. This allows the loading of the specimen to failure with a single pulse. For a detailed description of the SHTB test method, the reader can consult Ref. [165].

High speed cameras were used to monitor the failure process of the coupon. The specimen surface was painted with black speckles on a white background, enabling digital image correlation (DIC) to be used to measure the displacement. The use of DIC facilitate obtaining the opening and shear displacement at the delamination interface. However, only the opening and sliding displacements were measured for the mode I and II tests, respectively.

At a quasi-static loading rate, the high speed camera recorded deformation with a sampling rate of 20,000 frames per second (FPS). In the dynamic loading rate conditions, the high speed camera recorded deformation at a frame rate of 100,000 to 500,000 FPS, depending on the duration of the failure event.

To apply the appropriate mixed-mode load to the Z-pinned specimens, aluminium fixtures were designed as shown in fig. 4.3. A brass sleeve was used to constrain the opening displacement in mode II and mixed-mode load-

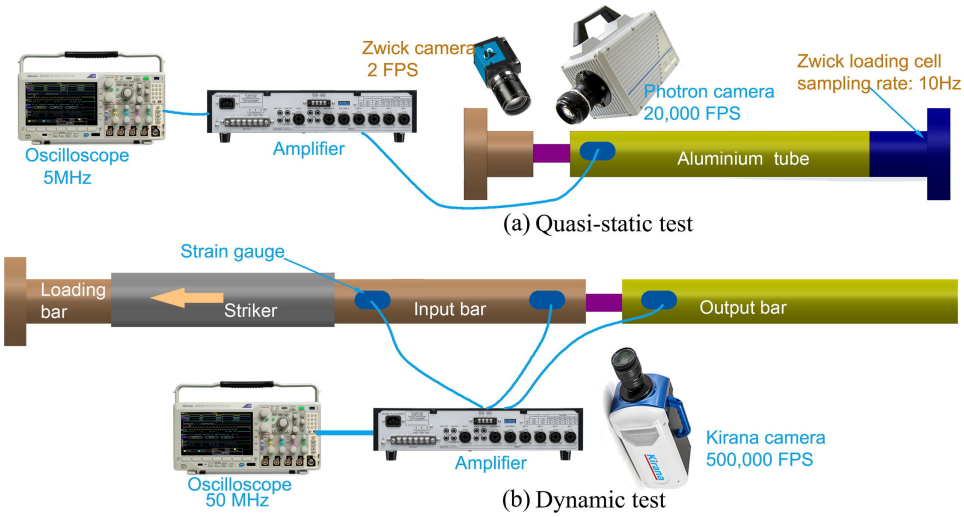


Figure 4.2: Test setup configuration at (a) quasi-static and (b)dynamic loading rate. Ref. [13]

ing. For the mixed-mode tests, the fixture angle β was varied from 15° to 75°, in increments of 15°, in order to achieve a nominal mode-mixity range of 0.259 to 0.966.

4.2.3 Inertia Effects

The sudden acceleration of the samples to the desired test speed in short time makes it very challenging to achieve equilibrium in dynamic tests. Consequently inertial forces arising from the acceleration of the sample and the aluminium fixture would contribute to the measured apparent bridging force. Thus there is a need to correct the inertia effect to obtain the bridging response purely due to the action of the Z-pins.

A finite element study was conducted in Ref. [12] to factor out the influence of inertia from the experimental results. The entire SHTB setup was modelled. The axial strain in an element positioned 200mm from the end of the output bar was used to calculate the force transmitted (F_m) by the specimen, which is equal to that measured in experiment. The acceleration of the fixture was obtained from the simulation. Considering the aluminium

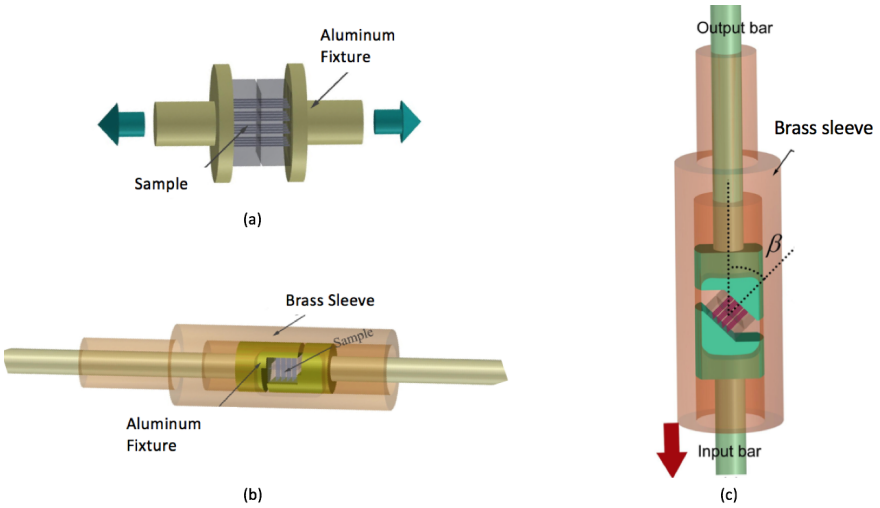


Figure 4.3: Fixture used in (a) Mode I, (b) Mode II and (c) Mixed Mode Loading. Ref. [12, 13]

fixture and the specimen as concentrated masses, the inertia force (F_k) can be calculated by multiplying the acceleration by the total mass. Having both the measured force and the inertia force, the corrected force can be obtained by adding the two associated terms, as shown in eq. (4.1).

$$F = F_m + F_k \tag{4.1}$$

The results presented in Ref. [12] demonstrate that applying the inertia effect correction to the measured force on the output bar can indeed recover the input signal to a high degree of accuracy. Thus it can be concluded that the proposed method for correcting the inertia effect is robust.

During the experiment, images of the specimen were obtained via high speed cameras. DIC was used to obtain the displacement, velocity and, consequently, the acceleration of the specimen and the fixture. Knowing the mass of the specimen and the fixture (6.5g) and the acceleration, the inertia force is calculated. Thus, where appropriate, inertia effects were corrected for in the experimental results based on eq. (4.1). The application of inertia effect correction is further discussed in the results section (section 4.3).

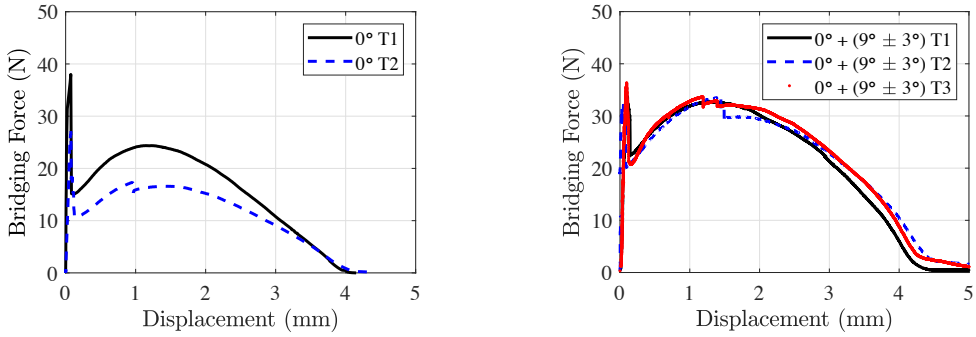
4.3 Results and Discussion

4.3.1 Mode I

The quasi-static and dynamic response of the Z-pin array subject to Mode I loading is presented in figs. 4.4 and 4.5 respectively.

Mode I loading shows the same characteristic response under both quasi-static and dynamic conditions. An initial elastic response of the bonded Z-pin corresponds to the initial peak bridging force observed. As the loading progresses, the Z-pin de-bonds from the surrounding laminate, thus causing the observed drop of the bridging force. Then the Z-pin starts to slide out of the laminate, causing the bridging force to increase up to a second peak followed by progressive decrease to zero. This pull out response indicates that the sliding friction per unit length is increasing, but there comes a point where the reduction in embedded Z-pin length (as pull-out progress) outweighs the increase in frictional force; hence the reduction in bridging response down to zero at complete pull-out.

The increase in frictional force per unit length can be explained by the fact that, as the Z-pin is pulled out, shear cusps are formed, causing debris to build up along the Z-pin pull-out path. In addition, a study presented in Ref. [166] demonstrated that Z-pins do not have a regular cross section along



(a) Mode I (0° misalignment)

(b) Mode I (9° misalignment)

Figure 4.4: The quasi-static bridging response of Z-pins subject Mode I loading. Data adapted from [12].

the length, i.e. the Z-pin does not have a perfect cylindrical shape. This causes a local enhancement contact forces that promote friction. The aforementioned study also found that the Z-pins had a twist angle of 52°, which contributed to the different cross sectional shapes from the bottom to the top of the TTR. Such large twist angle was likely adopted to improve consolidation during the pultrusion process that is usually employed to manufacture the continuous small-diameter CFRP rods from which Z-pin are cut. The Z-pins characterised in the experimental campaign summarised here were also manufactured via pultrusion, but no information is actually available regarding the eventual presence of a twist angle. Microscope observations of the TTR seem to suggest that a small amount of twist, in the order of few degrees, is indeed present, but it is impossible to draw a definitive conclusion observing Z-pins less than 10mm long. The twist could in principle contribute to the observed growth of frictional force during pull-out, by making the lateral surface rougher and also forcing the Z-pin to rotate while being pulled-out. However, the SEM images do not provide a conclusive evidence of such a mechanism.

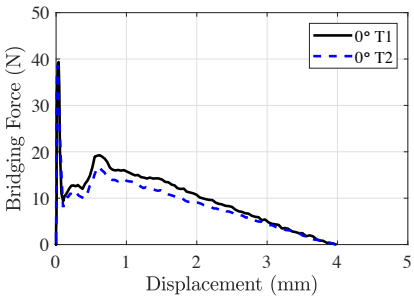
A clear rate effect on the Z-pin bridging response can be appreciated in figs. 4.4 and 4.5. The main features of this rate effect are summarised in the remarks that follow:

1. The peak force achieved during the pull-out stage decreases as the loading rate is increased from quasi-static conditions to 12m/s.

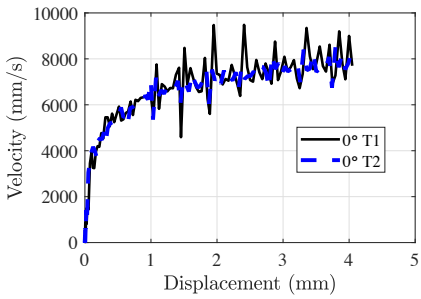
2. The pull-out response following the force peak is increasingly linear as the loading rate is increased; in quasi-static conditions, the amount of non-linearity is significant.

3. The energy dissipated during the pull-out process, defined as the area under the force-displacement graph, decreases with the loading rate.

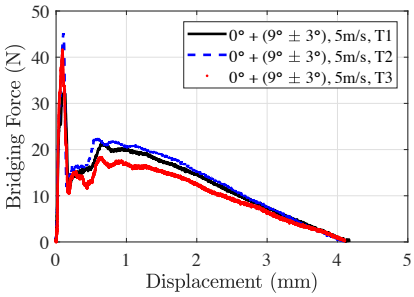
The observations above involve effects that are directly related to the behaviour of the Z-pin/laminate interface. All the tests conducted in mode I conditions ended with the complete Z-pin pull-out. Therefore, the differences observed in terms of force versus displacement trends must arise from the interface frictional response during the pull-out stage, which depends primarily on the loading rate.



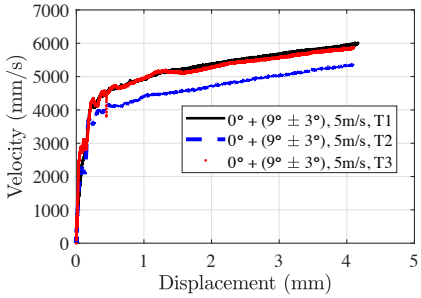
(a) Mode I (0° misalignment)



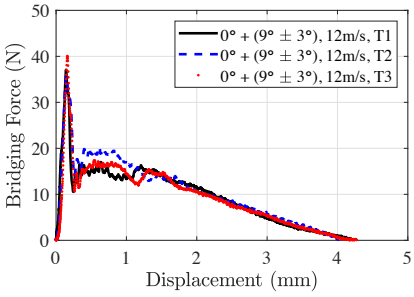
(b) Velocity profile for (a)



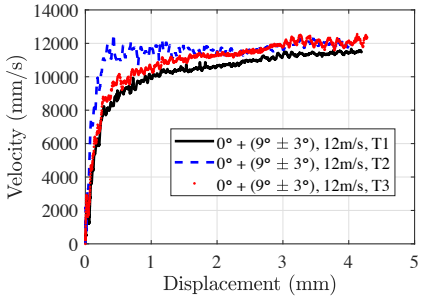
(c) Mode I (9° misalignment)



(d) Velocity profile for (c)



(e) Mode I (9° misalignment)



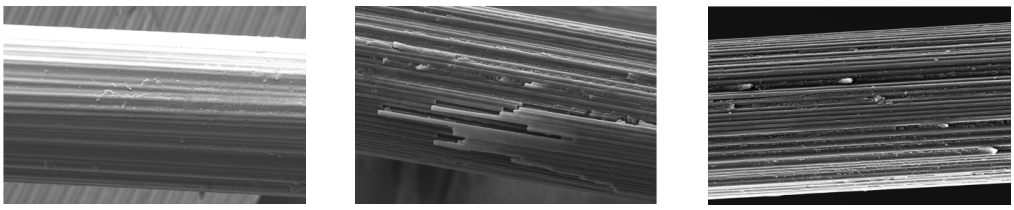
(f) Velocity profile for (e)

Figure 4.5: The bridging response and corresponding velocity profile in Mode I loading subject to dynamic rate. Data adapted from [12].

As can be seen in fig. 4.6, the pristine Z-pin has a smooth surface due to the resin being uniformly present over the whole surface (see fig. 4.6a). However, the surface of a Z-pin that has been pulled-out (both under quasi-

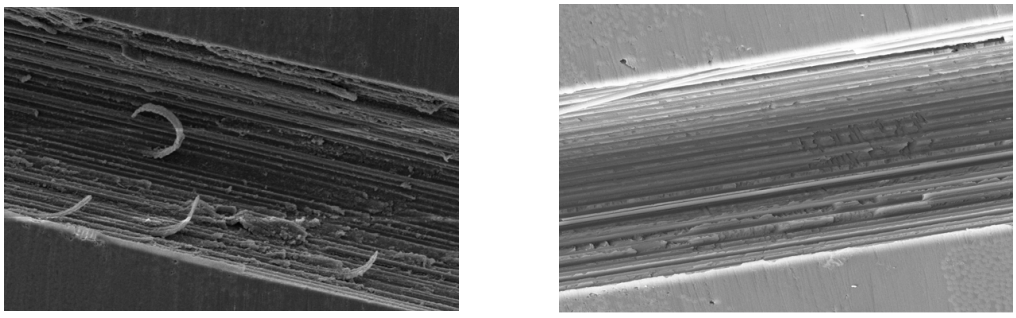
static or dynamic loading) has a rougher appearance, since individual fibres become visible. This is caused by the removal of the resin due to friction as the pull out progresses. In the quasi-static case, there is also evidence of surface fibre failure and fibre de-bond from the Z-pin (see figs. 4.6b and 4.6c). Both of these mechanisms contribute to the additional energy dissipated under quasi-static loading when compared to the dynamic regimes.

Furthermore, observing the surface of the hole left by the Z-pin in the laminate after pull out, shown in fig. 4.7, reveals large shear cusps and a significant amount of debris (see fig. 4.7a) at quasi-static loading. On the other hand, the surface of the hole after the high rate testing is relatively smooth



(a) Pristine (b) Quasi-Static (c) High Rate

Figure 4.6: Z-pin surface observed using scan electron microscopy in (a) pristine condition and subject to (b) quasi-static and (c) dynamic loading.Images are courtesy of Dr. Hao Cui.



(a) Quasi-Static (b) High Rate

Figure 4.7: Hole surface observed using scan electron microscopy after Z-pin pull-out at (a) quasi-static and (b) dynamic rates.Images are courtesy of Dr. Hao Cui.

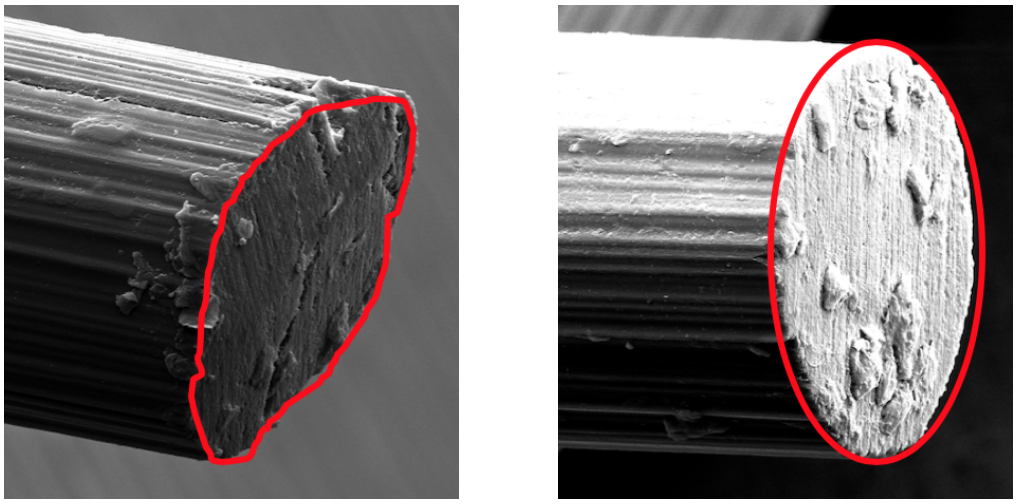


Figure 4.8: Tip cross section profile of two different Z-pins in pristine condition. Images are courtesy of Dr. Hao Cui.

with minimal presence of the shear cusps (see fig. 4.7b). This differences can be attributed to the rate dependence of the matrix mechanical behaviour. At high rate, the resin tend to behave in a brittle manner, while in quasi-static conditions the matrix is much more ductile. This allows for the shear cusps to form and debris to build up, thus explaining the higher energy dissipated under a quasi-static loading regime.

Two different Z-pins in pristine conditions observed via SEM show different cross sectional shapes at the tip (see fig. 4.8). This provides supporting evidence for the second mechanism responsible for frictional force growth as sliding progress discussed earlier, i.e. the local enhancement of contact and frictional forces as the Z-pin slides within the embedding laminate. However, at high loading rates the time scale of pull-out is much smaller than that in the quasi-static case. Thus the interlocking of different cross sectional profiles as the Z-pin slides out of the laminate cannot fully develop under dynamic loading. This provides another reasonable explanation for the reduction of the sliding frictional force at high loading rates.

On the other hand, it is interesting to note that one test contradicts the

observed trend, i.e. the higher the loading rate the lower the bridging force response. In particular this is observed in the T2 test presented in fig. 4.5e. The velocity profile for the T2 test shown in fig. 4.5f is characterised by a higher velocity then in the other two tests, but with a resulting larger bridging action (see fig. 4.5e). There are two possible explanations for this observation. The first is that the author in Ref. [12] argued that a near constant velocity profile is achieved within the first 0.2ms (see fig. 4.9), thus it was decided not to apply inertia correction when presenting the mode I test result. Such a decision would not affect the accuracy of the results, since the energy dissipated prior to pull-out where the Z-pin is accelerating contributes very little to the total work (around 1%). Albeit the acceleration being significantly reduced after 0.2ms to a relatively low value, it never reached zero. Thus the anomaly in the response for the T2 test seen in fig. 4.5e is here attributed to the lack of inertia correction.

Another possible explanation is that the distribution of the misalignment angle within the Z-pin array in the T2 test specimen may be slightly different from the other samples. More Z-pins could have a misalignment angle greater than the average of 9°, thus contributing to the higher bridging response observed. Nonetheless, given that the response is very similar to the other tests in fig. 4.5e once the velocity has stabilised, the effect observed in the T2 test in fig. 4.5e is rather attributed to the lack of inertia correction.

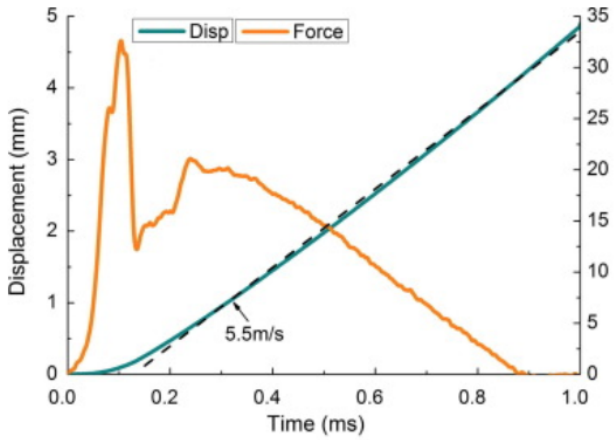


Figure 4.9: A bridging response in dynamic test presented in Ref. [12]

However, the different distribution of misalignment angle within the Z-pin array can be used to explain the difference in the response between T1 and T2 in both quasi-static (see fig. 4.10a) and dynamic (see fig. 4.5a) conditions. In the quasi-static case, the fact that the loading rate is the same is ensured by the cross head movement of the Instron machine, which is sufficiently stiff for the load levels attained during the tests. On the other hand, the velocity plot in fig. 4.5b shows that the pull-out speed is almost identical for the two tests at high rate. Thus the only logical explanation for this difference is that there is a different distribution of the misalignment angle within the array of Z-pins inserted into the two coupons.

Furthermore, the bridging force under mode I loading with 9° misalignment angle is greater than that with a 0° misalignment angle for both quasi-static and dynamic loading cases, as seen in figs. 4.4 and 4.5. This behaviour can be clearly attributed to the difference in the distribution of the misalignment angle within Z-pin arrays for the two batches of coupons. The misalignment angle causes the laminate to exert a punching resistance force against the Z-pins. Consequently this will result in an enhanced friction zone as the Z-pin is pulled out of the laminate. This is a well-known phenomenon, denoted as "snubbing", which was first discussed in Ref. [10]. The snubbing effect was also observed in other tests reported in the literature such as Ref. [83]. Snubbing is a critical factor affecting the Z-pin response in all conditions, apart from the mode I pull out of TTR with perfectly orthogonal insertion.

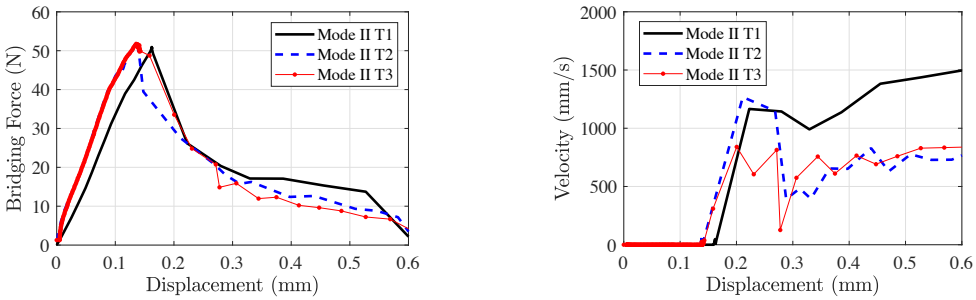
4.3.2 Mode II

The bridging response and the corresponding velocity profile of the Z-pins under Mode II loading for both quasi-static and dynamic loading rates are presented in figs. 4.10 and 4.11 respectively. In both scenarios, there is an initial linear or nearly linear bridging response from the Z-pins. Furthermore, in both cases a peak force of around 50N is reached before a sudden drop to zero occurs as the Z-pin fails. However, the response presented in Ref. [12] beyond the peak force appears to be significantly different from that shown in figs. 4.10 and 4.11.

In the quasi-static mode II test, the Z-pins fail in an unstable fashion,

causing a large acceleration of the sliding motion, which attains a high velocity in a short time period, as detailed in fig. 4.10b. This large acceleration causes inertial effects. Since only a relatively small number of images were taken during the failure process, no accurate acceleration history can be determined. Therefore, the actual bridging force response during the Z-pin failure cannot be obtained, since there are no sufficient data for performing an inertia correction. One could equivalently state that the a quasi-static test always involves a high-rate phase when the TTR experience sudden failure, as it occurs in mode II dominated scenarios.

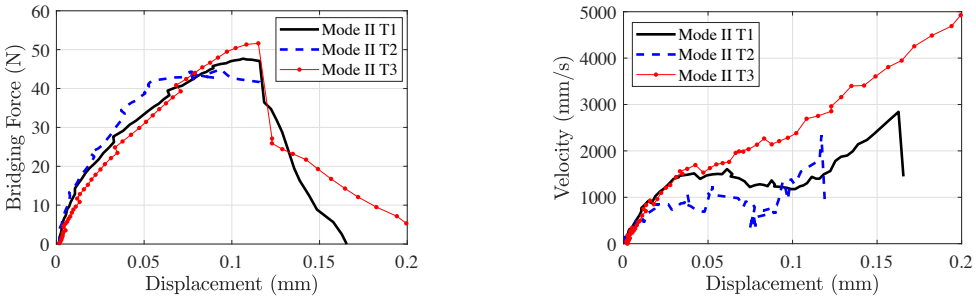
It is worth noting that capturing the decreasing force versus displacement trend during the mode II tests recalled here was done by the high speed cameras that recorded displacements together with the strain gauge attached to the bar used to connect the specimen to the load cell. The observed relatively smooth post-peak response shown in fig. 4.10a is an artefact due to the high speed of the specimen attained as the Z-pin fails. To illustrate this point, fig. 4.12 shows the bridging force as function of displacement and time for a specimen tested under quasi-static mode II loading (coupon T3). The force drops to zero as soon as the Z-pins fail. This confirms that the apparent progressive load drop reported in Ref. [12] is an artificial manifestation of the fact that high speed cameras were used to monitor the specimen failure in shear. It can be safely concluded that the Z-pins subject to Mode II loading fail abruptly past the peak load, regardless of the loading rate.



(a) Bridging Response

(b) Velocity Profile

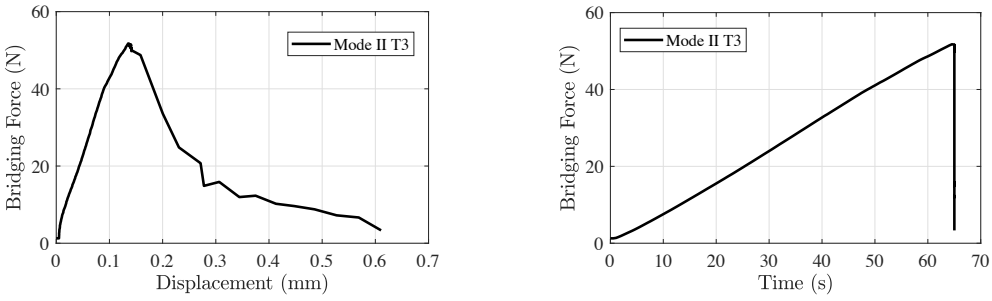
Figure 4.10: Quasi-static mode II response (a) bridging response of Z-pins, (b) velocity profile. Data adapted from Ref. [12].



(a) Bridging Response (b) Velocity Profile

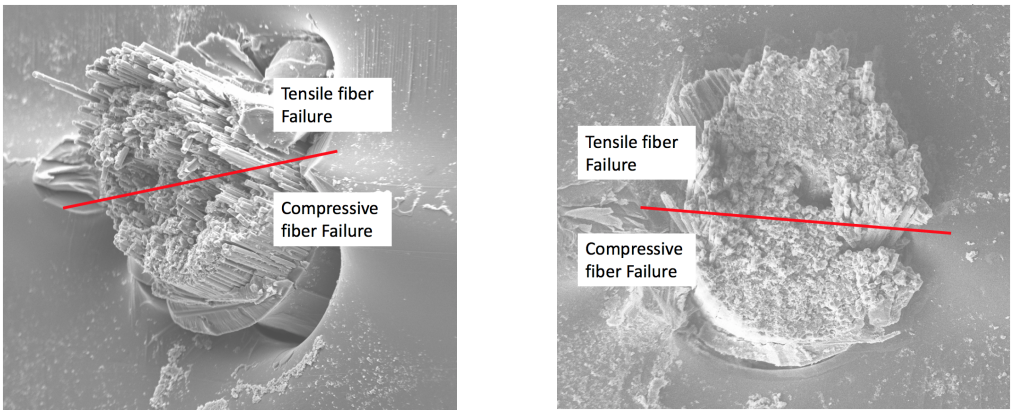
Figure 4.11: High rate mode II response (a) bridging response of Z-pins, (b) velocity profile. Data adapted from Ref. [12]

On the other hand, the mode II tests conducted at high rate were corrected for the inertia effect, as sufficient data were available in the post-failure regime. Although in Ref. [12] a near constant velocity of 1.5m/s was reported for the tests , the post-processing of the raw data presented here proves that such a steady state speed was not achieved, as illustrated in fig. 4.11b. Similar to the quasi-static test, once Z-pins failed, each specimen suddenly accelerates, as confirmed by the velocity profile of T1 test shown in fig. 4.11b. In the latter, a sharp increase in velocity is observed at a displacement of 0.12mm, which corresponds to the peak load that the Z-pins sustained immediately before failure.



(a) (b)

Figure 4.12: Mode II bridging response for specimen T3 at quasi-staic loading as a function of (a) Displacement and (b) Time. Data adapted from Ref. [12].



(a) (b)

Figure 4.13: Scan Electorn Microscopy image of the Z-pin fracture surface under mode II loading at (a) quasi-static and (b) high rates. Images courtesy of Dr. Hao Cui.

After the mode II test, it was observed that all the Z-pins where sheared out, regardless of the loading rate. Upon SEM inspection, the failed Z-pin cross section presented two distinct areas. In the first (zone 1), Z-pin fibres are irregularly pulled-out and failed at different locations (see fig. 4.13). The second area (zone 2) is characterised by the fibres failing more or less at the same location(see fig. 4.13), with evidence of micro-buckling. This failure morphology is due to the Z-pin bending, whereby one half of the cross section is subject to tension, while the other side is under compression. Thus, the observed failure in zone 1 corresponds to tensile fibre failure, while that in zone 2 is clearly representative of compressive fibre failure. The failure morphology appears unaffected by the loading rate. This explains the similarity of the dissipated energy values (area under force-displacement graph) in figs. 4.10a and 4.11a for Z-pins tested in mode II under quasi-static and high-rate loading.

4.3.3 Mixed Mode

The quasi-static bridging response under mixed-mode loading of Z-pinned coupons is presented in fig. 4.14. The mode mixity achieved during the test

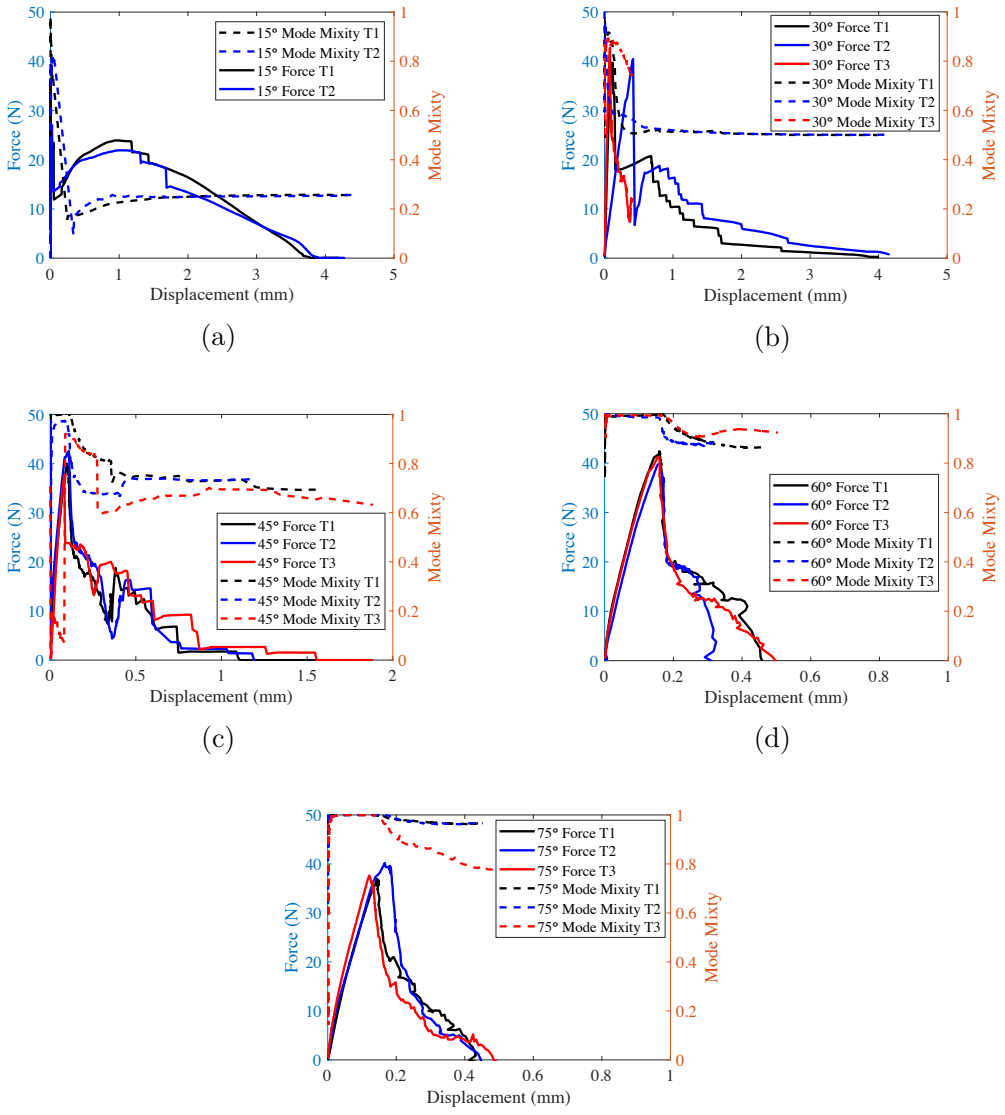
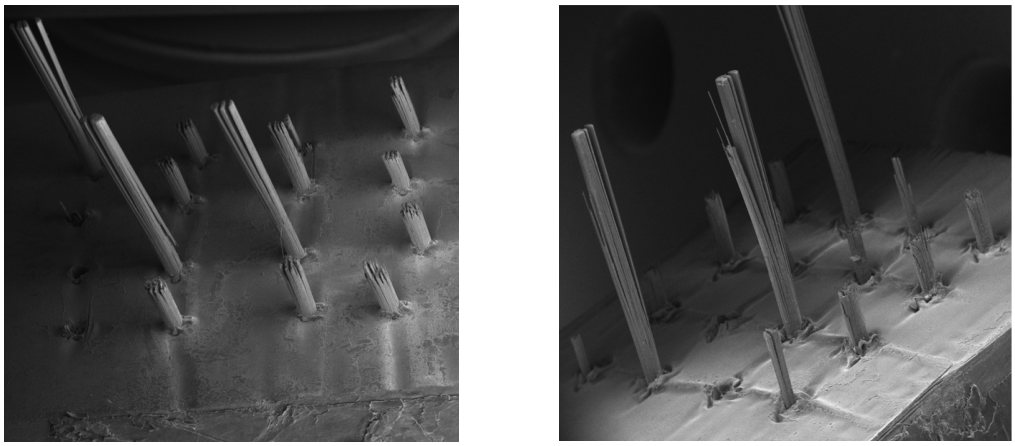


Figure 4.14: The quasi-static bridging response and mode mixity achieved in mixed mode loading with Z-pin mixed mode angle of (a) 15°, (b) 30°, (c) 45°, (d) 60° and (e) 75°, where 0° is pure mode I and 90° is pure mode II. Data adapted from Ref. [13].



(a) (b)

Figure 4.15: SEM image of the failure surface of Z-pinned laminate subject to quasi-static loading with a mixed mode angle of (a) 15° and (b) 30°. Images are courtesy of Dr. Hao Cui.

was obtained from DIC and it is here presented on the same graph as the bridging response (see fig. 4.14).

At low mode mixity values, i.e. corresponding to a nominal loading angle (β) of 15° and 30°, the recorded displacement reaches to the full half-embedded length of approximately 4mm (see figs. 4.14a and 4.14b). This might erroneously lead to thinking that the Z-pins failed because of complete pull-out, similar to what occurred in the mode I response. However, since the load offset angles of 15° and 30° are significantly larger than any misalignment observed in the mode I case, one should expect that a complete pull-out response at these mode mixities would result in larger bridging forces compared to mode I. This should happen because of the friction enhancement due to snubbing becomes stronger as the mode-mixity increases (as explained section 4.3.1). Considering that the response seen in figs. 4.14a and 4.14b results from the overall behaviour of the 16 Z-pins in each coupon, it is reasonable to speculate that some of those experienced full pull-out, whereas the remaining ones failed prematurely.

Such a "mixed" behaviour, where individual TTR may randomly fail or

pull out completely despite being loaded at the same mode-mixity, has been extensively discussed in the literature by Yasaee et al. [83]. The latter authors introduced the concept of transition region, to indicate the range of mode-mixity values within which Z-pin may either pull-out or fail in an almost random fashion. For quasi-isotropic laminates and embedding lengths in the order of 10 mm, the transition region spanned the mode-mixity range between 30° and 40°. However, the results from Ref. [83] were obtained on a much earlier generation of Z-pin rod-stock, which was affected by significant void content, as a result of poor consolidation during pultrusion. The Z-pins considered here belong to a later generation, made of the same material (i.e. T300/BMI), but for which the manufacturing process has been optimised, improving consolidation and reducing void content to a negligible level. However, this has actually increased the brittleness of the TTR, especially under mode II conditions; earlier generation Z-pins were prone to extensive internal splitting [83], which contributed a level of pseudo-ductility under shear and pushed the transition region towards larger mode-mixity angles compared to the later generation of TTR considered here.

SEM images taken from the failed specimens are shown in fig. 4.15. These show that 9 and 13 Z-pins out of 16 failed by fracture for the mixed-mode angles of 15° and 30°, respectively. This proves the fact that a "mixed" failure behaviour actually occurs in the coupons reinforced by Z-pin arrays, as speculated above. In terms of response, this causes the "stair-case" force trend in the pull-out region that is observed in fig. 4.14a . The stair case response can be directly linked to individual Z-pin fracture events within the coupon. The pulled-out Z-pins actually exhibit splitting (See fig. 4.15), which, as mentioned above, makes the TTR more compliant and hence enables complete pull-out by delaying bending-driven fibre failure.

It is also interesting to note that the transition region observed here starts at a mixed mode angle of 15°. That is significantly earlier than that reported in Ref. [83], confirming that the improvement of the pultrusion process have actually led to an increased susceptibility to fibre failure.

At higher mode mixities, i.e. for angle of 45°, 60° and 75°, the response shows an almost monotonic rise to a peak force to around 40N, followed by a sharp drop to zero (see fig. 4.14). This suggests that all the Z-pins fractured, a circumstance that is confirmed by the SEM images of the specimens (see

fig. 4.16). Nonetheless, it is worth noting that there is a slight stair case response trend beyond the peak force in fig. 4.14c for the mixed mode angle of 45°. Clearly this cannot be due to the pull-out of surviving Z-pins, since all the TTR rods failed. The trend is actually due to inertial effects, since once the Z-pins start breaking, the specimen and the fixture accelerate. This can be verified by observing the velocity response shown in fig. 4.17, which displays large accelerations at a displacement of about 0.1mm, which also corresponds to the load drop. Therefore, it can be concluded that the all Z-pins undergo sudden brittle failure.

It is very important to remark that the dynamic response presented in figs. 4.18 and 4.20 is very similar to that of the quasi-static tests, at least from a qualitative point of view. At low mode mixity values, i.e. at mixed mode angle of 15° and 30°, some Z-pins experience complete pull-out while others fracture, regardless of the loading rate. The bridging response obtained from these tests is always an average resulting from the behaviour of the 16 Z-pins in the coupons (see fig. 4.18). Overall, this suggests that the extent of the transition region as independent from the loading rate.

The dynamic loading at higher mode-mixity values, corresponding to 45°, 60° and 75° loading angles, is shown in fig. 4.20. Similar to the quasi-static

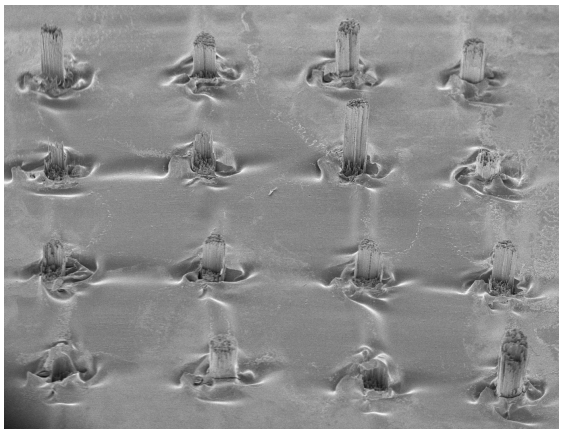


Figure 4.16: SEM image of the failure surface of Z-pinned laminate subject to quasi-static loading under a mixed mode angle of 45°. Image is courtesy of Dr. Hao Cui.

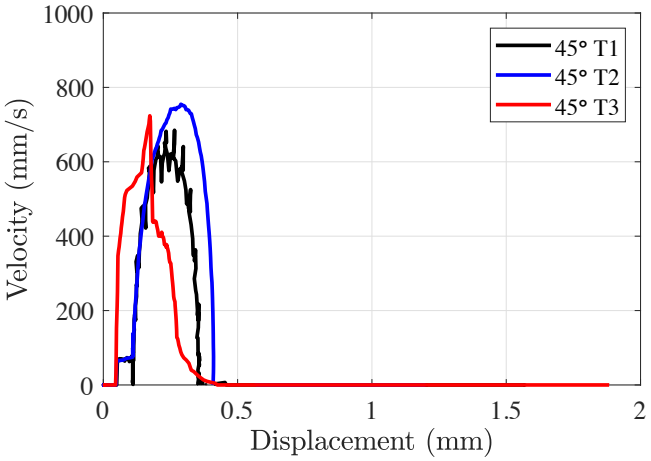


Figure 4.17: The Velocity profile of the Z-pin response subject to quasi-static loading for a mixed mode angle of 45°. Data adapted from Ref. [13].

case, all the Z-pins failed by brittle fracture (see fig. 4.19). This explains the response trends presented in fig. 4.20.

It is worth noting that in both the quasi-static and dynamic mixed-mode test cases, the mode mixity was not constant throughout the test, as shown in figs. 4.14, 4.18 and 4.20. The test always start in a mode II dominated regime; the mode-mixity converges to the intended value as the test progresses and the overall displacement increases. In the case of the smaller loading angles (β equals 15° and 30°), the bulk of the pull-out response occurs at the intended mode-mixity. However, the relatively high mode mixity at the start of the test could have contributed to the earlier failure of some Z-pins. For higher loading angles, i.e. 45° up to 75° ,the initial mode mixity was very close to pure mode II. The intended mode mixity was achieved in all these test *after the Z-pins had already failed*. Hence, all the aforementioned tests are actually dominated by mode II and they do not provide information about the Z-pin behaviour at the nominal loading angle prescribed for the experiments, since the latter is actually attained only after all the TTR rods have experienced failure. This point is further proved by plotting the response from the 3 different mixed-mode angles of 45°, 60° and 75° on the same graph (see fig. 4.21). The corresponding bridging responses are very similar and within the level of scatter that one would see in mode I dom-

inated cases, where the intended mode mixity was actually reached during most of the pull-out response. The modest differences in the response in the range of mixed mode angles of 45° to 75° could be attributed to the different populations of misalignment angles in the Z-pin arrays or perhaps to the different loading rate, since the imposed opening and sliding speeds are not the same (although similar) in any of the tests.

So far it has been demonstrated that, due to intrinsic limitations with the test set-up, all the tests performed with loading angles exceeding 45° are actually almost pure mode II tests, since the target mode-mixity value is reached only after the Z-pins have failed. Hence, it would be reasonable

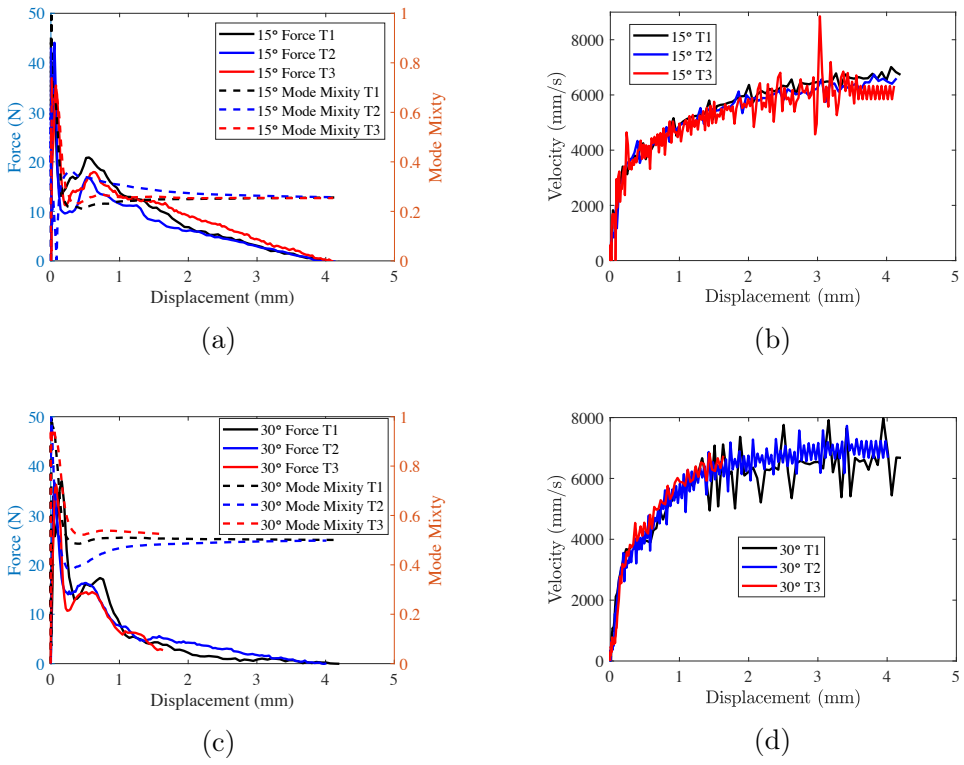


Figure 4.18: The dynamic bridging response and mode mixity achieved in mixed mode loading with mixed mode angle of (a) 15° and (c) 30° with the corresponding velocity profile attained in (b) and (d) respectively. Data adapted from Ref. [13]

to expect that the results of these tests agree with those carried out in pure mode II, i.e. for a loading angle of 90°, presented in fig. 4.22. However, this is not the case. The pure mode II response is stiffer than that for a mixed mode angle of 75°, reaching a peak load close to 50N, which is 25% higher than that attained in the tests at loading orientations $\geq 45°$. This difference is due to the fact that the brass sleeve used in the experiments fully prevents any opening displacement in the mode II tests. Because of the Z-pin misalignment, coupons always tend to experience some small opening, even under pure mode II (See Ref. [167]). If the latter opening displacement is suppressed, it implies that a normal closing force will act on the bridged interface, causing additional friction that will make the response look stiffer and the peak force larger. For this reason, the pure mode II tests reported here have limited significance. The actual mode II behaviour is that which has been characterised from the experiments with loading angles $\geq 45°$. It is also worth pointing out that the presence of the brass sleeve is the likely cause of the veering towards mode II conditions that is common to all the mixed-mode experiments, so an alternative experimental arrangement, such as a much lighter sleeve, should be considered for future TTR characterisations.

4.3.4 Energy Absorbed

The use of Z-pins provides an increase in apparent fracture toughness due to energy dissipated as the Z-pin is pulled out and/or broken. For carbon-based TTR, frictional pull-out usually provides an energy dissipation one order of magnitude larger than Z-pin failure. Hence, Z-pins tend to be much more



Figure 4.19: SEM image of the failure surface of Z-pinned laminate subject to dynamic loading under a mixed mode angle of 75°. Image is courtesy of Dr. Hao Cui.

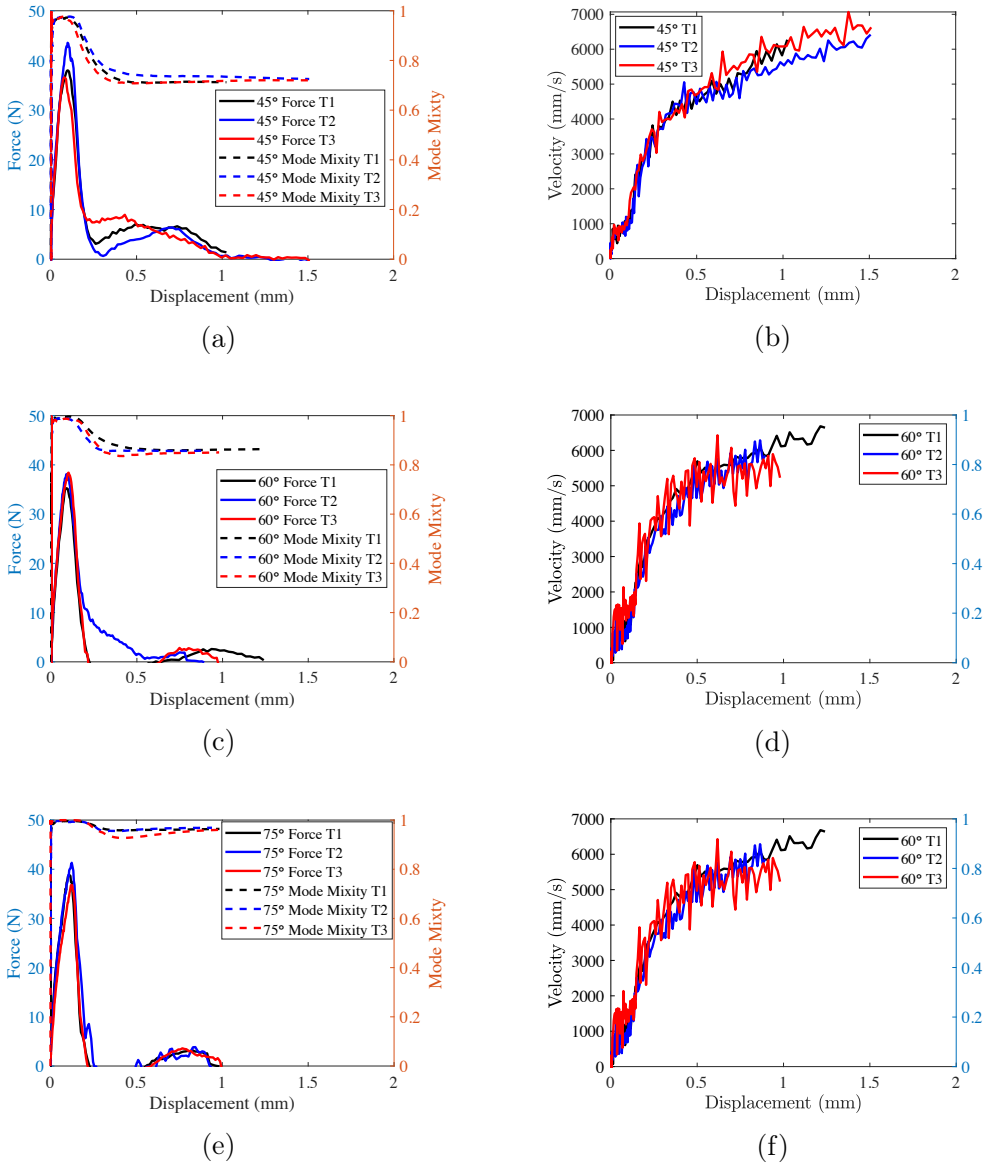


Figure 4.20: The dynamic bridging response and mode mixity achieved in mixed mode loading with mixed mode angle of (a) 45°, (c) 60° and (e)75° with the corresponding velocity profile attained in (b), (d) and (f) respectively. Data adapted from Ref. [13]

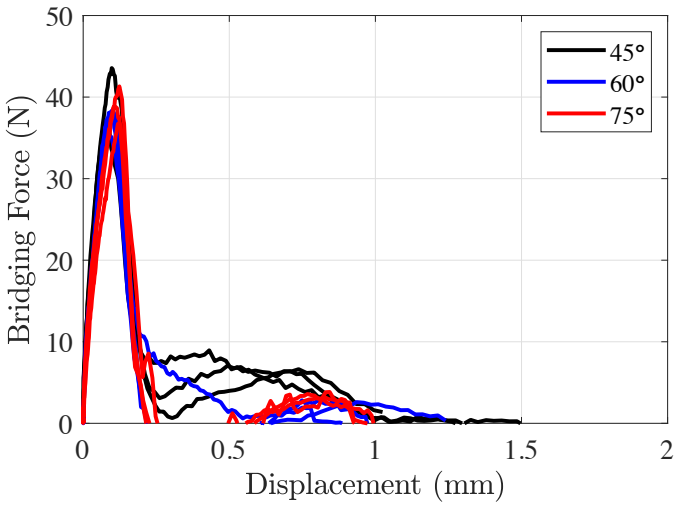


Figure 4.21: Dynamic bridging response for the three high mixed mode angles of 45°, 60° and 75° plotted on the same graph. Data adapted from Ref. [13].

effective in mode I than in mode II. This is a direct consequence of the inherent brittleness of T300/BMI Z-pins under shear and bending. The dissipated energy is therefore strongly dependent on the mode-mixity and, in principle, on the loading rate. A graph of the energy dissipated as a function of the nominal mixed mode angle and different loading rates is shown in fig. 4.23. Although the nominal loading angle is used in the graph, it is worth pointing out that mode-mixity was not constant during the tests, as extensively discussed in the previous section. Furthermore, the loading rate is different from test to test, with no dynamic equilibrium achieved. Nonetheless, the dynamic tests were largely conducted at similar peak rate of around 6m/s, with the exception of the test conducted at around 12m/s and 2m/s for the nominal mixed mode angles of 9° and 90° respectively.

As shown in fig. 4.23, the energy dissipated in both quasi-static and dynamic loading initially increases with the nominal mixed-mode angle, peaking at 9°; then it decreases sharply in the transition region. The energy dissipated at loading angles beyond the transition region ($\geq 45°$) remains fairly constant. This is due the fact that, beyond the transition region, the failure mechanism consists in fracturing of the Z-pins, with no actual pull out.

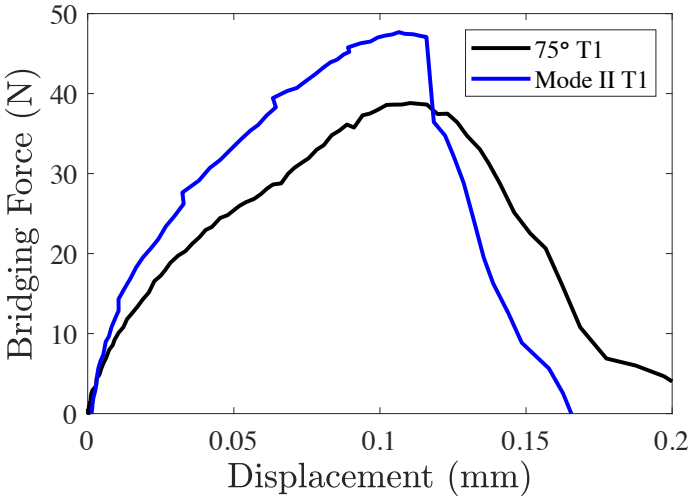


Figure 4.22: Dynamic bridging response for mixed mode angle of 75° and Mode II plotted on the same graph. Data adapted from Ref. [12, 13].

On the other hand, the higher the loading rate, the lower the energy absorbed at low mixed mode angles, i.e. $0° < \beta < 30°$. This is due to the failure process being dominated by complete Z-pin pull-out, where most of the energy is dissipated during the sliding friction response. Since the sliding friction has negative rate sensitivity, as explained in the previous section, then the energy dissipated decreases with increasing loading rate. However, for higher mixed-mode angles ($\beta > 45°$), the energy absorbed is rate insensitive (see fig. 4.23). This is due to the fact that Z-pin rupture is driven by tensile and compressive fibre failure, but the mechanical performance of T300 fibres are unaffected by rate (Ref. [168]). Therefore, no influence of rate affects the energy dissipated at mode-mixity values beyond the transition region.

4.4 Summary

It is extremely difficult to conduct meaningful dynamic tests (velocity of the order of meters per second) on a single Z-pin, since the force output would be too small to be reliably measured with state-of-the-art equipment. Therefore, an array of 16 (4x4) Z-pins, each 1.75mm apart from the other (corresponding

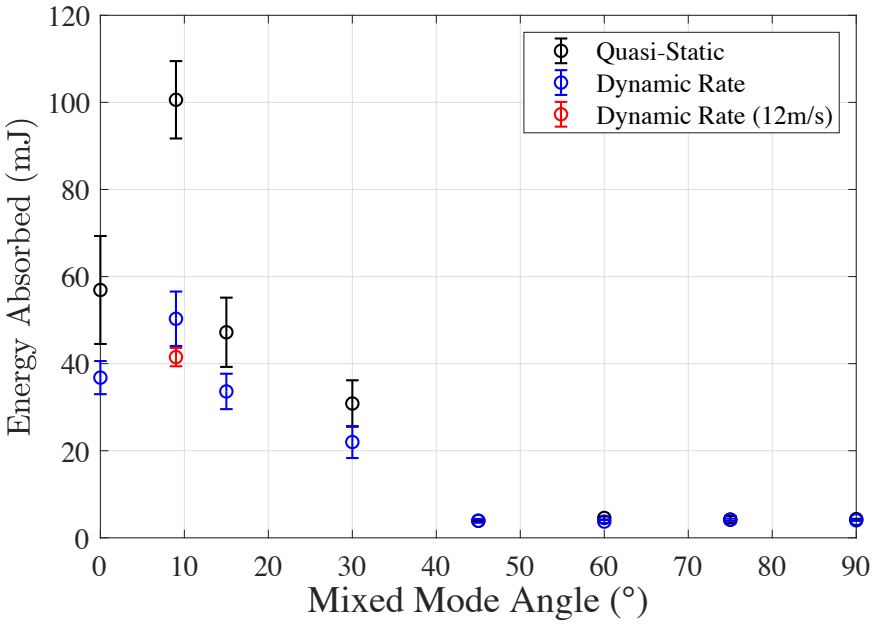


Figure 4.23: Energy absorbed as a function of the nominal mixed mode angle for different loading rates.

to 2% TTR areal density) were considered in the tests. Hence, the resulting experimental bridging force was divided by 16, to represent a single Z-pin response. Tests were conducted in quasi-static and dynamic conditions, with opening and sliding speeds ranging from 0.01mm/s to 12m/s, and across the full mode-mixity spectrum.

The use of a brass sleeve in the test set-up is the reason why the mode mixity is not constant during each test. However, the intended mode-mixity was achieved in the frictional pull-out stage of the Z-pin response for a lower range of loading angles ($\beta \leq 30°$). For larger loading angles, the target mode-mixity was achieved after the Z-pins had failed. This implied that most of these tests were actually carried out in a regime that was much closer to mode II than what had initially been anticipated. Furthermore, the use of the brass sleeve causes friction, which skews the bridging force measurement. This effect is especially significant in the mode II tests, which gave a stiffer bridging response for the loading angle of 90° compared to 75°, despite the

fact that the actual mode mixity value in both tests were very close, as confirmed by high-speed DIC. Therefore, the results of the pure mode II tests will not be considered in the remainder of this work.

The energy dissipated under pure mode I loading (misalignment angle of 0°) is significantly larger than that spent under pure mode II, by a factor of 13 and 9 for quasi-static and dynamic loading, respectively. The higher energy absorbed in pure mode I is due to the Z-pins failing by complete frictional pull-out. On the other hand, under pure mode II loading, the Z-pins failed by brittle fracture, thus absorbing relatively little energy. Under mode II loading, the Z-pin failed in bending. SEM images confirmed that the fibres on the half of the TTR cross section subject to compression collapsed due to micro-buckling, whereas on opposite half clear evidence of tensile fibre failure was found .

Increasing the mixed mode angle slightly to 9° doubled the energy dissipated by the Z-pins. This is due to the enhanced friction arising from the snubbing phenomenon. A further increase of the mixed mode angle to 15° and 30° resulted in the energy dissipated being reduced. This reduction is due to the Z-pins operating in failure transition region, where some Z-pins fail by complete pull-out while others fractured. Thus the resulting response is an average of the behaviour of 16 individual Z-pins, whereby those pulled-out dissipated a much larger amount of mechanical energy due to the sliding friction compared to those that fractured. Beyond the transition region, $\beta \geq 45°$, all the Z-pins fail in a brittle fashion. Consequently, the energy absorbed is nearly constant and one order of magnitude smaller than that dissipated in mode I dominated regimes.

Increasing the loading rate decreases energy dissipated and hence the effectiveness of Z-pins in pure mode I loading up to the transition region. The energy absorbed at a loading angle angle of 9° decreases by 60% as the loading rate increases from 0.01mm/s to 12m/s. A reduction in sliding friction is the primary factor controlling this drop in energy dissipation at the same actual mode-mixity. SEM images reveal that, whereas shear cusps and debris are visible on the Z-pin/laminate sliding interface after quasi-static pull out, the same interface appears smooth at high loading rates. The pull out speed therefore strongly influences the amount of friction that develops as the Z-pin slides within the laminate. However, the Z-pin performance is

insensitive to rate beyond the transition region, $\beta \geq 45°$, since the amount of pull out is negligible and the energy dissipation is governed by fibre failure, which is not influenced by rate if the TTR is made of carbon fibre as in the present case.

4.4.1 Test Matrix Summary

A total of 47 tests have been conducted at quasi-static and high loading rates. These tests were done under different nominal mode mixities and nominal test speeds. A summary of all the tests conducted is porvided in table 4.1 and table 4.2 for the quasi-static and high rate tests. In addition, table 4.1 and table 4.2 provide details of the sample results used for calibration and validation of the mode I and mixed mode models developed in chapter 5 and 6 respectively.

Misalignment angle	0°	9°	15°	30°	45°	60°	75°	90°
Nominal Mode Mixity	0	0.156	0.259	0.5	0.707	0.866	0.966	1.00
Nominal Speed (mm/s)	0.01	0.01	0.01	0.01	0.01	0.01	0.01	0.01
Test Samples	T1, T2	T1,T2,T3	T1,T2	T1,T2,T3	T1,T2,T3	T1,T2,T3	T1,T2,T3	T1,T2,T3
Used for mode I model calibration	n/a	T1,T2	n/a	n/a	n/a	n/a	n/a	n/a
Used for mode I model validation	n/a	T3	n/a	n/a	n/a	n/a	n/a	n/a
Used for mixed mode model calibration	T1	T1	n/a	n/a	n/a	n/a	T1	n/a
Used for mixed mode model vaildation	T2	T2,T3	T1,T2	T1,T2,T3	T1,T2,T3	T1,T2,T3	T2,T3	n/a

Table 4.1: Summary of the test matrix for quasi-static testing.

Misalignment angle	0°	9°	9°	15°	30°	45°	60°	75°	90°
Nominal Mode Mixity	0	0.156	0.156	0.259	0.5	0.707	0.866	0.966	1.00
Nominal Speed (m/s)	7	5	12	6	6	6	6	6	1.5
Test Samples	T1, T2	T1,T2,T3	T1,T2,T3	T1,T2	T1,T2,T3	T1,T2,T3	T1,T2,T3	T1,T2,T3	T1,T2,T3
Used for mode I model calibration	n/a	T1,T2,T3	n/a	n/a	n/a	n/a	n/a	n/a	n/a
Used for mode I model validation	n/a	n/a	T1,T2,T3	n/a	n/a	n/a	n/a	n/a	n/a
Used for mixed mode model calibration	T1	T1	n/a	n/a	n/a	n/a	n/a	T1	n/a
Used for mixed mode model vaildation	T2	T2,T3	T1,T2,T3	T1,T2	T1,T2,T3	T1,T2,T3	T1,T2,T3	T2,T3	n/a

Table 4.2: Summary of the test matrix for high rate testing.

Chapter 5

Mode I Z-pin Bridging Model

5.1 Introduction

Fibrous Z-pins are very efficient in increasing the apparent fracture toughness under mode I loading. The increase in apparent fracture toughness is due to the Z-pin exerting a bridging force on the delamination interface. In this chapter, a reduced order model capable of assessing the mode I rate-dependent bridging performance of Z-pins is presented. The proposed model is based on representing the Z-pin as a peridynamic rod using the formulation developed in section 3.3.1.

The external forces acting on the Z-pin is governed by the Z-pin/laminate bond state (i.e. whether the Z-pin is bonded or debonded from the surrounding laminate). As the crack opening displacement increases the bonded Z-pin elastically deform. At certain point, the Z-pin begins to debond from the surrounding laminate causing residual friction to act along the debonded region. Once the Z-pin fully debonds sliding friction acts on the interface. An appropriate model for the external force acting on the Z-pin in the bonded phase and up to sliding frictional pull-out is developed in this chapter. However, experimental observation shows that the majority of energy absorption occurs in the sliding frictional phase during Z-pin pull-out (see chpater 2). Consequently, two models including and ignoring the debonding stages are presented and compared in this chapter.

The sliding friction in the pull-out stage is observed to be rate depen-

dent as discussed in chapter 4. Therefore, a state-dependent friction model is employed to describe the effect of the displacement rate on Z-pin pull-out in mode I loading conditions.

The developed model is calibrated and validated against mode I (with 9° misalignment) experimental results presented in chapter 4. The obtained results are in excellent agreement with experimental high-rate and quasi-static data presented in the previous chapter.

5.2 Model Formulation

5.2.1 Problem Description

A Z-pin of length L is inserted into a composite laminate. A delamination intersects the Z-pin at a known depth, splitting the embedding laminate into a "top" and a "bottom" region of thickness L^+ and L^-, respectively. It is hereby assumed, without loss of generality, that $L^- \leq L^+$. The top sub-laminate starts moving with absolute speed $\dot{W}$ at the time instant $t = 0$, while the bottom foundation is considered fixed. Both sub-laminates exert axial forces on the Z-pin, which depend on the bonding state of the associated interfaces. Consequently, the Z-pin counteracts the delamination opening displacement by exerting equilibrated bridging tractions on the interlaminar crack surfaces.

Three different stages of the Z-pin response are here considered:

1. the "bonded" stage, when the laminate reacts to the relative Z-pin displacement as an elastic foundation having stiffness k_z; the reference configuration for this stage of the Z-pin response is presented in fig. 5.1a.

2. The "progressive de-bond" phase; this occurs when the Z-pin/laminate interface fails due to the growth of a cylindrical mode II crack on the lateral surface of the TTR (through thickness reinforcement) rod. The reference configuration for this phase of the Z-pin response is illustrated in fig. 5.1b, where L_d^- and L_d^+ denote the debond lengths in the bottom and top Z-pin segments, respectively. The bonding/debonding state is

represented via a local boolean variable $d(z)$, which takes zero value for a pristine interface and unit value after the Z-pin/laminate bond fails. When $d(z) = 1$, a local frictional interaction develops along the Z-pin circumference corresponding to the axial coordinate z.

3. The "frictional pull-out" stage, when the entire Z-pin segment in the bottom sub-laminate is de-bonded and it experiences sliding. This stage of the Z-pin response is illustrated in fig. 5.1c. Complete debonding is assumed to occur first for the lower, i.e. shorter, Z-pin segment. Hence, the TTR rod slides within the bottom sub-laminate and its embedded length is reduced to $L^- - W$, where W is the pull-out displacement across the initial delamination plane. The frictional force comprises an initial "residual" term at the start of the pull-out and an additional component, whose value increases as the relative sliding between the Z-pin and the laminate takes place. This effect is described using a state-dependent friction model introduced by Ruina (Ref. [169]).

The insertion asymmetry parameter α is defined as follows:

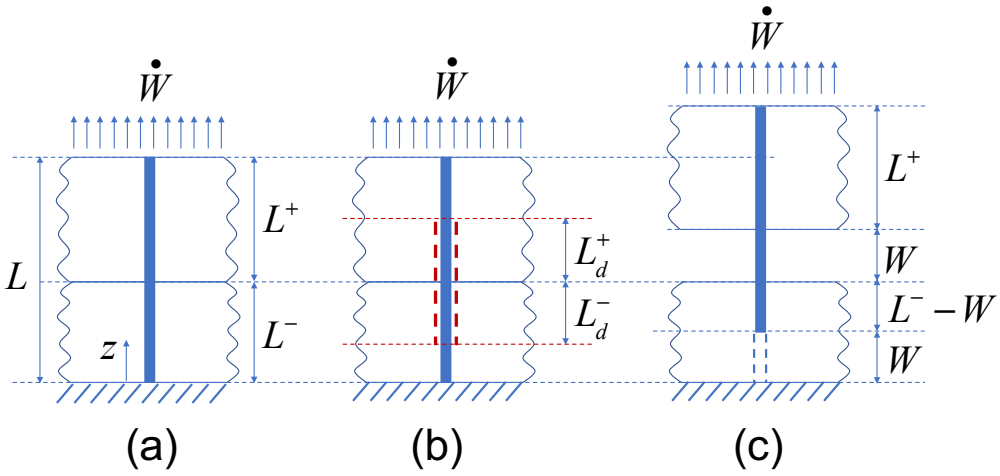


Figure 5.1: Reference configurations for the three response stages: (a) bonded Z-pin; (b) de-bonding Z-pin; (c) pull-out

$$\alpha = \frac{L^-}{L^- + L^+}, \tag{5.1}$$

which implies $L^- = \alpha L$ and $L^+ = (1-\alpha)L$. Thus, in the case of symmetric insertion (i.e. $L^- = L^+$) considered in the experimental results in chapter 4 (Ref. [12]), one finds $\alpha = 1/2$.

5.2.2 Governing Equation

The Z-pin is here described as a peridynamic rod subject to unsteady axial forces. The equilibrium equation for such a rod in bond-based peridynamics is the following:

$$\rho A\ddot{w} + b_w\dot{w} = \frac{2EA}{r_h^2}\int_{z-r_h}^{z+r_h}\frac{w'-w}{|z'-z|}dz + p(z), \tag{5.2}$$

where r_h is the horizon radius of the material particle located at point z; w and w' are the elastic displacement of the peridynamic particle at location z and z' respectively; z' represents the location of particles within the horizon of z; $\ddot{w}$ and $\dot{w}$ are the second and first derivative respectively with respect to time of the peridynamic particle at location z i.e. correspond to the acceleration and velocity of the peridynamic particle at location z; ρ, E and A are the Z-pin density, young's modulus and cross sectional area respectively; b_w is a damping coefficient. Finally, $p(z)$ is the distributed axial load acting on the Z-pin. The derivation of (eq. (5.2)) is detailed in section 3.

Let the rod be divided in N segments, each having length $\Delta z = L/N$ and let it be assumed that the displacement field $w(z)$ is constant within each of the segments. This leads to a "meshfree" discretization of the rod [134], whereby a peridynamic particle is located at the centre of each segment. Hence, the position of the i-th peridynamic particle is $z_i = \Delta z\left(i - \frac{1}{2}\right)$, $i = 1, 2, ..., N$. The integro-differential equation in (eq. (5.2)) can therefore be discretised as follows:

$$\rho A\ddot{w}_i + b_w\dot{w}_i = I_i + p_i, \tag{5.3}$$

where $\ddot{w}_i = \ddot{w}(z_i)$, $p_i = p(z_i)$. The integral on the rights hand side of

(eq. (5.2)) is approximated via a Riemann sum [134], i.e.

$$I_i = \frac{2EA\Delta z}{r_h^2} \sum_{\substack{j \neq i \\ j=i_1}}^{i_M} v_c(ij) SCF_i \frac{w_j - w_i}{|z_j - z_i|}, \tag{5.4}$$

where v_c and SCF are the volume and surface correction factors; i_1, i_2, ..., i_M are the M particles in the horizon H_{z_i} of the i-th particle.

Time integration of (eq. (5.3)) is conducted by using an explicit second-order centred finite difference discretisation with respect to time [134, 156]. Applying the numerical scheme to eq. (5.3) leads to:

$$\rho A \frac{w_i^{(n+1)} - 2w_i^{(n)} + w_i^{(n-1)}}{\Delta t^2} + b_w \frac{w_i^{(n+1)} - w_i^{(n-1)}}{2\Delta t} = I_i^{(n)} + p_i^{(n)}, \tag{5.5}$$

where Δt is the time step; the superscript (n) denotes the n-th time instant. Substituting eq. (5.4) into eq. (5.5) and solving with respect to $w_i^{(n+1)}$ yields the following time-marching solution:

$$w_i^{(n+1)} = \frac{4w_i^{(n)} - (2 - \chi_w \Delta t)\, w_i^{(n-1)} + 4\left(\frac{\Delta t}{t_h}\right)^2 J_i^{(n)} + 2\Pi_i^{(n)}}{2 + \chi_w \Delta t}, \tag{5.6}$$

where:

$$\chi_w := \frac{b_w}{\rho A}, \quad t_h := r_h \sqrt{\frac{\rho}{E}}, \quad J_i^{(n)} := \Delta z \sum_{\substack{j \neq i \\ j=i_1}}^{i_M} \frac{w_j^{(n)} - w_i^{(n)}}{|z_j - z_i|}, \quad \Pi_i^{(n)} := \frac{p_i^{(n)} \Delta t^2}{\rho A}. \tag{5.7}$$

Note that the second of eq. (5.7) represents the time taken for an elastic axial wave to travel across half the horizon of a particle.

5.2.3 Lateral Foundation and Frictional Forces

Based on the problem description in sec. 5.2.1, it follows that the expression of the lateral frictional force per unit length for a bonded Z-pin/laminate interface is

$$p(z) = -k_z w_r(z) \tag{5.8}$$

where k_z is the elastic foundation stiffness with units of N/mm^2, and $w_r(z)$ is the relative displacement between the Z-pin and the surrounding laminate at location z. Once the Z-pin/laminate interface fails (debonding criterion discussed in sec. 5.2.5) frictional contact develops between the Z-pin and surrounding laminate.

Allegri et al. [99] described single Z-pins as inextensible Euler-Bernoulli beam embedded in an elastic foundation. They neglected the bonded and progressive de-bonding stages of the TTR response and focussed on the friction governing the pull-out stage. They observed that, when the Z-pin is fully debonded, it experiences a level of friction that depends on the pull-out displacement. Based on experimental observation, the following dependency of the friction force per unit length was inferred [99]:

$$p = p_\infty + (p_0 - p_\infty)\, e^{-W/\ell}, \tag{5.9}$$

where p_0 is a baseline frictional force value at the start of the pull-out, ℓ is a characteristic length scale for the evolution of the frictional interaction, p_∞ is a steady-state value of the frictional force per unit length and, finally, W is the pull-out displacement. Allegri et al. [99] observed that $p_\infty > p_0$, i.e. the friction force tended to increase with the pull-out displacement and reach an asymptotic plateau (explanation of such observation is presented in Chapter 4). Since the Z-pin was assumed to be inextensible, the "rigid" pull-out displacement W also represented the relative sliding between the TTR rod and the embedding laminate. The model in Ref. [99] was developed for quasi-static bridging. Thus, it does not take into account the effect of the actual sliding speed, which in principle varies locally along the Z-pin during high rate pull-out if the TTR is assumed to stretch axially as postulated here.

To take into account the effect of speed on sliding friction, another rate-dependent friction model is developed and implemented at higher rate based on Ruina's friction model (Ref. [169]). The Ruina state-based friction model is governed by the following equations [169]:

$$\begin{aligned} \tau &= \sigma \left(\mu_0 + \phi + A \log \left| \frac{\dot{w}_r}{V_c} \right| \right), \\ \dot{\phi} &= -\frac{|\dot{w}_r|}{\ell} \left(\phi + B \log \left| \frac{\dot{w}_r}{V_c} \right| \right), \end{aligned} \tag{5.10}$$

where τ is the frictional shear stress that arises between two surfaces in contact, which slide with respect to each other with relative velocity $\dot{w}_r$; σ is the compressive contact stress between the two aforementioned surfaces. In eq. (5.10), μ_0 denotes a reference coefficient of friction. The variable ϕ is an additional coefficient of friction that tracks the "state" of the interface. The latter evolves as relative sliding with speed $\dot{w}_r$ takes place; ℓ is again a characteristic length scale for the interface evolution. The coefficient A and B are empirical constants that need to be calibrated by means of experimental data. For $|\dot{w}_r| \leq V_c$, the logarithmic terms in Eqs. (5.10) are set to zero, i.e. the dependency of the friction on the sliding speed is neglected. Hence, V_c is usually denoted as a "cut-off" speed. It is worth pointing out that in Ruina's model no a-priori assumption is introduced regarding the signs of the constants A and B and this gives the model plenty of versatility for describing the effect of the sliding speed on friction. The frictional force can therefore exhibit either a positive or a negative dependency on rate and the state variable can describe either a reduction or an enhancement in friction, all depending on the signs of A and B, as well as their relative magnitude.

Considering the Z-pin pull-out in pure mode I, σ denotes a compressive radial stress on the TTR surface, while τ is the corresponding axial-radial frictional shear. The relative sliding speed in this case depends only on the axial coordinate z, i.e. $\dot{w}_r = \dot{w}_r(z)$. Moreover, it is here assumed that the compressive stress σ has the same distribution around the periphery of the Z-pin for any given z. Hence, the resulting frictional force per unit length p caused by the sliding of the Z-pin within the laminate can be expressed as

$$p(z) = \oint \tau(z, l) dl = \pi D \int_0^{2\pi} \tau(z, \psi) d\psi. \tag{5.11}$$

Substituting the first of eq. (5.10) into eq. (5.11) yields

$$p(z) = p_0^* + A^* \log \left| \frac{\dot{w}_r(z)}{V_c} \right| + \Phi(z), \tag{5.12}$$

where

$$p_0^* = \pi D \mu_0 \int_0^{2\pi} \sigma(\psi) d\psi, \quad A^* = \pi D A \int_0^{2\pi} \sigma(\psi) d\psi, \tag{5.13}$$

and

$$\Phi(z) = \pi D \phi(z) \int_0^{2\pi} \sigma(\psi) d\psi. \tag{5.14}$$

Multiplying the second of eq. (5.10) times σ and integrating around the periphery of the Z-pin lead to the following state evolution equation:

$$\dot{\Phi}(z) = -\frac{|\dot{w}_r(z)|}{\ell}\left[\Phi(z) + B^* \log\left|\frac{\dot{w}_r(z)}{V_c}\right|\right], \tag{5.15}$$

where

$$B^* = \pi D B \int_0^{2\pi} \sigma(\psi) d\psi. \tag{5.16}$$

In summary, at high rate the distributed axial frictional force per unit length acting along the Z-pin is obtained by solving the following equation:

$$\begin{aligned} p(z) &= p_0^* + A^* \log\left|\frac{\dot{w}_r(z)}{V_c}\right| + \Phi(z), \\ \dot{\Phi}(z) &= -\frac{|\dot{w}_r(z)|}{\ell}\left[\Phi(z) + B^* \log\left|\frac{\dot{w}_r(z)}{V_c}\right|\right], \end{aligned} \tag{5.17}$$

Considering the three stages of the response outlined above, the distributed axial force acting on the Z-pin is expressed as follows:

$$p(z) = \begin{cases} 0 & \alpha L - W < z < \alpha L \\ -k_z w_r[1 - d(z)] - d(z) f(z) & otherwise \end{cases} \tag{5.18}$$

where $d(z)$ is the boolean damage variable (see sec. 5.2.5) for the Z-pin/laminate interface; $f(z)$ is the frictional force acting on the Z-pin once debonded and is given by eq. (5.9) and eq. (5.17) in the case of quasi-static and high rate loading respectively. In eq. (5.18), the axial force acting on the Z-pin is zero in the segment that has pulled-out from the laminate.

The general expression of the relative displacement(w_r) and speed($\dot{w}_r$) is given by:

$$\begin{aligned} w_r(z) &= [1 - H(z - \alpha L + W)]\, w(z) + H(z - \alpha L)\,[w(z) - W], \\ \dot{w}_r(z) &= [1 - H(z - \alpha L + W)]\, \dot{w}(z) + H(z - \alpha L)\left[\dot{w}(z) - \dot{W}\right]. \end{aligned} \tag{5.19}$$

where, $H(x)$ for $x \in \mathbb{R}$ is the Heaviside step function, i.e. $H(x) = 1$ for $x \geq 0$ and $H(x) = 0$ for $x < 0$.

The reader can easily verify that the expressions of the relative sliding displacements and speed from eq. (5.19) are valid for all the three stages of the Z-pin pull-out described above. In particular, in the bonded and progressive de-bonding stages, the reference configuration sketched in figure. 5.1a implies $W = 0$; in this case, the terms associated with the Heaviside function in eq. (5.19) would give a relative displacement (speed) equal to w ($\dot{w}$) for $z < L^- = \alpha L$ and to $w - W$ ($\dot{w} - \dot{W}$) for $z \geq L^- = \alpha L$. In the pull-out phase, eq. (5.19) takes into account the fact that the bottom embedded length of the Z-pin is reduced to $L^- - W = \alpha L - W$; moreover, in this case, zero relative displacement and speed are obtained for $\alpha L - W \leq z \leq \alpha L$.

Considering the time-marching centred finite-difference scheme discussed in sec. 5.2.2, the discretised axial forces from eq. (5.18) read:

$$p_i^{(n)} = \begin{cases} 0 & \alpha L - W < z < \alpha L \\ -k_z w_{ri}^{(n)}[1 - d_i] - d_i f_i^{(n)} & otherwise \end{cases} \tag{5.20}$$

At high rate, the frictional force in eq. (5.20) is obtained as:

$$\begin{aligned} f_i^{(n)} &= d_i^{(n)} \left[p_0^* + A^* \log \left| \frac{\dot{w}_{ri}^{(n)}}{V_c} \right| + \Phi_i(n) \right], \\ \Phi_i^{(n)} &= \Phi_i^{(n-2)} - 2 d_i^{(n-1)} \frac{\left| \dot{w}_{ri}^{(n-1)} \right|}{\ell} \left[\Phi_i^{(n-1)} + B^* \log \left| \frac{\dot{w}_{ri}^{(n-1)}}{V_c} \right| \right] \Delta t. \end{aligned} \tag{5.21}$$

While, at quasi-static loading, the frictional force in eq. (5.20) is obtained as:

$$f_i^n = p_\infty + (p_0 - p_\infty)\, e^{\frac{-w_{ri}^n}{\ell}} \tag{5.22}$$

5.2.4 Numerical Stability

It is interesting to investigate the effect of the external applied force on the stability of the numerical scheme. Therefore, stability analysis is conducted in this section (similar to that in sec. 3.3.3) where the external applied force is assumed to be: $p(z) = k_z w$.

For this purpose, consider the time-marching scheme from eq. (5.6), let the round-off error be defined as $e_i^{(n)} = \hat{w}_i^{(n)} - w_i^{(n)}$, where $\hat{w}_i^{(n)}$ is the exact numerical solution, while $w_i^{(n)}$ is the actual displacement field obtained due to the presence of truncation errors. Let it be assumed that the damping coefficient in eq. (5.6) is zero, i.e. $\chi_w = 0$, and that $p(z) = k_z w$. Expressing the actual numerical solution as $w_i^{(n)} = \hat{w}_i^{(n)} - e_i^{(n)}$ and substituting the latter into eq. (5.6) lead to the following error-evolution equation:

$$e_i^{(n+1)} = \left(2 + \frac{k_z \Delta t^2}{\rho A}\right) e_i^{(n)} - e_i^{(n-1)} + \left(\frac{\Delta t}{t_h}\right)^2 \left[2\Delta z \sum_{\substack{k \neq i \\ k=i_1}}^{i_N} \frac{e_k^{(n)} - e_i^{(n)}}{|z_k - z_i|}\right] \quad (5.23)$$

where advantage has been taken of the fact that $\hat{w}_i^{(n)}$ exactly satisfies the algebraic equation representing the numerical scheme. Following Von Neumann's approach to stability analysis [134, 135], the error due to truncation can be expressed in the general form

$$e_i^{(n)} = \zeta^{n\Delta t} e^{j k_m i \Delta z}, \quad (5.24)$$

where ζ is in general a complex number, while k_m is a real wave-number; j denotes the complex unit number, i.e. $j = \sqrt{-1}$. For the sake of this analysis, let us assume that the peridynamic particles are numbered in order with an increasing z; the i-th peridyamic particle has in general have $N + 1$ particles in its horizon, including itself. The indexes of these particles will be $i - (N-1)/2$, ..., $i - 1$, i, $i + 1$, ..., $i + (N-1)/2$. Substituting eq. (5.24) into eq. (5.23) and considering the reordering of the particles described above yield:

$$\zeta^{\Delta t} = \left(2 + \frac{k_z \Delta t^2}{\rho A}\right) - \zeta^{-\Delta t} + 2\left(\frac{\Delta t}{t_h}\right)^2 \sum_{\substack{r \neq 0 \\ r=-(N-1)/2}}^{(N-1)/2} \frac{e^{j k_m r \Delta z} - 1}{|r|}. \quad (5.25)$$

Considering the symmetry of the terms that appear in the series on the right hand side, eq. (5.25) can be equivalently expressed in the following form:

$$\zeta^{\Delta t} = \left(2 + \frac{k_z \Delta t^2}{\rho A}\right) - \zeta^{-\Delta t} - 4\left(\frac{\Delta t}{t_h}\right)^2 \sum_{r=1}^{(N-1)/2} \frac{1 - \cos j\kappa_m r}{r}, \quad (5.26)$$

where $\kappa_m = k_m \Delta z$. Let us define:

$$S_m := \sum_{r=1}^{(N-1)/2} \frac{1 - \cos j\kappa_m r}{r} \tag{5.27}$$

One can immediately observe that, by virtue of the last definition:

$$S_m \leq 2 \sum_{r=1}^{(N-1)/2} \frac{1}{r} = 2H_{(N-1)/2} \tag{5.28}$$

where $H_{(N-1)/2}$ denotes the $(N-1)/2$-th harmonic number. eq. (5.26) leads to the following quadratic algebraic equation in $\zeta^{\Delta t}$:

$$\zeta^{2\Delta t} - 2\left[1 + G\Delta t^2 - 2\left(\frac{\Delta t}{t_h}\right)^2 S_m\right]\zeta^{\Delta t} + 1 = 0, \tag{5.29}$$

where $G = \frac{k_z}{2\rho A}$. The above equation admits the following solutions:

$$\zeta^{\Delta t} = 1 + G\Delta t^2 - 2\left(\frac{\Delta t}{t_h}\right)^2 S_m \pm \sqrt{\left[1 + G\Delta t^2 - 2\left(\frac{\Delta t}{t_h}\right)^2 S_m\right]^2 - 1} \tag{5.30}$$

The stability of the numerical scheme in eq. (5.6) is guaranteed for $\left|\zeta^{\Delta t}\right| \leq 1$, i.e.

$$\left|1 - 2\Delta t^2 \left(\frac{s_m}{t_h^2} - G\right)\right| \leq 1 \tag{5.31}$$

that is satisfied for:

$$\Delta t^2 \left(\frac{s_m}{t_h^2} - G\right) \leq 1 \tag{5.32}$$

Hence, for the time step one obtains:

$$\Delta t \leq \frac{t_h}{\sqrt{S_m - G t_h^2}} \tag{5.33}$$

Since $G > 0$, then the time step Δt for the case where an external load of $p = k_z w$ is applied is greater than that when $p = 0$. This is clear by observing that the denominator in eq. (5.33) is smaller than that in eq. (3.54). Thus it can be said that the external applied force helps to improve the stability of the numerical scheme.

5.2.5 Failure Criterion

Experimental observations (see chapter 4) for Z-pin under mode I loading conclusively show that Z-pin fails by complete pull-out from the laminate. Thus the numerical simulation is run until the pull-out displacement exceeds the Z-pin embedded length in the lower laminate (L^-).

Prior to complete Z-pin pull-out the Z-pin debonds from the surrounding laminate. The Griffith criterion is here employed to simulate the progressive fracture of the Z-pin/laminate interface. Since the foundation provided by the laminate is assumed elastic prior to failure, the following expression is readily obtained for the strain energy per unit length stored in the foundation:

$$\frac{dU}{dz} = \frac{1}{2} k_z w_r^2. \tag{5.34}$$

When de-bonding occurs in the form of a cylindrical crack on the lateral surface of the Z-pin, the elementary fracture surface increment is given by $\pi D\, dz$. Therefore the associated mode II energy release rate is

$$G = \frac{1}{\pi D} \frac{dU}{dz} = \frac{k_z w_r^2}{2\pi D}. \tag{5.35}$$

Denoting the interface fracture toughness as G_{IIc}, the combination of the Griffith criterion and eq. (5.35) yield the following relative displacement corresponding to the fracture of the interface:

$$w_r^{(f)} = \sqrt{\frac{2\pi D G_{IIc}}{k_z}}. \tag{5.36}$$

Hence, for a de-bond that has reached the axial position z, the condition for further propagation is $w_r(z) \geq w_r^{(f)}$ and the corresponding local boolean damage variable is defined as:

$$d(z) := \max\left\{ H\left[w_r(z) - w_r^{(f)} \right],\, 0 \right\}, \tag{5.37}$$

where $H(x)$ for $x \in \mathbb{R}$ is the Heaviside step function. Thus, when $d(z) = 0$ foundation stiffness forces act on the Z-pin and when $d(z) = 1$ frictional forces act on the Z-pin.

5.2.6 Convergence and Boundary Condition

The Z-pin is divided into 200 particles in all the simulations conducted. The number of particles (N) chosen was based on the results obtained in sec. 3 and on convergence study conducted (see fig. 5.2). The convergence study in fig. 5.2 is conducted for the QS loading ignoring the debonding stage and using the parameters in sec. 5.4.2. As can be seen in fig. 5.2 convergence is guaranteed when using 200 peridynamic particles.

On the other hand, to apply the boundary condition a fictitious boundary layer is added to the Z-pin in the top half of the laminate (see sec. 3.4.1). The boundary layer size is set to be equal to the horizon radius. The horizon radius is set to be equal to $r_h = 3\Delta z$ based on benchmark study conducted in Ref. [135]. The particles in the fictitious boundary layer are set to have an opening displacement/velocity equal to the laminate opening displacement/velocity in the case of quasi-static/dynamic loading.

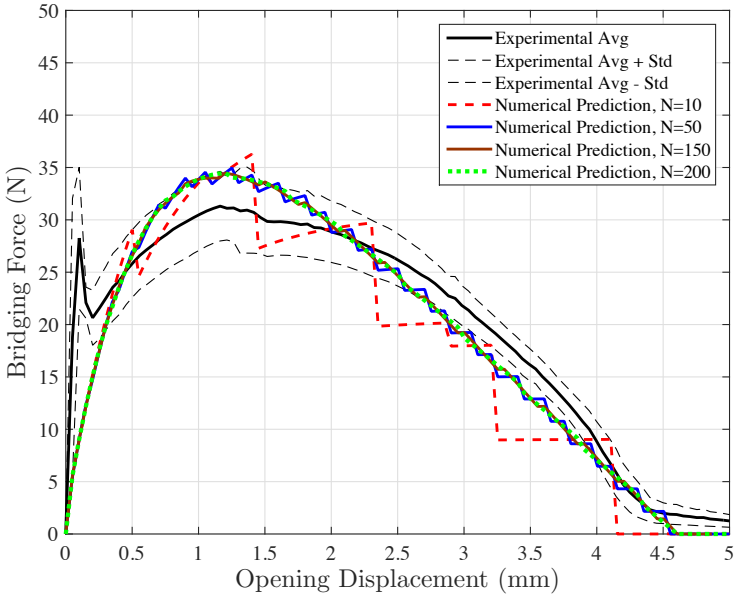


Figure 5.2: Convergence Study with different number of peridynamic particles (N)

5.3 Model Calibration

The most important output of the modelling approach proposed here is the bridging traction that an individual Z-pin exerts on the delamination surfaces during the three stages of the mechanical response discussed in sec. 5.2.1. Considering the reference configurations illustrated in fig. 5.1, the bridging force is here calculated at $z = \alpha L$, which is the point that has equal distance from the delamination surfaces when a finite displacement W is imposed on the top sub-laminate. The expression of the peridynamic force at an arbitrary location z^* on the rod is derived in Appendix C. From eq. (C.4), considering $z^* = \alpha L$, the bridging force is given by:

$$P = 2EA\left(\frac{\Delta z}{r_h}\right)^2 \sum_{i=1}^{M^-}\sum_{j=1}^{M^+} \frac{w_j - w_i}{|z_j - z_i|} v_c(ij) SCF(i) \tag{5.38}$$

where v_c and SCF are the volume and surface correction factors respectively. The index i points to the M^- particles located at $z < \alpha L$ whose horizons cross the $z = \alpha L$ location; similarly, the index j refers to the M^+ particles located at $z \geq \alpha L$ whose horizons cross the $z = \alpha L$ location.

Model constant need to be identified for calibrating the model, namely: the foundation stiffness k_z, the interface toughness G_{IIc} and the friction-related parameters p_0^*, A^*, B^*, ℓ, p_0 and p_∞ which appear in eqs. (5.21) and (5.22). Strictly speaking, also the damping coefficient b_w from eq. (5.5) and the cut-off velocity (V_c) in eq. (5.21) represents an unknown, but these have been set to 0.005 and 0.01 respectively in the analysis that follows. The Choice of V_c is based on the fact that the cut-off velocity is the velocity where rate effects are not significant and can be ignored. Quasi-static (QS) loading rate is the logical choice where rate effects are not significant. Consequently, $V_c = 0.01$ is chosen as it represents the speed at which QS tests are conducted.

The model calibration is here carried out via a genetic algorithm (GA) that minimised the cost function:

$$C = \sum_{k=1}^{Q} \left[P_k - P_k^{(e)}\right]^2_{0\&5m/s}, \tag{5.39}$$

where $P_k^{(e)}$ represents the experimental observation of the bridging traction at the k-th time instant, while P_k is the corresponding axial force obtained

from the time-marching simulations via 5.38. The subscript on the right square bracket in 5.39 means that the model calibration is carried out for the test speeds performed at the nominal speed of 5 m/s and at quasi-static rate.

5.4 Results

The Z-pin geometric and mechanical properties are defined in Table 5.1. L, D, E, ρ and α are respectively the Z-pin length, diameter, Young's Modulus, density and insertion asymmetry.

E(GPa)	ρ(kg/mm^3)	L(mm)	D(mm)	α
115	1.6E-6	8	0.28	0.5

Table 5.1: Mechanical and physical properties of a T300/BMI Z-pin [12].

Two models, including and ignoring the debonding stage, have been studied. It was observed that the foundation stiffness (k_z), the mode II fracture toughness (G_{IIc}) and the residual friction (p_0) were rate dependent (reasons discussed in next section). The lack of experimental data means that a model can not be fit to describe the rate dependent variation in these parameters i.e. different parameter values need to be used at each loading rate. Therefore, the model including the debonding stage was not suitable to be used at all rates. However, the model is presented here to prove the capability of reduced order model to simulate all the three stages of Z-pin response under mode I loading. In addition, once more experimental data becomes available, then a suitable rate dependent model for these parameters can be developed and this model can be readily used.

On the other hand, another model ignoring the debonding stage had been developed. In this model, the parameters does not need to be changed for each loading rate making the model capable of predicting the bridging performance at different loading rate.

5.4.1 Model 1: Including the Debonding Stage

The genetic algorithm optimisation conducted have yielded the results shown in tables 5.2 and 5.3. As evident in table 5.2, the parameters k_z, G_{IIc} and p_0 take a different value for each loading rate. It is physically feasible for the values of k_z and G_{IIc} to vary with loading rate i.e. to be rate dependent. This is the case because the interface properties are governed by the resin which is rate dependent and hence rate effects are present. However, the accuracy of these values is questionable due to the presence of inertial effect in the debonding region for the 5m/s and 12m/s cases. It is worth noting that the obtained G_{IIc} is much lower than the values reported in literature of approximately $2kJ/m^2$. The lower G_{IIc} value can be explained by the curing process resulting in thermal stresses that damages the interface between the Z-pin and the laminate yielding a helical bonding structure as reported in Ref. [11]. However, in the proposed model it is assumed that the Z-pin is bonded perfectly to the laminate forming a cylindrical bond structure. Thus, the value obtained for G_{IIc} arguably reflects a weakened interface fracture toughness.

On the other hand, the variable p_0^* (same as p_0 in the empirical QS friction model) was seen to vary for each loading rate from QS up to 12m/s case. The variation in p_0^* is not physical, since it is a parameter describing residual friction prior to slip. Nonetheless, the variation can be explained by the fact that equilibrium was not reached during the debonding stage (see Chapter 4) and hence this observation could well be an inertial effect.

Based on the results obtained in tables 5.2 and 5.3 the predicted bridging response obtained from the model is presented in figs. 5.3 to 5.5.

Pull-out rate	$k_z(N/mm^2)$	$G_{IIc}(N/mm)$	$p_0^*/p_0(N/mm)$
QS	75	0.4	3.5
5m/s	300	0.8	3.3
12m/s	350	1.0	1.5

Table 5.2: Model parameters varying with loading rate

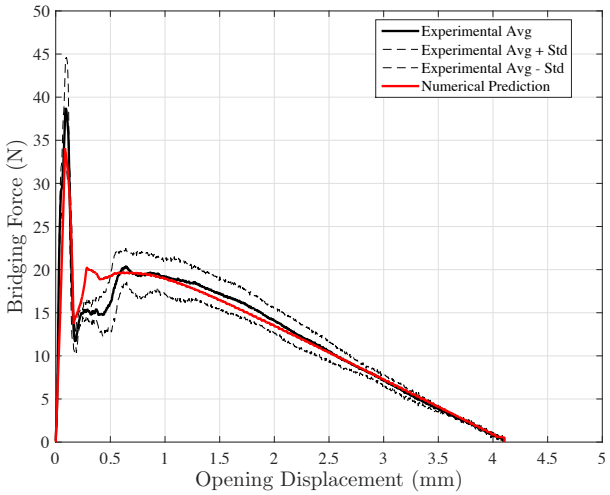


Figure 5.3: The bridging response at 5m/s obtained from the proposed peridynamic model compared to the experimental results in Ref. [12].

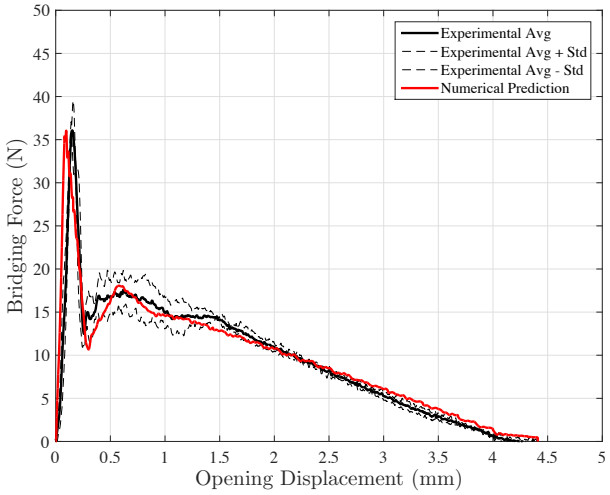


Figure 5.4: The bridging response at 12m/s obtained from the proposed peridynamic model compared to the experimental results in Ref. [12].

Pull-out rate	$A^*(N/mm)$	$B^*(N/mm)$	$l(mm)$	p_∞
QS	-	-	2.35	17.5
Dynamic	-0.1576	-0.38	0.2	-

Table 5.3: Sliding friction parameters for QS and dynamic friction models.

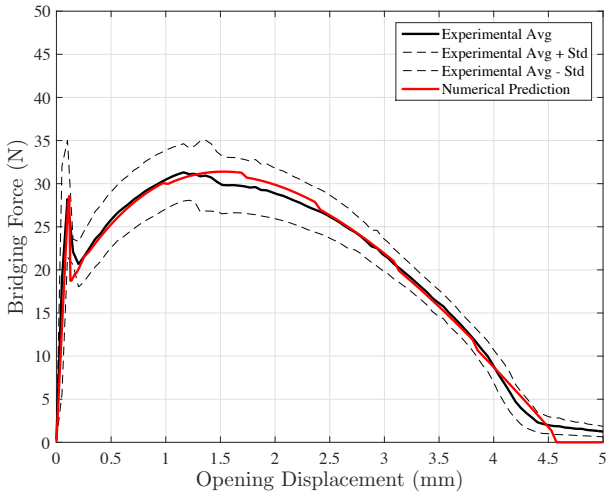


Figure 5.5: The bridging response at quasi-static loading obtained from the proposed peridynamic model compared to the experimental results in Ref. [12].

5.4.2 Model 2: Ignoring the Debonding Stage

The energy absorbed in the debonding stage is very small (about 1%) compared to that absorbed during the frictional pull-out stage. In addition, at high loading rates, dynamic equilibrium was not reached in the de-bonding phase of the experimental results (see Chapter 4) rendering the outcome obtained from modelling the de-bonding stage questionable. Therefore, it was deemed appropriate to develop a rate dependent model that ignored the debonding stage. The results obtained from the GA optimisation in this modelling approach is presented in table 5.4. It is worth noting that this approach resulted in residual friction having the same value in both QS and

Pull-out rate	$A^*(N/mm)$	$B^*(N/mm)$	$l(mm)$	$p_0^*/p_0(N/mm)$	$p_\infty(N/mm)$
QS	-	-	$0.6\dot{6}$	0.375	12.0
Dynamic	0.45	-0.55	0.1	0.375	-

Table 5.4: Sliding friction parameters for QS and dynamic friction models.

dynamic cases as would be expected i.e. $p_0 = p_0^* = 0.375$. Also, the one set of parameters is used to describe the external forces at dynamic loading rates making the model suitable for use for all dynamic loading rates unlike the previous model (where debonding was included). The bridging response obtained using results in table 5.4 is presented in figs. 5.6 to 5.8.

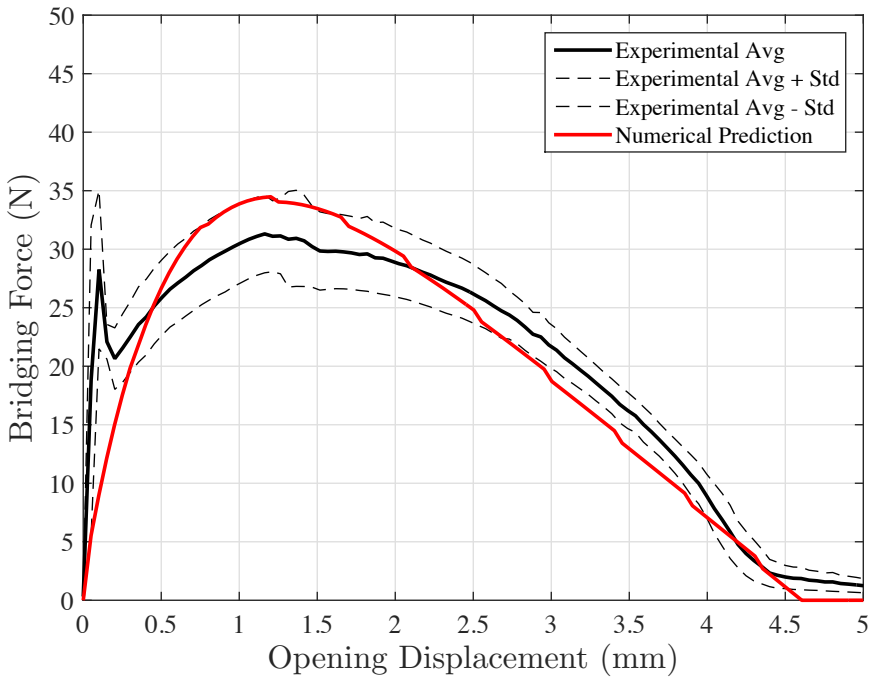


Figure 5.6: The bridging response at quasi-static loading obtained from the proposed peridynamic model compared to the experimental results in Ref. [12].

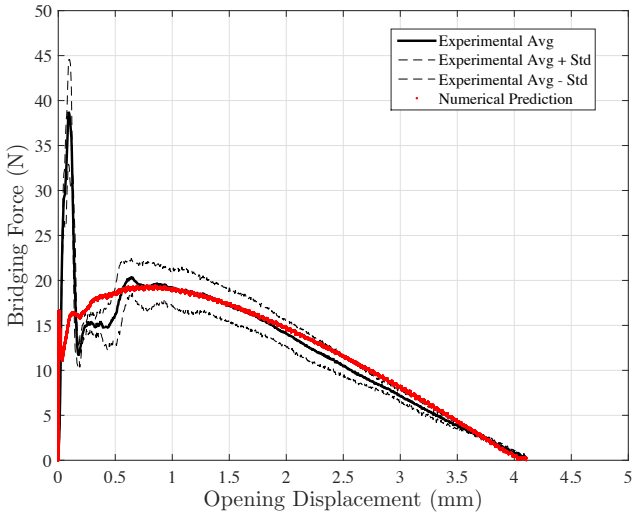


Figure 5.7: The bridging response at 5m/s obtained from the proposed peridynamic model compared to the experimental results in Ref. [12].

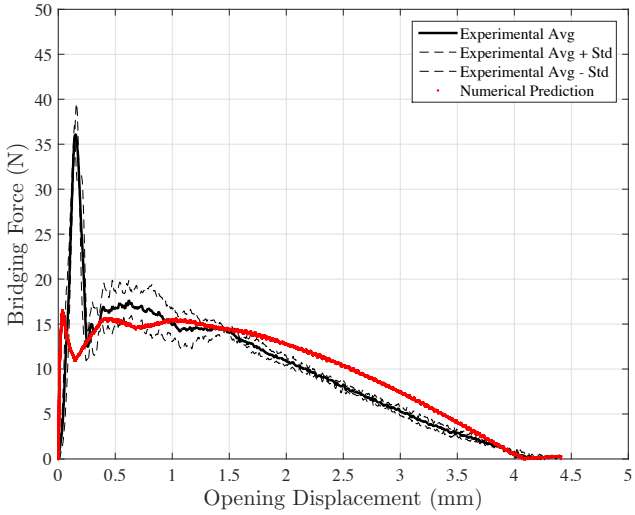


Figure 5.8: The bridging response at 12m/s obtained from the proposed peridynamic model compared to the experimental results in Ref. [12].

5.5 Discussion

The bridging response obtained by including the debonding stage is more accurate than that ignoring the debonding stage as seen in figs. 5.3 to 5.8. However, including the debonding stage three parameters k_z, G_{IIc} and p_0/p_0^* needed to be varied for each loading rate. The variation in k_z and G_{IIc} is physically feasible because they are governed by the resin which is rate dependent resulting in a rate dependent parameters. There is a lack of experimental data in the literature to be able to devise a rate dependent model for the foundation stiffness (k_z) and fracture toughness(G_{IIc}). On the other hand, the variation in the p_0/p_0^* parameter is not physical as it represent the residual friction prior to slip and by definition it is not a rate dependent parameter. Albeit, this variation can be attributed to the fact that equilibrium was not achieved during the debonding stage in the experimental results. Thus, the variation in residual friction with rate might well be a manifestation of the inertial effect. The lack of experimental data and absence of equilibrium during the debonding stage of the Z-pin pull-out response moti-

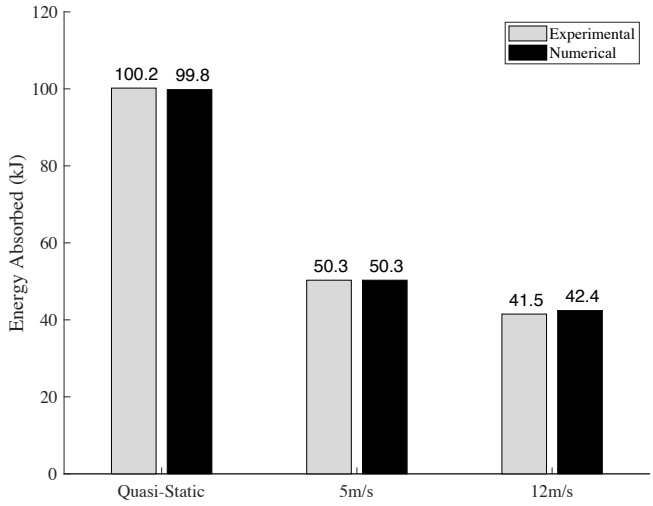


Figure 5.9: Energy dissipated by the Z-pin using model 1: Comparison between Numerical prediction and experimental results at different pull-out rates

vated the development of the model ignoring the debonding phase.

The model including the debonding stage is capable of reproducing all the key features of the experimental results: the peak force in the elastic response stage, the drop in bridging force during the debonding stage and the increase up to a peak force in the pull-out stage followed by a decrease to zero at complete Z-pin pull-out. The model ignoring the debonding stage is not able to capture the response in the debonding phase (by model definition) but captured the pull-out stage response very well. Nonetheless, the most important feature of the reduced order model is to be able to accurately predict the increase in apparent fracture toughness due to use of Z-pins. The area under the force-displacement graph is equivalent to the energy dissipated by the Z-pin and hence the increase in apparent fracture toughness. Thus it is interesting to observe whether ignoring the debonding response has any significant effect on the apparent fracture toughness.

The predicted and experimental energy dissipated by the Z-pin under

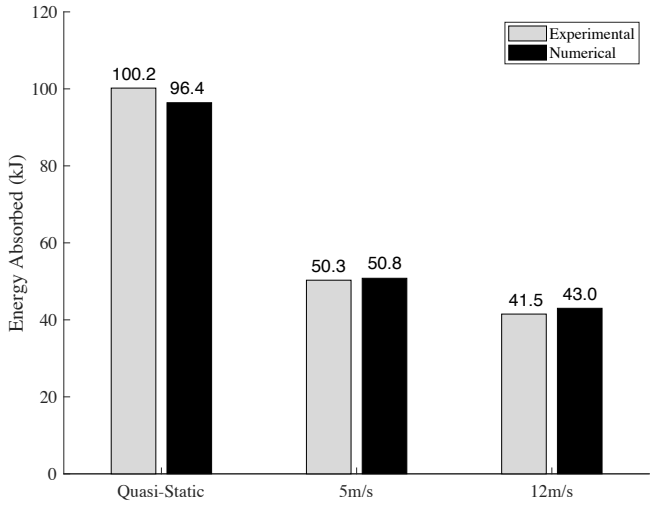


Figure 5.10: Energy dissipated by the Z-pin using model 2: Comparison between Numerical prediction and experimental results at different pull-out rates

mode I loading using both model 1 (including debonding stage) and model 2 (ignoring debonding stage) is presented in figs. 5.9 and 5.10 respectively. Both models predicted the dissipated energy with excellent accuracy as the maximum percentage error is less than 5%. The maximum percentage error in model 1 and 2 is 2.1% and 3.6%. Thus ignoring the debonding stage results in a very limited decrease in the model prediction accuracy in regards to the apparent fracture toughness. Therefore, it can be stated that ignoring the debonding stage is a sound modelling approach with insignificant impact on the modelling accuracy.

As well as yielding excellent prediction capabilities of the Z-pin bridging performance, the proposed models offer significant computational cost saving. The models proposed were run in order of minute on a desktop computer using a non-optimised Matlab code. A detailed Finite Element (FE) model to predict the bridging performance of a single Z-pin is computationally expensive taking on the order of days to run on a high performance computer with 64 cores as presented in Ref. [11]. Thus the proposed model offers several order of magnitude reduction in computational cost compared to current state of the art methods.

On large structures such as wings and fuselage were there might be thousands of Z-pins inserted, a detailed FE model would be prohibitively expensive to implement. Thus a possible alternative approach would be to utilize the proposed model in a multi-scale approach framework to predict fracture response of Z-pinned composite structures.

5.6 Summary

A reduced order model (ROM) capable of predicting the Z-pin bridging performance under pure mode I loading and subject to different loading rates is proposed. The model is based on representing the Z-pin as one dimensional peridynamic rod.

Two modelling approaches were examined in model 1 (including the debonding stage) and model 2 (ignoring the debonding stage). Mode 1 is the first ROM model capable of simulating the debonding stage of the Z-pin. In the bonded stage, the laminate reacts to relative Z-pin displacement as an elastic

foundation having stiffness k_z. Once the relative displacement exceeds a critical value based on a developed failure criterion a cylindrical mode II crack propagates along the Z-pin length. Frictional force acts on the Z-pin once it has debonded from the surrounded laminate. Ruina's state based friction model is used to model the rate dependent sliding friction response of the laminate once the debonding region exceeds the Z-pin embedded length.

Both models provide excellent prediction of the bridging force exerted by the Z-pin at the delamination interface, with better match to experimental results achieved by adopting model 1. However, it was necessary to vary the foundation stiffness (k_z), mode II fracture toughness (G_{IIc}) and residual friction (p_0/p_0^*) for each loading rate when the debonding stage was simulated in mode I. This was the case due to lack of experimental data and contamination of the experimental debonding stage results by inertial effects. Nonetheless, model 1 had shed the light on parameters that are rate dependent in the debonding region such as the foundation stiffness (k_z) and mode II fracture toughness (G_{IIc}).

On the contrary, model 2 which ignored the debonding response resulted in universal model with the same parameters used at different rates. Although this model was not able to capture the peak force in the debonding stage of the bridging response, it described the pull-out response to a high degree of accuracy. In addition, the predicted energy dissipated by model 2 is in excellent agreement with the experimental results.

Both of these models were proven to be computationally efficient (a run time of order of minute), offering significant improvement when compared to current state of the art methods utilising a high fidelity finite element models. In addition, a high degree of accuracy is achieved with less that 4% discrepancy between the numerical prediction and experimental results.

Chapter 6

Mixed Mode Z-pin Bridging Model

6.1 Introduction

The mode I model developed in the previous chapter provided a first of its kind reduced order model capable of simulating the three stages of the Z-pin bridging response. In the mode I model it was shown that neglecting the debonding stage is a sound modelling approach with negligible impact on prediction accuracy. The model proposed a validated method to describe the sliding friction behaviour of Z-pins under quasi-static (QS) and dynamic loading. Mode I is a special case of mixed mode loading where the lateral deflection of the Z-pin is zero. It is inevitable for Z-pinned laminate to experience mixed mode loading in service. This motivates the development of the mode I model to a general model capable of predicting the Z-pin bridging performance under the full range of mode mixity. This chapter is concerned with presenting a rate dependent reduced order model capable of predicting the Z-pin bridging performance across the mode mixity ranging from pure mode I to pure mode II loading.

In mixed mode loading the Z-pin will be subject to lateral deflection, rotation and axial extension. Therefore, the rod formulation is not suitable to model Z-pin bridging performance under mixed mode loading. Instead, the peridynamic beam formulation (see chapter 3) will form the basis of the mixed mode bridging model.

A Z-pin subject to mixed mode loading will experience both lateral and axial forces that reacts to the Z-pin lateral and axial deflections. A model that represents these lateral and axial forces is presented in this chapter. Mathematical modelling of these forces requires the calibration of certain model parameters. The calibrated parameters for Z-pin bridging performance is provided in this chapter.

As the mixed mode loading increases from pure mode I to pure mode II the Z-pin failure will shift from pure pull-out to pure shear fracture. A suitable failure model based on the B-K (Ref. [170]) failure criterion is developed and presented in this chapter to be able to capture the Z-pin bridging response across different mode mixties.

The model developed is then used to predict the QS and dynamic bridging performance across the mode mixity range. The deterministic nature of the model results in good prediction overall but the performance deteriorates especially in the transition region. Introducing Z-pin misalignment and strength variability into the modelling of the array response provided an excellent response across the mode mixity range including the transition region.

The result and discussion section is used to highlight the advantage of the proposed modelling approach in terms of prediction accuracy and computational cost. A summary is then presented at the end to highlight key points in this chapter.

6.2 Model Formulation

6.2.1 Problem Description

A Z-pin of length L is inserted into a composite laminate. A delamination intersects the Z-pin at a known depth, splitting the embedding laminate into a "top" and a "bottom" region of thickness L^+ and L^-, respectively. It is hereby assumed, without loss of generality, that $L^- \leq L^+$. The top sub-laminate starts moving with absolute axial and lateral speeds of $\dot{W}$ and $\dot{U}$ respectively at the time instant $t = 0$, while the bottom foundation is considered fixed (see fig. 6.1). Both sub-laminates exert axial and lateral forces on the Z-pin.

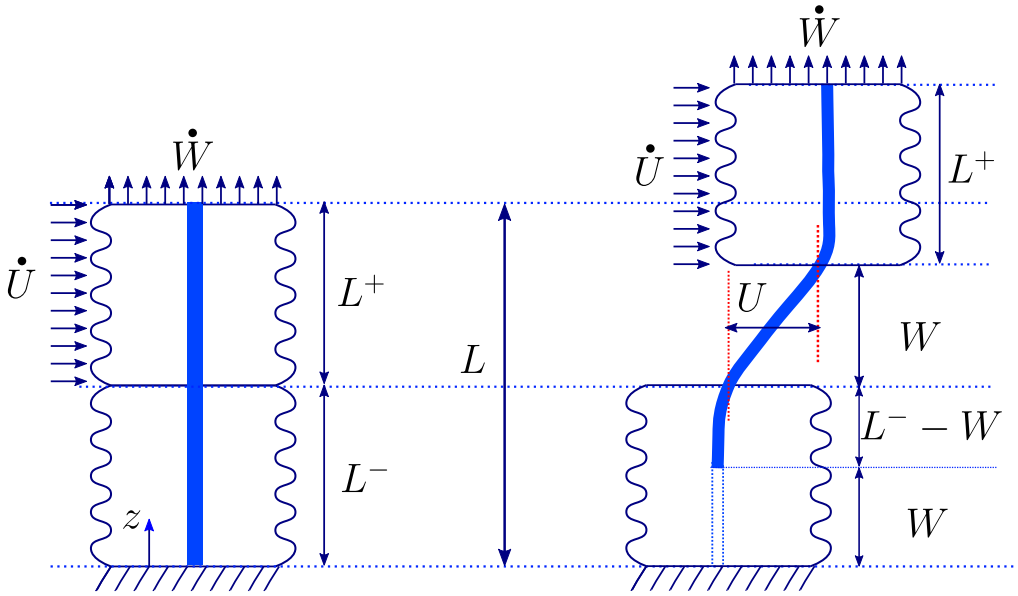


Figure 6.1: Reference undeformed (left) and deformed (right) configurations.

Consequently, the Z-pin counteracts the delamination opening displacement by exerting equilibrated bridging tractions on the interlaminar crack surfaces.

The Z-pin subject to mixed mode loading is assumed to be debonded in the current modelling approach. The bonded and progressive debonding phases are most prominent under mode I loading as discussed in chapter 4. The modelling procedure of the Z-pin under pure mode I loading in chapter 5 proved that the contribution of the bonded and debonding phases to the increase in apparent fracture toughness is very small and can be safely ignored. In addition, the residual stresses that act on the Z-pin during cure results in partial debonding of the Z-pin from the surrounding laminate (see chapter 5). Thus ignoring the debonding phase is a sound modelling approach with negligible impact on the results.

Under mixed mode loading three different forces acting on the Z-pin are here considered:

1. The "Winkler" foundation force, is a form of "punch" resistance force exerted by the laminate on the Z-pin to counteract the lateral deforma-

tion of the Z-pin. The force exerted by the laminate is proportional to the relative lateral Z-pin displacement and in opposite direction. The proportionality constant is the foundation stiffness k_x and depends on laminate stacking sequence, ply elastic constants and the Z-pin diameter and elastic properties. The Winkler foundation force has been utilised in the literature (see Refs. [98, 113, 118]).

2. The "sliding" frictional force; this includes a residual frictional term arising from the compressive thermal stress due to curing. The residual friction acts on the Z-pin in the debonded state. As the Z-pin starts sliding out of the laminate the frictional force per unit length is observed to increase with pull-out distance. The increase in frictional force can be attributed to two potential mechanisms: the interlocking of Z-pin as it is sliding out due to irregular cross section along the Z-pin length and the build up of debris along the Z-pin length (see chapter 4 for more details). The sliding friction force acts along the Z-pin length under all mixed mode loadings. However, the longer the pull-out distance the more prominent the sliding friction force. In pure mode I the Z-pin completely pull-out from the laminate making the sliding friction force a very prominent external force. In pure mode II the Z-pin fails by shear out fracture with little pull-out making the sliding friction force less prominent.

3. The "snubbing" frictional force, is an enhancement frictional term arising from the lateral punch resistance force acting on the Z-pin due to its deformation against the laminate. The presence of a lateral force acting on the Z-pin induces an enhanced axial frictional force due to Coulomb effect. The snubbing effect is a well established phenomenon as discussed in previous chapters. The snubbing frictional force acts on the Z-pin across all mode mixities. The snubbing forces increases with lateral Z-pin deformation. Under pure mode I loading where the Z-pin lateral deformation is zero the snubbing force is zero. On the other hand, the lateral Z-pin deformation is the largest under pure mode II loading resulting in high snubbing force. Nonetheless, even at low mode mixity the snubbing force remains significant and cannot be neglected.

Under pure mode I loading the Z-pin fails by complete pull-out from the embedding laminate. Under pure mode II loading the Z-pin fails by shear out fracture. Therefore, a failure criterion is needed to determine whether or not the Z-pin will fail by shear out fracture. In certain mixed mode loading range, there exist a transition region (as discussed in chapter 4) where the Z-pin can fail by either complete pull-out or by shear out fracture at random. The random nature of the Z-pin failure in the transition region is attributed to sensitivity to variability in Z-pin misalignment angle and strength. Consequently, it is necessary to take these variabilities into account when modelling the Z-pin bridging performance in the transition region as deterministic models would perform poorly.

The insertion asymmetry parameter α is defined as follows:

$$\alpha = \frac{L^-}{L^- + L^+}, \tag{6.1}$$

which implies $L^- = \alpha L$ and $L^+ = (1-\alpha)L$. Thus, in the case of symmetric insertion (i.e. $L^- = L^+$) considered in the experimental results in Chapter 4 (Ref. [12]), one finds $\alpha = 1/2$.

6.2.2 Governing Equation

The Z-pin is here described as a peridynamic beam subject to unsteady axial and lateral forces. The equilibrium equation for such a beam in bond-based peridynamics is the following (see chapter 3 for derivation):

$$\begin{aligned}
\rho A\ddot{w} + b_w\dot{w} &= \int_{z-r_h}^{z+r_h} c_a s_w dz' - \int_{z-r_h}^{z+r_h} c_s s_\gamma \bar{\theta} dz' + p(z) - q(z)u^I, \\
\rho A\ddot{u} + b_u\dot{u} &= \int_{z-r_h}^{z+r_h} c_s s_\gamma dz' + \int_{z-r_h}^{z+r_h} c_a s_w \bar{\theta} dz' + q(z) + p(z)u^I, \\
\rho I\ddot{\theta} + b_\theta\dot{\theta} &= \int_{z-r_h}^{z+r_h} c_b s_\chi dz' + \frac{1}{2}\int_{z-r_h}^{z+r_h} \left[c_s s_\gamma + c_a s_w \bar{\theta}\right](z'-z)\, dz'.
\end{aligned} \tag{6.2}$$

where, r_h is the horizon radius of the material particle located at point z; z' represents the location of particles within the horizon of z; the Z-pin

density, cross sectional area and moment of inertia are represented by ρ, A and I respectively; b_w, b_u and b_θ are the axial, shear and bending damping coefficients respectively; $\ddot{w}$ ($\dot{w}$), $\ddot{u}$ ($\dot{u}$) and $\ddot{\theta}$ ($\dot{\theta}$) are the axial, transverse and rotational acceleration (velocity) of the peridynamic particle at location z; c_a, c_s and c_b are the axial, shear and bending bond constant respectively and are defined in eq. (3.36); s_w, s_γ and s_θ are the axial, shear and bending stretches respectively as defined in eq. (3.14); $p(z)$ and $q(z)$ are the distributed axial and transverse loads acting on the Z-pin; u^I is the spatial derivative of the transverse displacement (i.e. $\frac{\partial u}{\partial z}$) which represents the slope of the Z-pin at location z.

Let the beam be divided in N segments, each having length $\Delta z = L/N$ and let it be assumed that the displacement fields ($w(z)$,$u(z)$ and $\theta(z)$) is constant within each of the segments. This leads to a "meshfree" discretization of the beam [134], whereby a peridynamic particle is located at the centre of each segment. Hence, the position of the i-th peridynamic particle is $z_i = \Delta z\left(i - \frac{1}{2}\right),\ i = 1, 2, ..., N$. The integro-differential equation in eq. (6.2) can therefore be discretised as follows:

$$\begin{aligned}
\rho A\left(\ddot{w}_i + \chi_w \dot{w}_i\right) &= I_{ij}^{(1)} + p_i - q_i u_i^I, \\
\rho A\left(\ddot{u}_i + \chi_u \dot{u}_i\right) &= I_{ij}^{(2)} + q_i + p_i u_i^I, \\
\rho I\left(\ddot{\theta}_i + \chi_\theta \dot{\theta}_i\right) &= I_{ij}^{(3)},
\end{aligned} \tag{6.3}$$

Where the I_{ij}^m entries are given in AppendixB; χ_w, χ_u and χ_θ are the axial, lateral and rotational mass-proportional viscous damping coefficients respectively.

Time integration of eq. (6.3) is conducted by using an explicit second-order centred finite difference discretisation with respect to time [134, 156]. Using a time step Δt and applying the numerical scheme to eq. (6.3), the

updated solution at the time instant $n+1$ reads:

$$
\begin{aligned}
w_i^{(n+1)} &= \frac{\frac{2\Delta t^2}{\rho A}\left[I_{ij}^{(1)} + p_i - q_i u_i^I\right]^{(n)} + 4w_i^{(n)} - (2-\chi_w\Delta t)\, w_i^{(n-1)}}{2+\chi_w\Delta t}, \\
u_i^{(n+1)} &= \frac{\frac{2\Delta t^2}{\rho A}\left[I_{ij}^{(2)} + q_i + p_i u_i^I\right]^{(n)} + 4u_i^{(n)} - (2-\chi_u\Delta t)\, u_i^{(n-1)}}{2+\chi_u\Delta t}, \\
\theta_i^{(n+1)} &= \frac{\frac{2\Delta t^2}{\rho I}\left[I_{ij}^{(3)}\right]^{(n)} + 4\theta_i^{(n)} - (2-\chi_u\Delta t)\, \theta_i^{(n-1)}}{2+\chi_\theta\Delta t}.
\end{aligned}
\tag{6.4}
$$

6.2.3 External Forces Model

Lateral Force Model

The only lateral force (q) acting on the Z-pin is the Winkler foundation force. Based on the description in section 6.2.1, it follows that the expression of the lateral force per unit length acting on the Z-pin is:

$$
q(z) = -k_x u_r(z) \tag{6.5}
$$

Where k_x is the Winkler foundation stiffness with units of N/mm^2, and $u_r(z)$ is the relative transverse displacement between the Z-pin and the surrounding laminate at location z. The minus sign is present as the force, a "punch resistance force", acts to oppose the relative displacement between the Z-pin and the laminate.

The general expression of the transverse relative displacement(u_r) and speed($\dot{u}_r$) is given by:

$$
\begin{aligned}
u_r(z) &= \left[1 - H(z-\alpha L+W)\right] u(z) + H(z-\alpha L)\left[u(z) - U\right], \\
\dot{u}_r(z) &= \left[1 - H(z-\alpha L+W)\right] \dot{u}(z) + H(z-\alpha L)\left[\dot{u}(z) - \dot{U}\right].
\end{aligned}
\tag{6.6}
$$

where, $H(x)$ for $x \in \mathbb{R}$ is the Heaviside step function, i.e. $H(x) = 1$ for $x \geq 0$ and $H(x) = 0$ for $x < 0$.

Considering the time integration scheme proposed section 6.2.2, the discretised lateral force is simply given by:

$$q_i = -k_x u_{ri} \tag{6.7}$$

where u_{ri} is the relative displacement of the peridynamic particle at location z.

Axial Force Model

The axial force acting on the Z-pin is purely a frictional force due to neglecting the bonded stage of the Z-pin response. The frictional force is divided into two components, a sliding (P_{SL}) and snubbing (P_{SN}) frictional forces each arising due to different mechanisms.

The sliding frictional force arises from:

1. The presence of residual thermal stresses acting on the Z-pin due to curing.

2. The build up of debris along the path of the Z-pin as its pulling out.

3. The interlocking between the Z-pin and surrounding laminate due to irregular Z-pin cross section as discussed in chapter 4.

The sliding frictional force acting on the Z-pin under mixed mode loading is the same as that acting under mode I loading. Consequently, the same mathematical equations as that developed in chapter 5 is used here to describe the sliding friction force and are given in eq. (6.8) and eq. (6.9) for the quasi-static and dynamic cases respectively. The meaning and definition of the variables presented in eqs. (6.8) and (6.9) is the same as that presented in chapter 5.

$$P_{SL} = p_\infty + (p_0 - p_\infty)\, e^{-W/\ell} \tag{6.8}$$

$$P_{SL}(z) = p_0^* + A^* \log\left|\frac{\dot{w}_r(z)}{V_c}\right| + \Phi(z)$$
$$\dot{\Phi}(z) = -\frac{|\dot{w}_r(z)|}{\ell}\left[\Phi(z) + B^* \log\left|\frac{\dot{w}_r(z)}{V_c}\right|\right] \tag{6.9}$$

On the other hand, the snubbing friction is an enhancement coulomb friction that arises from the lateral deflection of the Z-pin being opposed by a Winkler foundation force as presented earlier. The Winkler foundation force increases the compressive stresses acting on the Z-pin inducing an additional coulomb friction. Thus, under quasi-static loading the snubbing frictional force is given by:

$$P_{SN}(z) = \mu_{QS} q(z) \tag{6.10}$$

Under dynamic loading condition, the Ruina state-based friction model (Ref. [169]) presented in eq. (6.11) is used to describe the snubbing frictional force.

$$\tau = \sigma\left(\mu_0 + \phi_1 + A_1 \log\left|\frac{\dot{w}_r}{V_c}\right|\right),$$
$$\dot{\phi_1} = -\frac{|\dot{w}_r|}{\ell_1}\left(\phi_1 + B_1 \log\left|\frac{\dot{w}_r}{V_c}\right|\right), \tag{6.11}$$

where τ is the frictional shear stress that arises between two surfaces in contact, which slide with respect to each other with relative velocity $\dot{w}_r$; σ is the compressive contact stress between the two aforementioned surfaces. In eq. (6.11)), μ_0 denotes a reference coefficient of friction. The variable ϕ_1 is an additional coefficient of friction that tracks the "state" of the interface. The latter evolves as relative sliding with speed $\dot{w}_r$ takes place; ℓ_1 is a characteristic length scale for the interface evolution. The coefficient A_1 and B_1 are empirical constants that need to be calibrated by means of experimental data. For $|\dot{w}_r| \leq V_c$, the logarithmic terms in eq. (6.11) are set to zero, i.e. the dependency of the friction on the sliding speed is neglected. Hence, V_c is usually denoted as a "cut-off" speed.

In the context of snubbing force acting on the Z-pin, σ denotes a compressive radial stress on the TTR surface, while τ is the corresponding axial-radial frictional shear due to snubbing. The relative sliding speed in this case depends only on the axial coordinate z, i.e. $\dot{w}_r = \dot{w}_r(z)$. Hence, the resulting

snubbing frictional force per unit length (p_{SN}) can be expressed as:

$$P_{SN}(z) = \oint \tau(z,l)dl = \left(\mu_0 + \phi_1 + A_1 \log\left|\frac{\dot{w}_r}{V_c}\right|\right) \pi D \int_0^{2\pi} \sigma(z,\psi)d\psi. \quad (6.12)$$

Note that:

$$q(z) = \pi D \int_0^{2\pi} \sigma(z,\psi)d\psi. \quad (6.13)$$

Substituting eq. (6.13) into eq. (6.12) yields:

$$P_{SN}(z) = q(z)\left(\mu_0 + \phi_1 + A_1 \log\left|\frac{\dot{w}_r}{V_c}\right|\right) \quad (6.14)$$

Lets define a dynamic friction coefficient (μ_{Dyn}) as:

$$\mu_{Dyn} = \mu_0 + \phi_1 + A_1 \log\left|\frac{\dot{w}_r}{V_c}\right| \quad (6.15)$$

substituting the definition of μ_{Dyn} above into eq. (6.14) yields eq. (6.16). Comparing eq. (6.16) and eq. (6.10), it is immediately clear that the two equations are equivalent to each other. The only difference is that the coefficient of friction in dynamic loading is a variable that depends on the sliding speed and the state (ϕ_1) of the interface.

$$P_{SN}(z) = \mu_{Dyn} q(z) \quad (6.16)$$

The total axial force (P) acting on the Z-pin is obtained by adding the sliding and snubbing frictional force components, i.e. $P = P_{SL} + P_{SN}$. Therefore, the total axial force acting on the Z-pin is given by eq. (6.17) and eq. (6.18) for the quasi-static and dynamic cases respectively.

$$P(z) = p_\infty + (p_0 - p_\infty)\, e^{-W/\ell} + \mu_{QS} q(z) \quad (6.17)$$

$$P(z) = p_0^* + A^* \log\left|\frac{\dot{w}_r(z)}{V_c}\right| + \Phi(z) + \mu_{Dyn} q(z)$$

$$\dot{\Phi}(z) = -\frac{|\dot{w}_r(z)|}{\ell}\left[\Phi(z) + B^* \log\left|\frac{\dot{w}_r(z)}{V_c}\right|\right] \quad (6.18)$$

$$\dot{\phi_1}(z) = -\frac{|\dot{w}_r(z)|}{\ell_1}\left[\phi_1(z) + B_1 \log\left|\frac{\dot{w}_r(z)}{V_c}\right|\right]$$

The general expression of the relative displacement(w_r) and speed($\dot{w}_r$) is given by:

$$\begin{aligned} w_r(z) &= \left[1 - H(z - \alpha L + W)\right] w(z) + H(z - \alpha L)\left[w(z) - W\right], \\ \dot{w}_r(z) &= \left[1 - H(z - \alpha L + W)\right] \dot{w}(z) + H(z - \alpha L)\left[\dot{w}(z) - \dot{W}\right]. \end{aligned} \tag{6.19}$$

where, $H(x)$ for $x \in \mathbb{R}$ is the Heaviside step function, i.e. $H(x) = 1$ for $x \geq 0$ and $H(x) = 0$ for $x < 0$.

Considering the time-marching centred finite-difference scheme discussed in sec. 6.2.2, the discretised axial forces from eq. (6.18) read:

$$\begin{aligned} P_i^{(n)} &= \left[p_0^* + A^* \log\left|\frac{\dot{w}_{ri}^{(n)}}{V_c}\right| + \Phi_i(n)\right] + \mu_{Dyn} q_i^n \\ \Phi_i^{(n)} &= \Phi_i^{(n-2)} - 2\frac{\left|\dot{w}_{ri}^{(n-1)}\right|}{\ell}\left[\Phi_i^{(n-1)} + B^* \log\left|\frac{\dot{w}_{ri}^{(n-1)}}{V_c}\right|\right]\Delta t. \\ \phi_{1i}^{(n)} &= \phi_{1i}^{(n-2)} - 2\frac{\left|\dot{w}_{ri}^{(n-1)}\right|}{\ell_1}\left[\phi_{1i}^{(n-1)} + B_1 \log\left|\frac{\dot{w}_{ri}^{(n-1)}}{V_c}\right|\right]\Delta t. \end{aligned} \tag{6.20}$$

While, at quasi-static loading, the discretised axial force in eq. (6.17) is obtained as:

$$P_i^n = p_\infty + (p_0 - p_\infty)\, e^{\frac{-w_{ri}^n}{\ell}} + \mu_{QS} q_i \tag{6.21}$$

It is worth noting that no external forces act on the section of the Z-pin that has pulled-out from the laminate. In mathematical form this means that:

$$p_i^{(n)}, q_i^{(n)} = \begin{cases} 0 & \alpha L - W < z < \alpha L \\ p_i^{(n)}, q_i^{(n)} & otherwise \end{cases} \tag{6.22}$$

6.2.4 Failure Model

The Z-pin fails by complete pull-out failure under pure mode I loading and by shear out fracture failure under pure mode II loading. There exist a mixed mode loading region where the Z-pin fails by either pure pull-out or by fracture failure at random (see chapter 4). This region is known as the transition

region which spans the mode mixity of 0.25-0.5 as shown in the experimental results (see chapter 4). At mode mixities above 0.5 the Z-pin fails by shear out fracture with minimal pull-out from the laminate. Thus it is necessary to implement a failure criterion capable predicting whether or not fracture failure occurs in the Z-pin under any loading condition.

An energy based criterion similar to that presented by Foster et al. (Ref. [146]) is developed and implemented to predict the fracture failure of the Z-pin under mixed mode loading conditions. The total energy stored at point z along the Z-pin can be obtained by calculating the energy needed to break all the bonds across a fracture plane located at point z. Comparing the calculated total energy at location z to a critical energy the onset of failure can be determined. In order to use well established material parameters, the energy release rate is used instead of the total energy. Assuming the crack propagates instantaneously once the critical energy is reached, then the energy release rate is obtained by dividing the total energy by the Z-pin cross sectional area. The energy release rate is compared to the critical energy release rate to determine the onset of fracture.

The energy density contained in a bond is defined as (Ref. [156]):

$$E_{bond} = \frac{1}{2} c s^2 \left| z' - z \right| \tag{6.23}$$

where c and s are a general bond constant and stretch respectively, i.e. c can be replaced by c_a, c_s or c_b to represent axial, shear and bending bond constants. It is here assumed that the energy stored in a bond is fully recoverable unless failure occurs. Consider a fracture plane located at $z = z_f$ as shown in fig. 6.2, then the total energy at that location is obtained by summing the contribution of all the bonds that cross the z_f plane. Therefore, the total energy (E_{tot}) at point z is given by:

$$E_{tot} = \int_{z_f - r_h}^{z_f} \int_{z_f}^{z_f + r_h} E_{bond} \, dz' dz \tag{6.24}$$

Substituting eq. (6.23) into eq. (6.24) one obtains:

$$E_{tot} = \frac{1}{6} c s^2 r_h^3 \tag{6.25}$$

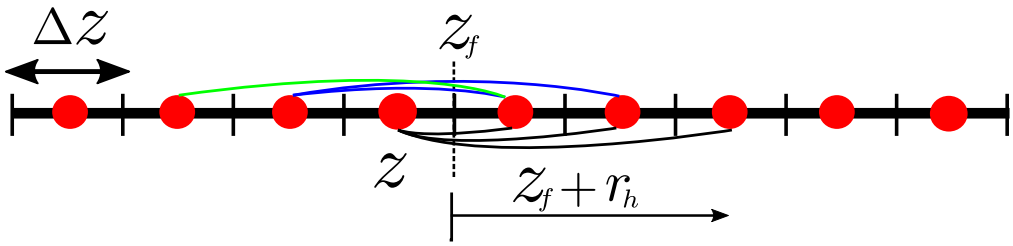


Figure 6.2: Illustration of bonds crossing a failure plane located at point z_f

The energy release rate is thus obtained by dividing the total energy at location z (E_{tot}) by the Z-pin cross sectional area (A). Using the result in eq. (6.25) and dividing by A the mode I and II energy release rates denoted as G_I and G_{II} respectively in peridynamic formulation are defined as:

$$\begin{aligned} G_I &= \frac{r_h^3}{6A} c_a s_w^2 \\ G_{II} &= \frac{r_h^3}{6A} \left[c_s s_\gamma^2 + c_b s_\theta^2 \right] \end{aligned} \tag{6.26}$$

Where c_a, c_s and c_b are the axial, shear and bending bond constants respectively as defined in eq. (3.36); s_w, s_γ and s_θ are the axial, shear and bending stretches respectively as defined in eq. (3.14).

The total energy release rate (G) at location z is the addition of the mode I and II energy release rates, i.e. $G = G_I + G_{II}$. Once the total energy release rate exceeds the critical energy release rate (G_c) the Z-pin fails. Since the Z-pin is subject to mixed mode loading, the critical energy release rate is defined using the B-K failure criterion (Ref. [170]) as given in eq. (6.27).

$$G_c(z) = G_{Ic} + (G_{IIc} - G_{Ic}) \xi^\eta(z) \tag{6.27}$$

where G_{Ic} and G_{IIc} are the mode I and II critical energy release rates of the Z-pin; ξ is the mode mixity of the Z-pin particle at location z; η is an empirical constant. The mode mixity ξ is defined as the ratio of the mode II energy release rate to the total energy release rate at location z, i.e. $\xi = G_{II}/G$. Consequently, the critical energy release rate (G_c) varies along the length of the Z-pin depending on the local mode mixity of the Z-pin at location z allowing for prediction of failure location.

6.2.5 Modelling Variability

The Z-pin response in the transition region showed great variability in failure mode as reported in chapter 4, where some Z-pins failed by complete pull-out and others by fracture failure. Each of the coupons tested had 16 Z-pins inserted in the through thickness direction. In the transition region the proportion of Z-pins failing by fracture varied between 19% and 60%. Thus the measured bridging response in the experimental results is an averaged response of the 16 Z-pins.

A deterministic model would not be able to capture such variability, resulting in less accurate results in the transition region. It is necessary to introduce variability into the reduced order model to accurately capture the response of the Z-pin in the transition region.

Two main sources of variability are the Z-pin misalignment angle and strength as mentioned in chapter 4. The variability in the misalignment angle, a consequence of the Z-pin insertion process, results in the Z-pin witnessing a different mode mixity to the nominal mode mixity. The higher the mode mixity the more prominent the punch resistance and snubbing frictional forces and the more likely the Z-pin to fail by shear fracture. On the other hand, the variability in Z-pin strength is due to the Z-pin manufacturing process producing different defects of varying sizes.

In chapter 4 it was stated that the mean deviation of the misalignment angle from the nominal value ($\beta_{nominal}$) is zero while the standard deviation is 3°. Assuming a normal distribution for the Z-pin misalignment angle (β) with the mean and standard deviation of 0° and 3° respectively, a population of 16 Z-pins is created where each Z-pin has a different misalignment angle. The misalignment angle population ($\beta_{population}$) was created in Matlab using the *normrnd* function as shown in eq. (6.28).

$$\beta_{population} = normrnd(\beta_{nominal}, 3^{\circ}, population\ size) \tag{6.28}$$

Where the population size in the above equation is 16 to reflect the number of Z-pins inserted into each coupons; note that $\beta_{population}$ is a vector with the number of elements equal to the population size. The definition of the opening (W) and lateral (U)displacements is calculated based on the total

measured experimental displacement δ and the misalignment angle (β) as:

$$\begin{aligned} W &= \delta cos(\beta^\circ) \\ U &= \delta sin(\beta^\circ) \end{aligned} \tag{6.29}$$

The Z-pin critical fracture toughness obtained in eq. (6.27) is multiplied by factor in order to model the variability in Z-pin strength. Thus the critical fracture toughness of the Z-pin is calculated as:

$$G_c(z) = (1 + \Gamma) \left[G_{Ic} + (G_{IIc} - G_{Ic}) \, \xi^\eta(z) \right] \tag{6.30}$$

where Γ is the factor introduced to alter the strength of the Z-pin; the variable G_{Ic}, G_{IIc}, ξ and η are the same as those define in eq. (6.27). The variability in Z-pin strength is assumed to follow a normal distribution with the mean value equal to nominal fracture toughness (G_c) given by eq. (6.27) obtained for the deterministic model, while the standard deviation chosen to reflect the observed variability of the Z-pin failure in the transition region. Thus the factor Γ has a mean of zero and a standard deviation of 2. The Z-pin strength population is created in Matlab using the *normrnd* function to obtain a different value for the factor Γ as shown in eq. (6.31).

$$\Gamma = normrnd(0, 2, populationsize) \tag{6.31}$$

The Z-pin bridging response model is then run 16 times each time with a Z-pin misalignment angle (β) and fracture toughness (G_c) taken from the population of misalignment angles and fracture toughness values generated using the normal distributions in eqs. (6.28) and (6.31). The bridging response is then averaged across the 16 samples and compared to the appropriate experimental results.

6.2.6 Numerical Considerations

The Z-pin is divided into 200 particles in all the simulations conducted. The number of particles (N) chosen was based on the results obtained in chapter 3 and on convergence study conducted (see fig. 5.2). Thus peridynamic particle domain size is $\Delta z = L/N$. The horizon radius is set to be equal to $r_h = 3\Delta z$ based on benchmark study conducted in Ref. [135] and the results from chapter 5.2.

To apply the boundary condition a fictitious boundary layer is added to the Z-pin in the top half of the laminate (see sec. 3.4.1). The boundary layer size is set to be equal to the horizon radius. The particles in the fictitious boundary layer are set to have opening and lateral displacement (velocity) equal to the laminate opening and lateral displacement (velocity) respectively in the case of quasi-static (dynamic) loading.

The time step size (Δt) was chosen to be equal to the stable time step size (Δt_{stable}) computed in section 5.2.4 multiplied by a safety factor of 0.9, i.e. $\Delta t = 0.9\Delta t_{stable}$. The axial ($b_w$), shear ($b_\gamma$) and bending ($b_\theta$) damping coefficients were set using trial and error to be 5×10^{-3}, 5×10^{-4} and 5×10^{-4} respectively.

6.3 Model Calibration

Model parameters need to be identified for calibrating the model, namely: the Winkler foundation stiffness k_x, the B-K failure criterion parameters G_{Ic}, G_{IIc} and the exponent η; the friction-related parameters p_0^*, A^*, B^*, ℓ, p_0, p_∞, μ_0, μ_{QS}, A_1 and B_1 which appear in eqs. (6.15), (6.17) and (6.18). Strictly speaking, also the cut-off velocity (V_c) in eq. (6.18) represents an unknown, but this have been set to $0.01mm/s$. The Choice of V_c is based on the fact that the cut-off velocity is the velocity where rate effects are not significant and can be ignored. Quasi-static (QS) loading rate is the logical choice where rate effects are not significant. Hence, $V_c = 0.01$ is chosen as it represents the speed at which QS tests are conducted.

The bridging traction force applied by the Z-pin as a function of the lateral and opening displacements is the main output of interest from the model. The experimental bridging traction response presented in chapter 4 is the total force applied by the Z-pin i.e. it is the resultant of the Z-pin shear and axial applied forces. The expression of the peridynamic shear (f_{shear}) and axial (f_{axial}) forces at an arbitrary location z^* on the rod is derived in Appendix C. Considering that the bridging traction is applied at the mid-plane between the top and bottom laminates i.e. $z^* = \alpha L$, and using the formulas developed in Appendix C, the bridging force (P) obtained from the model is given by:

$$P = \sqrt{f_{axial}^2 + f_{shear}^2} \tag{6.32}$$

The model parameters are then obtained by calibrating the model traction force against a subset of the experimental results. The calibrated model is then tested against the rest of the experimental results as a proof of validity. The subset of experimental results used for calibration is T1 tests of the 0°, 9° and 75° (representing mode II loading) mixed mode angles for the quasi-static and dynamic cases. Thus, the model is here calibrated by using genetic algorithm to minimise the cost function (C) given in eq. (6.33).

$$\begin{aligned} C_1 &= \sum_{k=1}^{Q} \left[P_k - P_k^{(e)} \right]^2_{T1@0^\circ} \\ C_2 &= \sum_{k=1}^{Q} \left[P_k - P_k^{(e)} \right]^2_{T1@9^\circ} \\ C_3 &= \sum_{k=1}^{Q} \left[P_k - P_k^{(e)} \right]^2_{T1@75^\circ} \\ C &= \sqrt{C_1^2 + C_2^2 + C_3^2}\Big|_{QS\ and\ Dynamic} \end{aligned} \tag{6.33}$$

where $P_k^{(e)}$ represents the experimental observation of the bridging traction at the k-th time instant, while P_k is the corresponding axial force obtained from the time-marching simulations via eq. (6.32); Q is the total number of time steps. The subscript on the right square bracket in eq. (6.33) means that the model calibration is carried out using T1 experimental data at mixed mode angles of 0°, 9° and 75° for the quasi-static and dynamic loading rates.

The rational for adopting the cost function in eq. (6.33) is as follows:

- Under pure mode II loading (represented by 75° nominal angle), punch resistance force is the largest but the pull-out of the Z-pin from the laminate is zero. Thus, this loading case is best to calibrate the punch resistance parameters and snubbing but cannot be used for the sliding friction parameters. Also, the Z-pin fails by fracture and so can help to calibrate the B-K criterion parameters.

- Under pure mode I loading, the sliding friction is prominent but the

punch resistance and snubbing friction force is zero. Thus, this loading case is best to calibrate the sliding friction parameters.

- Under mixed mode loading all of the above described forces are at interplay. It is important to use this case to obtain a set of parameters that can describe the interaction between the sliding, snubbing and punch resistance forces. The other experimental data in the mixed mode loading regions are either in transition region where there is uncertainty in the Z-pin failure mode or failing by pure fracture only (already captured using the mode II loading).

6.4 Results and Discussions

The Z-pin geometric and mechanical properties are defined in Table 6.1. L, D, E, ρ and α are respectively the Z-pin length, diameter, Young's Modulus, density and insertion asymmetry.

E(GPa)	ρ(kg/mm^3)	L(mm)	D(mm)	α
115	1.6E-6	8	0.28	0.5

Table 6.1: Mechanical and physical properties of a T300/BMI Z-pin [12].

The genetic algorithm optimisation conducted have yielded the results shown in tables 6.2 to 6.4. As evident in table 6.2, the B-K failure criterion parameters are the same for both quasi-static and dynamic loading cases indicating that the fracture failure is not rate dependent. The rate insensitivity of fracture failure is observed in the experimental results presented in chapter 4. The fracture failure rate insensitivity is explained by the fact that the Z-pin failure is dominated by the fibre failure which themselves are rate insensitive as reported in literature (Ref. [168]). In terms of the values, Pinho et al (Ref. [171]) reported that the tensile fracture toughness (G_{Ic}) of T300/epoxy is in the range of 130-150N/mm. Hence, the calibrated value obtained here lies in the same range as that reported in literature. The shear fracture toughness (G_{IIc}) of carbon fibres are more difficult to measure experimentally but the work conducted by Laffan (Ref. [172]) indicates that G_{IIc} lies in the range of 10-15N/mm. Thus the calibrated value of G_{IIc} in

$G_{Ic}(N/mm)$	$G_{IIc}(N/mm)$	η
130	11.25	1

Table 6.2: B-K failure criterion parameters for both dynamic and quasi-static loading.

Pull-out rate	$A^*(N/mm)$	$B^*(N/mm)$	$l(mm)$	$p_0^*/p_0(N/mm)$	$p_\infty(N/mm)$
QS	-	-	$0.\dot{6}$	0.375	9.5
Dynamic	0.0281	-0.60	0.011	0.375	-

Table 6.3: Sliding friction parameters for QS and dynamic friction models.

table 6.2 of 11.25N/mm lies within the experimental range. Therefore, it can be said that the calibrated B-K failure criterion parameters are physically based and realistic.

The sliding friction parameters reported in table 6.3 have changed from the values obtained in chapter 5 where the Z-pin was subject to pure mode I loading. This is attributed to the presence of snubbing friction which is not present under pure mode I loading i.e. the total axial friction force is due to the interplay between sliding and snubbing friction. A simple way to highlight the significance of snubbing friction is to compare the value of p_∞ in table 6.3 (9.5N/mm) to that obtained in chapter 5 (12N/mm). At low mixed mode angle of 9° the snubbing friction contributes at least 20% of the total axial friction acting on the Z-pin. Similar to the result in chapter 5, it is interesting to note that the value of the residual/static sliding friction parameter (p_0^*/p_0) is the same for both quasi-static and dynamic loading. This is due to the definition of p_0^*/p_0 as being the residual friction acting on the Z-pin prior to any sliding.

The snubbing friction parameters are reported in table 6.4. The Winkler foundation stiffness (k_x) value is the same for both quasi-static and dynamic loading indicating that the punch resistance force is rate insensitive. This is a realistic outcome given that the Z-pin is embedded in quasi-isotropic laminate i.e. the Z-pin is surrounded by fibres along the whole circumference

Pull-out rate	$A_1(N/mm)$	$B_1(N/mm)$	$l_1(mm)$	$\mu_0/\mu_{QS}(N/mm)$	$k_x(N/mm^2)$
QS	-	-	-	0.285	3654.3
Dynamic	6e-4	-6e-4	0.0136	0.285	3654.3

Table 6.4: Lateral force and snubbing friction parameters for QS and dynamic friction models.

of the Z-pin. Hence, as the Z-pin is laterally deforming, it is mainly pushing against the fibres in the surrounding laminate which are rate insensitive as established earlier. However, it is believed that this outcome might not hold for a Z-pin embedded in a uni-directional laminate particularly if the Z-pin deforms against the resin rich eyelet instead of deforming against the fibres of the laminate. The static friction coefficient (μ_0/μ_{QS}) is the same for both quasi-static and dynamic friction coefficients as would be expected from its definition (the friction coefficient prior to sliding).

6.4.1 Deterministic Model Results

The predicted bridging response of the Z-pin under quasi-static and dynamic loading using the parameters obtained in tables 6.2 to 6.4 is presented in figs. 6.3 to 6.6. Overall the reduced order model is shown to be capable of accurately describing the bridging force exerted by the Z-pin at different loading rates and mixed mode loading. However, in the transition region corresponding to a nominal mixed mode angles of 15° and 30° the performance of the model deteriorates noticeably. The deterioration in the transition region is attributed to the deterministic nature of the model and the fact that the experimental results are an average of 16 Z-pins. The bridging response varies in the transition region due to variability in misalignment angle and strength. Thus, with an experimental coupon having 16 Z-pins each Z-pin produces different bridging response and fails at different point. Taking into account the variability in Z-pin response improves the performance in the transition region as seen in section 6.4.2.

For the quasi-static loading, it is observed that for the nominal mixed mode angle of 0° the predicted force continuously decrease to zero past the peak force as the opening displacement increases closely matching the ex-

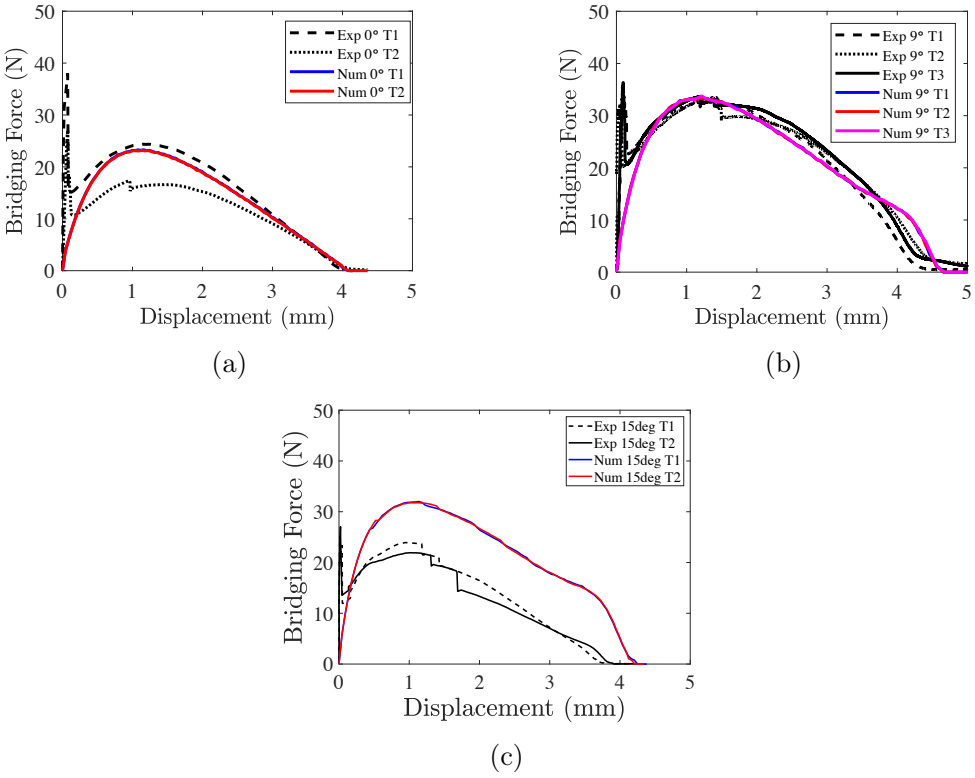


Figure 6.3: The experimental and numerical bridging response under quasi static loading for a nominal mixed mode angle of (a) 0°, (b) 9° and (c) 15°.

perimental results. Similar observation is seen for the nominal mixed mode angle of 9° and 15° but with slight change in slope close to the end as seen in figs. 6.3b and 6.3c. This change in slope is due to the large snubbing friction force being removed as the Z-pin pulls-out from the laminate. This observation is clearly seen in the experimental results of the T2 test of the nominal mixed mode angle of 15° (see fig. 6.3c) albeit less pronounced due to the fact that few Z-pins have survived up to this opening displacement in the experimental results.

The numerical prediction for the nominal mixed mode angle of 30° (see fig. 6.4a) is distinctly different from the observed experimental response as it predicts the Z-pin failing at low displacement compared to experimental

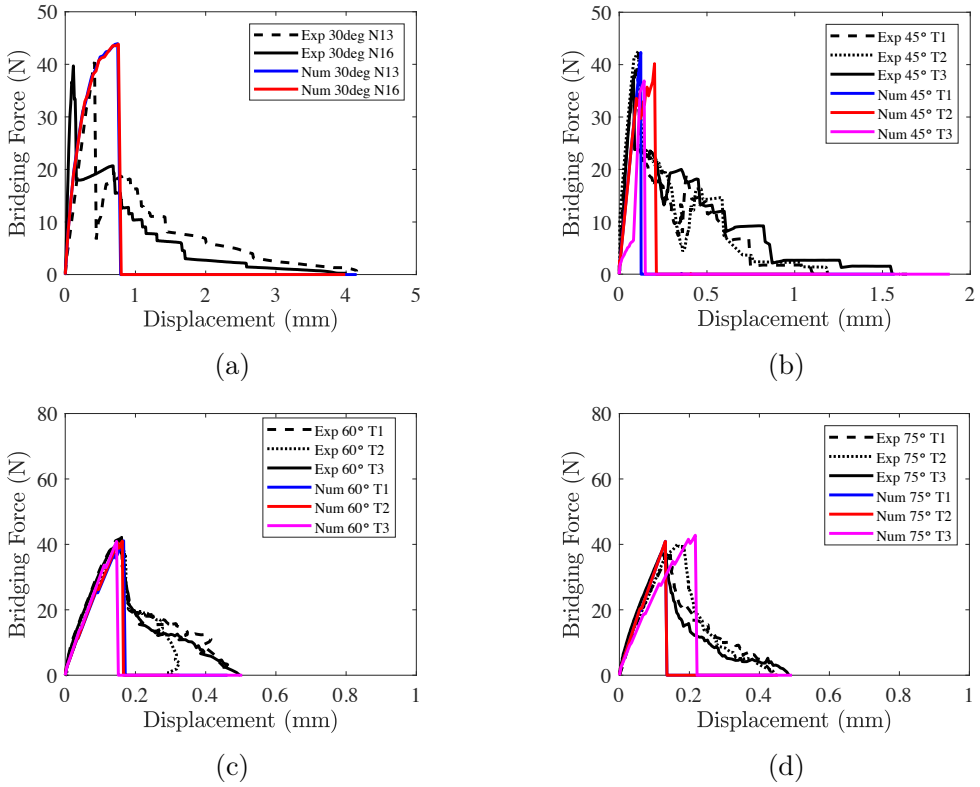


Figure 6.4: The experimental and numerical bridging response under quasi static loading for a nominal mixed mode angle of (a) 30°, (b) 45°, (c) 60° and (e) 75°.

results. This is attributed to the deterministic nature of the model that is not capturing the variability arising from the misalignment angle and strength present in experimental results. The experimental observation of the samples tested under quasi-static loading with nominal mixed mode angle of 30° had between 1-2 Z-pins pulling out and not fracturing. Consequently, resulting in a small bridging force being recorded up to complete pull-out. The incorporation of variability significantly improved bridging response prediction capability as seen in section 6.4.2.

For higher nominal mixed mode angles, the numerical model predicts failure to occur instantaneously once the failure criterion is reached. For

the nominal mixed mode angles of 60° and 75° (see figs. 6.4c and 6.4d) the experimental results shows a sharp initial drop accurately matched by the numerical model failure location. However, the experimental results then slowly decreases to zero which inaccurately suggest that the Z-pin continues to provide a supporting bridging force. The carbon fibre based Z-pin is brittle and so cannot support any load past failure point, the observed experimental force is attributed to inertial effect (see chapter 4) and potentially the fractured Z-pin scratching against the laminate and hence the observed experimental result. Thus it can be said that the model is accurately able to capture the Z-pin failure response. Similar observation applies to the nominal mixed mode angle of 45° but it is interesting to note the numerical prediction and experimental response of the T3 test. In the T3 test of the nominal mixed mode angle 45° the experimentally measured mode mixity is observed to start from a low value below the transition region (see fig. 4.14c). The numerical prediction of the bridging force accurately reflects the response of the provided mixed mode loading profile by predicting a bridging force initially lower than the T1 and T2 tests which initially starts with high mode mixity (see fig. 4.14c). Therefore, it is suspected that the provided mode mixity profile for T3 is incorrect while the numerical prediction of the model being able to physically reflect the mode mixity profile input provides confidence in the model prediction capability.

For the dynamic loading, it is observed that numerical prediction for the nominal mixed mode angle of 0° (see fig. 6.5a) closely matches the experimental results albeit reaching lower peak values when compared to quasi-static loading; thus proving model ability to predict rate effect. The ability to predict rate dependent bridging performance is clearly observed in the numerical prediction of the nominal mixed mode angle of 9° which were subject to a different loading rate of approximtely 5m/s and 12m/s as shown in figs. 6.5b and 6.5c respectively. The lower the loading rate the higher the predicted bridging force i.e. accurately capturing the rate effect observed experimentally. In addition, in chapter 4 it was pointed out that experimental T2 result for the nominal mixed mode angle and loading rate of 9° and 12m/s respectively does not match the trend of increased loading rate resulting in lower Z-pin bridging force. This observation was rather attributed to inertial effect and variation in misalignment angle. However, the deterministic numerical model excluding the effect of the misalignment angle was able to predict the rate effect as shown in fig. 6.5c. The Z-pin bridging response predicted for

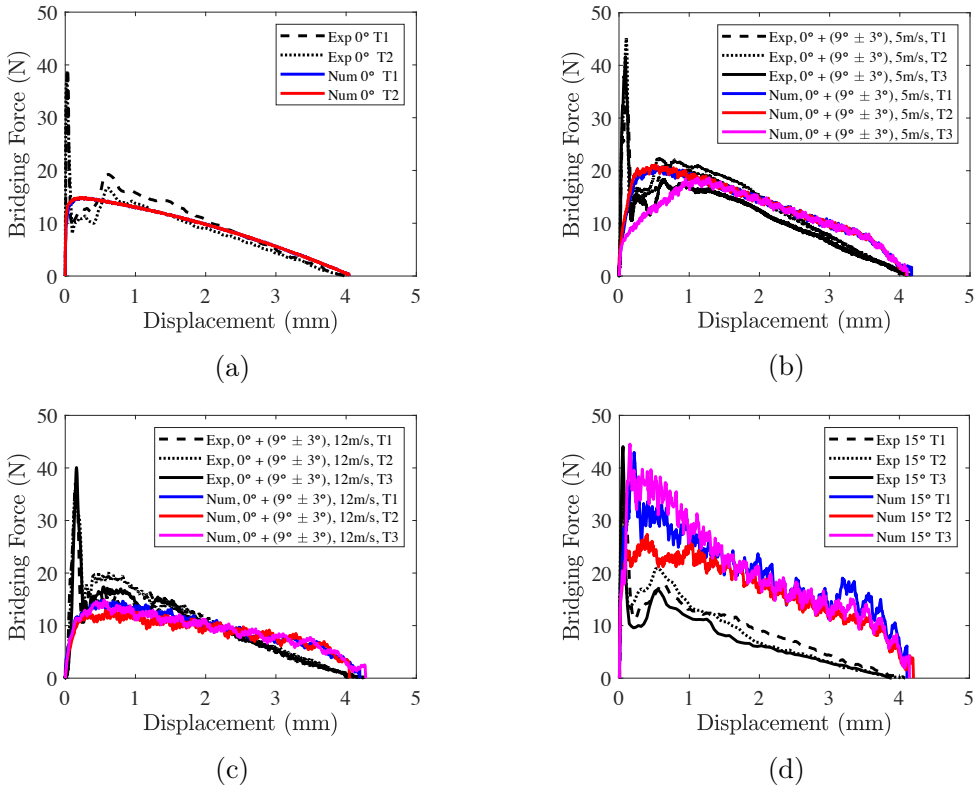


Figure 6.5: The experimental and numerical bridging response under dynamic loading for a nominal mixed mode angle of (a) 0°, (b) 9° with 5m/s rate, (c) 9° with 12m/s rate and (e) 15°.

the T2 test in fig. 6.5c is slightly lower than the T1 and T3 tests subject to the same loading rate and mode mixity. This provides further confidence in the model being able to capture key behaviour such as rate dependent Z-pin bridging performance.

The dynamic bridging response of the deterministic model in the transition region does not accurately describe the observed experimental response due to the sensitivity to the variability in misalignment angle and strength discussed earlier. Nonetheless, it was presented in the chapter 4 that the mode mixity starts from a value close to mode II and then drops to the nominal value for the mixed mode angle of 15° and 30°. This is clearly reflected

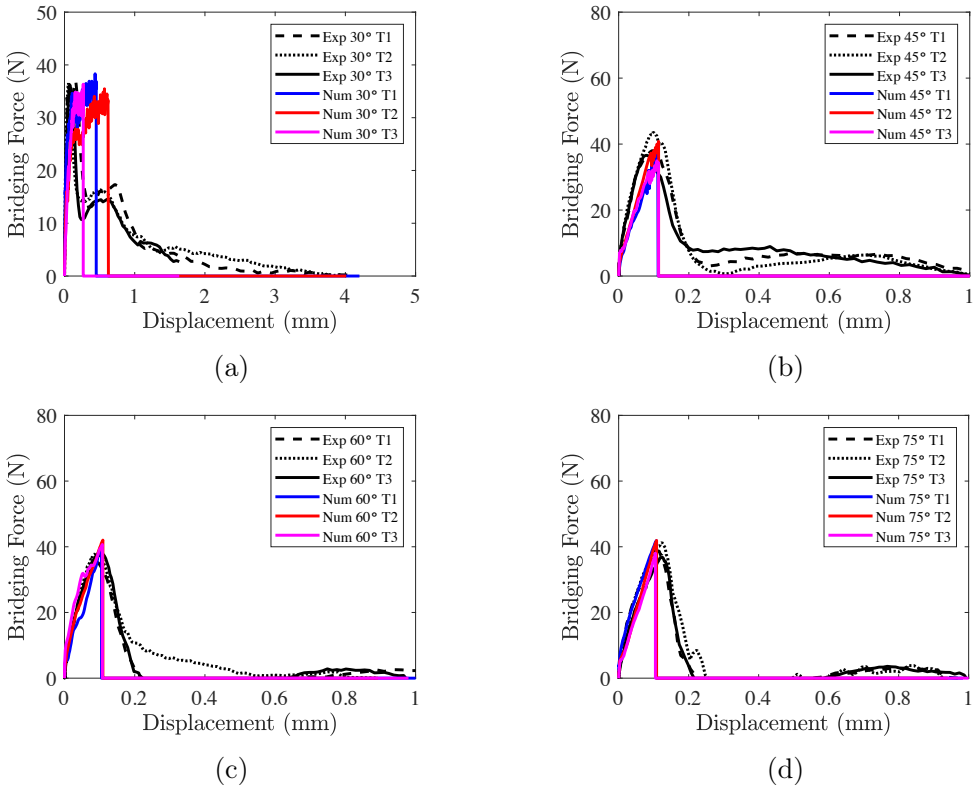


Figure 6.6: The experimental and numerical bridging response under dynamic loading for a nominal mixed mode angle of (a) 30°, (b) 45°, (c) 60° and (e) 75°.

in the numerical model predicting high force values with high slope similar to that observed in mode II and then dropping down to lower values corresponding to nominal mixed mode values as shown in fig. 6.5d. This demonstrates that the model is physically based and able to capture the mixed mode response of the Z-pin.

The dynamic bridging response beyond the transition region closely matches the experimental results as seen in figs. 6.6b to 6.6d. The numerical model predicts instantaneous failure which reflects the brittle nature of the T300/BMI Z-pin. The experimental results shows a sharp but not instantaneous drop in the bridging response which could be due to inertial effects or an array

effect. The array effect means that the 16 Z-pins failing in close proximity to one another but not at the same time. The Z-pins failing in close proximity to one another means that the difference in apparent fracture toughness between the numerical prediction and experimental value is insignificant.

6.4.2 Transition Region Non-Deterministic Model Results

The response in the transition region is seen to be sensitive to the misalignment angle and Z-pin strength. To illustrate this point, lets consider the deterministic model for the nominal mixed mode angle of 15° at the nominal value and with a small misalignment angle that corresponds to a mixed mode angle of 10°, 18° and 24° without altering any other input to the model. The result from running the model is presented in fig. 6.7. The misalignment sensitivity study shows a large variation is Z-pin response for a small variation in misalignment angle. For example, a small misalignment angle of +3° results in the Z-pin behaviour changing from complete pull-out to a fracture failure at significantly lower displacement (see fig. 6.7). At the lower misalignment angle of -5° the Z-pin fails by complete pull-out but with a much lower bridging force as a function of opening displacement compared to nominal mixed mode angle (see fig. 6.7). This clearly demonstrate the sensitivity of the misalignment angle.

On the other hand, the effect of variability in strength on the Z-pin bridging response is clearly illustrated in fig. 6.8. A 20% reduction in strength changes the failure mode from pull-out to fracture at a noticeably lower displacement. The aforementioned illustration motivates the incorporation of variability into the model in the transition region.

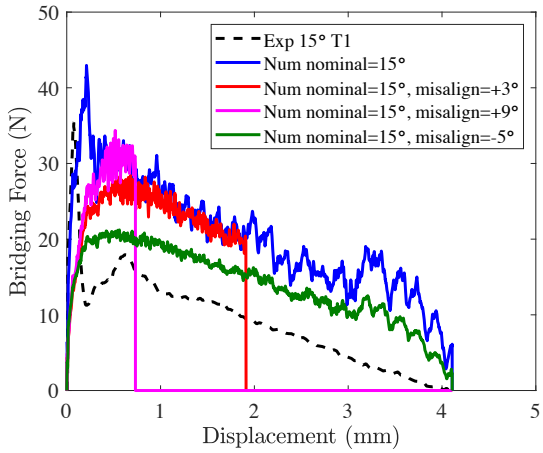


Figure 6.7: The effect of misalignment angle on the Z-pin bridging response for a nominal mixed mode angle of 15°.

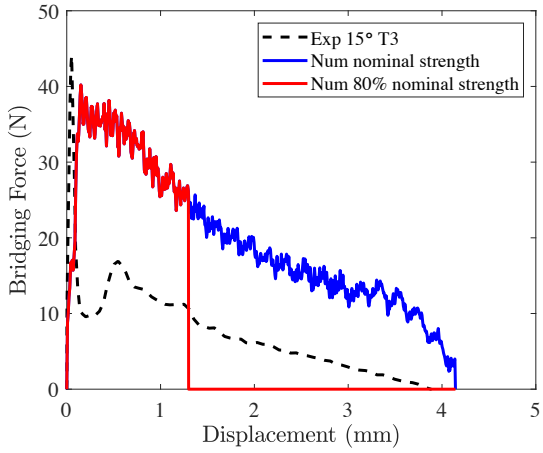


Figure 6.8: The effect of variability in Z-pin strength on Z-pin bridging response for a nominal mixed mode angle of 15°.

The misalignment angle and strength variability are incorporated into the model as described in section 6.2.5. The Z-pin bridging response in the transition region for both quasi-static and dynamic loading rates is presented in fig. 6.9. The incorporation of the variability results in a significantly better prediction of the Z-pin bridging response in the transition region. Further-

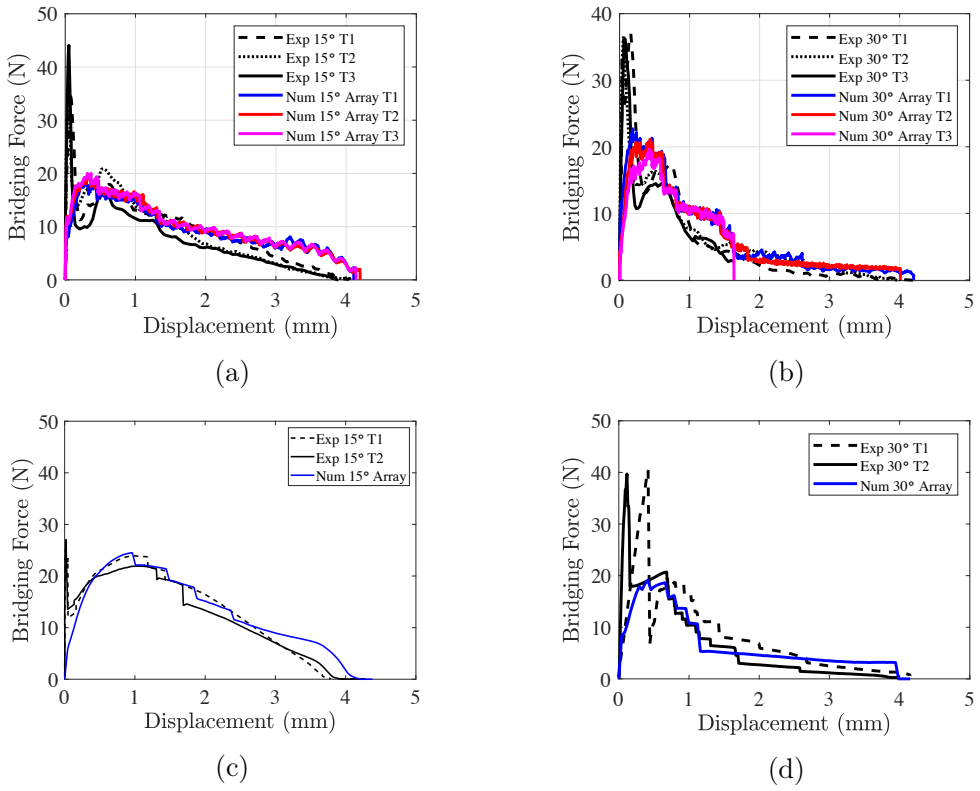


Figure 6.9: The numerical model prediction when including variability compared to experimental results. (a) and (b) correspond to nominal mixed mode angle of 15° and 30° and are under dynamic loading. (c) and (d) correspond to nominal mixed mode angle of 15° and 30° and are under QS loading.

more, this result improves our understanding of the experimental results highlighting the experimental procedure deficiency in capturing individual Z-pin response particularly in the transition region. Also, the numerical prediction makes it clear that the "stair casing" response evident under quasi static loading is due to Z-pins fracturing i.e. each stair case correspond to either 1 or more Z-pins failing depending of the drop size. It is worth noting that the numerical prediction was run for each test under dynamic loading because of the slightly different velocity profile of each test. However, under quasi-static loading only one numerical prediction is presented because both test are conducted in a controlled manner under the same velocity profile.

6.4.3 Energy Dissipation

The most important measure of Z-pin performance is the increase in apparent fracture toughness, i.e. the energy dissipated by the Z-pins. A summary of the energy dissipated by the Z-pin across all nominal mixed mode angles is presented in figs. 6.10 and 6.11 for the dynamic and quasi-static loading rates respectively. It is clear that for both quasi-static and dynamic loading rate the deterministic model gives excellent prediction of the energy dissipated by the Z-pin outside the transition region. In the transition region the prediction is poor for the reasons mentioned previously. This causes the deterministic model to fall short of being able to capture the energy dissipation trend as a function of nominal mixed mode angle. However, once the variability of the response in the transition region is implemented, the model results for both quasi-static and dynamic loading rate provide excellent prediction as a function of nominal mixed mode angle as shown in figs. 6.10 and 6.11.

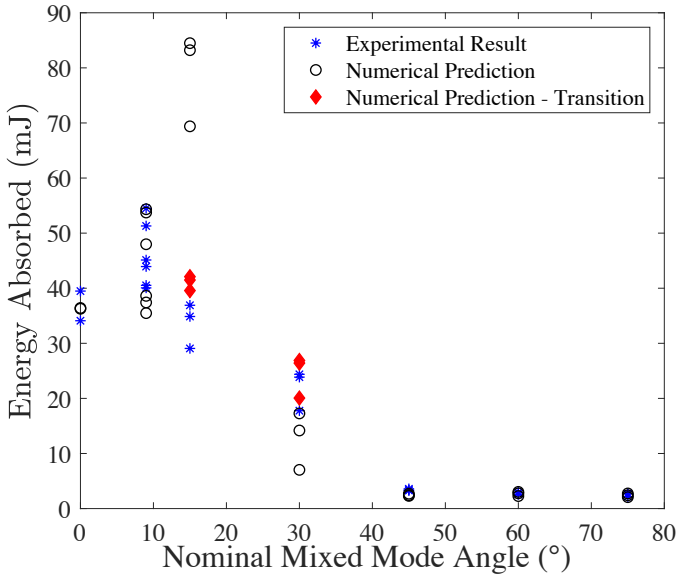


Figure 6.10: A comparison of predicted and experimental energy dissipated by Z-pin at different nominal mixed mode angles under dynamic loading.

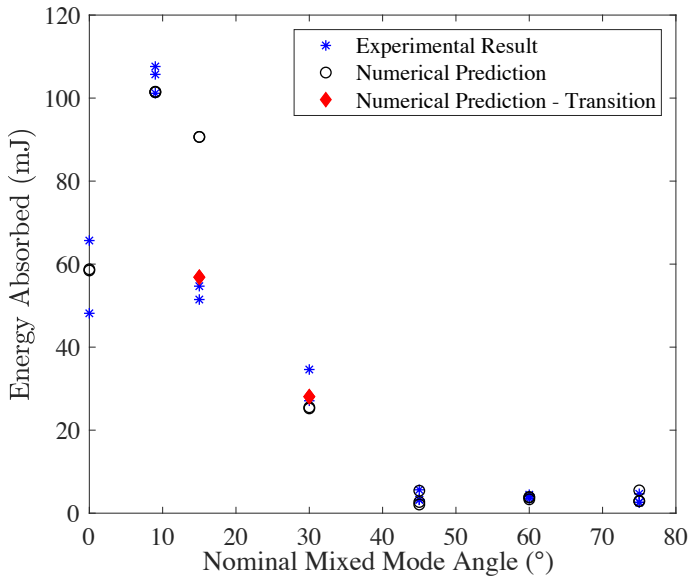


Figure 6.11: A comparison of predicted and experimental energy dissipated by Z-pin at different nominal mixed mode angles under quasi-static loading.

The Energy dissipated under pure mode I is mainly due to friction as discussed in chapter 5. As the nominal mixed mode angle increases the Z-pin deforms laterally against the laminate which is counteracted by a Winkler foundation force. The lateral deformation induces snubbing friction to act on the Z-pin in addition to the sliding friction forces. Thus causing an increase in apparent fracture toughness. However, in the transition region some Z-pins fail by fracture while others slides causing the observed reduction in absorbed energy. This was evident from observation of Z-pin samples but is conclusively proved by comparing the outcome of the deterministic and non-deterministic models. Beyond the transition region the dissipated energy falls sharply as all the Z-pins fracture at relatively low displacements due to the brittleness of the Carbon based Z-pins.

In order to improve the energy dissipation of the Z-pins across all mode mixities for a carbon based Z-pin, it is necessary to delay fracture failure as much as possible. It is thought that fracture can be delayed by having

more defects in the Z-pin which causes the Z-pin to split prior to fracture failure. The Z-pin splitting reduces stiffness allowing the Z-pin to behave in a more ductile fashion. Alternatively, using metal Z-pins which are significantly more ductile than their Carbon based counterpart could be an option for loading at higher mode mixities.

6.4.4 Model Run Time

The developed reduced order model provides excellent prediction of the Z-pin bridging performance as presented in the previous section. Additionally, the computational cost of this model is significantly lower than state of the art models using finite element approach.

The model was coded in Matlab and run on a desktop computer. The maximum run time under dynamic loading occurred where the Z-pin failed by complete pull-out as would be expected. The maximum run time under dynamic loading was 290s i.e. of the order of minutes. On the other hand, the maximum run time under quasi-static loading is 3000s i.e. of the order of tens of minutes. The reason that the quasi-static runtime is longer than the dynamic one is attributed to the use of adaptive dynamic relaxation to solve the inherently dynamic formulation of the peridynamic theory. The adaptive dynamic relaxation means that for each time steps there will be many iteration to reach the steady state solution resulting in an increase in computational cost.

Current state of the art model using finite element approach of a single Z-pin inserted in a $10 \times 10cm$ laminate is presented in Ref. [11]. The run time for such a model is 4 days on a supercomputer utilising 64 cores. Thus, considering the maximum run of tens of minutes on a desktop computer, the proposed model computational cost is still significantly cheaper than other available methods with several orders of magnitude reduction in run time. Note that the proposed model and the one provided in literature were run on machines with considerably different computational performance abilities. Thus, the computational cost reduction using the proposed approach becomes more evident.

In addition, taking into account that Matlab is a "heavy environment"

(meaning less computationally efficient than other coding environments) and that the code has not been optimised for computational efficiency, it becomes clear that the computational cost of the proposed approach can be further reduced significantly. For example, it is believed that the maximum run time cost can be reduced to order of seconds (if not split second) by:

- writing the same code in another environment such as Fortran
- parallelising the code in the spatial domain

The need for an accurate and computationally efficient reduced order model becomes clear when considering that modelling the variability in the transition region required running 16 different Z-pin models with a different combination of misalignment angle and Z-pin strength. In the dynamic case, 16 different Z-pin models were run in under an hour without utilising parallel processing. The code can be easily parallelised so that different cores solve for different Z-pin model inputs.

Based on the obtained results and the aforementioned discussion, it is apparent that the proposed reduced order model is both accurate and computationally efficient.

6.5 Summary

A rate dependent reduced order model capable of predicting Z-pin bridging performance under mixed mode loading is developed. The developed model is based on representing the Z-pin as a peridynamic beam using the formulation presented in chapter 3. Three key forces act on the Z-pin as it deforms in the laminate. These are divided into axial and lateral forces. The lateral force is modelled as a "Winkler" foundation force while the axial force is a frictional force. The axial frictional force is further split into two component: a sliding friction force and a snubbing frictional force. The frictional forces were modelled using Ruina's state based friction model. The external forces acting on the Z-pin causes it to fail.

The Z-pin fails by either complete pull-out or fracture as seen in chapter 4. Therefore, B-K failure criterion is used to predict fracture failure. For

this reason, a peridynamic based energy release rate has been proposed. The developed reduced order model had many unknown parameters. These unknown parameters were obtained by calibrating the numerical results against experimental results using genetic algorithm optimisation. However, the calibration was only done using a subset of the experimental results.

The calibrated model parameters were then used to predict Z-pin bridging performance at different loading rates and mode mixities. The model prediction was excellent at different rates and mode mixities except in the transition region. The poor performance in the transition region is attributed to the deterministic nature of the model. In the transition region the Z-pin fails by either pull-out or fracture. This variability in Z-pin response is attributed to variability in Z-pin misalignment angle and strength. Once the variability is incorporated into the model, the predicted Z-pin bridging response in the transition region is significantly improved.

The developed model provides relatively accurate bridging response prediction while being highly computationally efficient, outperforming other state of the art model presented in literature.

Chapter 7

Conclusion and Future Work

7.1 Summary

7.1.1 Thesis Motivation

Literature review showed that current state-of-the-art models of Z-pins using finite element approach are extremely expensive. Reduced-order models are a cheaper alternative to predict the Z-pin bridging performance. However, the literature is devoid from reduced order models capable of describing Z-pin bridging performance across the full span of mode-mixity loading and under high deformation rates. Therefore, the objective of this thesis was to develop such a model to fill the aforementioned knowledge gap.

7.1.2 Peridynamic Formulation and Validation

A Peridynamic approach to elasto-dynamics has been used as the basis of the reduced-order model. The rod and non-linear beam elements have been developed using such peridynamic approach. The developed models were validated against benchmark problems. It is worth noting that the geometrically non-linear peridynamic Timoshenko beam developed in this thesis is the first of its kind.

7.1.3 Experimental Results

The peridynamic Z-pin model was calibrated and validated against experimental results obtained from Ref. [12, 13]. However, the results presented in chapter 4 were analysed from a different perspective to that presented in Ref. [12, 13], highlighting the following key points:

- Constant mode-mixity was not achieved during the entirety of the tests. At lower mode-mixity values, i.e. below a nominal loading angle of 30°, the experimental mode-mixity converged to the nominal desired value prior to Z-pin failure and within a reasonable time. At higher mode-mixity values, when the nominal loading angle (β) exceeded 45°, the Z-pin failed before the mode-mixity converged to the nominal value. Consequently, the Z-pin in the range $\beta \geq 45°$ mainly failed under a mode-mixity close to pure mode II loading.

- The use of brass sleeve in the test set-up contaminated the measured Z-pin bridging force, due to friction between the coupon and the brass sleeve. In addition, the use of brass sleeve restricted the opening and sliding displacement of the coupons resulting in a high initial mode-mixity across all the tests. The anomalous result, i.e. large bridging force, obtained in pure mode II loading is attributed to the use of brass sleeve in the test.

- Constant velocity and hence dynamic equilibrium were not achieved during the dynamic testing of the Z-pin bridging performance.

7.1.4 Mode I Model

Two rate dependent models of the Z-pin bridging performance under mode I loading were introduced based on a peridynamic rod formulation. The first model (model 1) is capable of describing all the key stages of the Z-pin response, namely bonded stage, progressive debonding and frictional pull-out. The calibration of model 1 parameters yielded different values at different loading rates due to the presence of inertial effects in the experimental results. Thus model 1 could not be used as a universal description of the Z-pin response. Nonetheless, model 1 demonstrate the capability of a reduced-order approach to simulate all the key stages of Z-pin response. Model 1 is the first of its kind in this regard.

The second model (model 2) ignored the bonded and de-bonding stages and only considered the frictional pull-out stage. Calibration against experimental results yielded a unified set of parameter values for model 2 making it truly applicable at different loading rates. Both model 1 and 2 adapted Ruina's (Ref. [169]) state-dependent friction model to describe the rate dependent sliding frictional force.

Both models yielded excellent prediction capability with negligible difference arising from the two models in terms of the total energy absorbed by the Z-pin. Nonetheless, model 1 is in principle better suited to describe the Z-pin bridging force as a function of opening displacement, since it considered all the stages of the Z-pin response. However, performing single Z-pin tests where dynamic equilibrium conditions are attained remains an open challenge.

7.1.5 Mixed Mode Model

A rate dependent model of Z-pin bridging performance under mixed-mode loading has been developed based on a peridynamic Timoshenko beam formulation. The model considered the full set of external forces acting on a Z-pin, namely the sliding friction, snubbing friction and Winkler foundation force. The sliding and snubbing frictional forces are described using Ruina's (Ref. [169]) rate-dependent friction model. The Winkler foundation force is proportional to the relative lateral Z-pin displacement and in opposite direction, i.e. it represents a form of "punch resistance" force.

Under mixed mode loading the Z-pin fails by either complete pull-out or fracture. The developed model incorporated B-K failure criterion to predict the onset of fracture. For this purpose, closed form expressions of the mode I and II energy release rates in the peridynamic formulation were derived.

The model parameters were obtained by calibrating the model output against a subset of the available experimental results, using a genetic algorithm. The model resulted in excellent prediction of the Z-pin bridging performance at different loading rates and across different mode-mixity, except in the transition region, i.e. for nominal mixed mode angle of 15° and 30°. This was attributed to the deterministic nature of the model not being

able to capture the variability in the Z-pin performance observed across the array of 16 Z-pins in the experimental results.

The variability in the observed Z-pin response is due to uncertainty in the Z-pin misalignment angle and strength. Once the variability in the aforementioned parameters was incorporated into the model, the prediction capability was seen to significantly improve in the transition region.

7.2 Overall Conclusion

A reduced order model capable of predicting the Z-pin bridging performance under mixed-mode loading and at high loading rates is developed. The developed model is relatively accurate and computationally efficient at the same time. The model run time is of the order of minutes on a desktop computer using a non-optimised Matlab code. It is suggested to use the model as part of a multi-scale modelling approach as presented in section 7.3.

7.3 Future Work

7.3.1 Numerical

Multi-Scale Modelling Approach

It is suggested to use the reduced order model (ROM) as part of a multi-scale modelling approach to model Z-pinned laminates. This can be done by replacing the Z-pin with a nodal force or enhancing the fracture toughness of the cohesive element in the neighbourhood of the Z-pin. The ROM model can be used to obtain either the force or the enhanced fracture toughness in two ways.

The first way is to develop the code into a subroutine suitable to be run with a finite element (FE) package such as Abaqus or LS-DYNA. The subroutine can then be run concurrently with the FE package to predict the Z-pin bridging force for a given opening and sliding displacement as obtained from the FE package. The output from the subroutine can then be applied

as a nodal force acting in the location of the Z-pin. Alternatively, the output from the model can be used to obtain the enhanced fracture toughness of the Z-pin and apply it to the cohesive element.

The second way is to use the ROM model to generate bridging maps that can be interpolated from to obtain inputs for the FE package. The bridging map would have the bridging force and energy absorbed by the Z-pin for a given mode-mixity and loading rate. The ROM model allows the generation of bridging maps spanning different mode-mixities and loading rates in reasonable time scales. The bridging map can then be used to interpolate the Z-pin bridging force and apply it as a nodal force in the Z-pin laminate. Alternatively, the bridging map can be interpolated for the enhanced fracture toughness value that is applied to the cohesive zone element.

Further Development of the Current Model

The computational efficiency of the present model can be significantly improved by writing the code using Fortran or C++ languages. In addition, the code run time can be reduced by using a parallel for loop for the spatial integral in the integro-differential peridynamic equation. It is suggested to incorporate both of the aforementioned improvements when implementing the developed model.

Furthermore, it is suggested to extend the single state Ruina friction model used in this thesis into a multi-state model. The reason for this suggestion is the anticipation that a multi-state model would replace the empirical model used to simulate the sliding friction under quasi-static prediction loading while remaining applicable at high loading rates.

7.3.2 Experimental

Test Set-up

It is suggested to improve the test set-up to address the issues highlighted in this work. For this purpose, it is suggested to remove the brass sleeve from the test set-up used. The brass sleeve is thought to constrain the coupon

opening and sliding displacement causing high initial mode mixity in all tests observed. In addition, the presence of the brass sleeve causes additional friction with the coupon which can contaminate the measured bridging force.

Additionally, it is suggested to use optical image correlation to measure the coupon opening and sliding displacement close to the delamination interface of the coupon during all tests. This information would allow the actual mode mixity achieved to be calculated and hence a better characterisation of the Z-pin response as a function of the mode mixity.

Other Experimental Considerations

The experiments were conducted at either quasi-static($0.01mm/s$) or dynamic loading rates of the order of meters per second(i.e. $1000mm/s$). It is immediately clear that there is a large gap between the two test speeds with no data available. It is interesting to test whether the current calibrated model can predict the Z-pin bridging performance at this range of loading rates. Therefore, it is suggested to repeat the same experiments but with the following loading rates: $1mm/s$, $10mm/s$ and $100mm/s$.

Measuring the bridging performance of a single Z-pin under dynamic loading is very challenging with current state-of-the-art methods. It is recommended to develop new test techniques that can achieve dynamic equilibrium in short period of time and are sensitive enough to measure the bridging force of a single Z-pin. In the instant of such a test method becoming available, it is suggested to repeat the experimental tests to measure single Z-pin response instead of averaging over an array of 16 Z-pins. This allows for a clear distinction between single Z-pin response and array response.

Appendices

Appendix A

Classical Timoshenko Beam With Small Rotation

Consider a long prismatic beam of length L made of homogeneous material. The beam is collinear with the z-axis of the global zx reference frame shown in fig. A.1. Let N be the axial force normal to the rotated cross-section of the beam, while let T denote the shear resultant that lies on the cross-section. Similarly, let Z and X denote the cross-section resultants expressed in the global reference frame zx, as illustrated in fig. A.1. For a small cross-section rotation θ, the following approximated transformation holds:

$$\begin{aligned} Z &= N - T\theta, \\ X &= T + N\theta. \end{aligned} \tag{A.1}$$

Considering negligible the elongation of the beam axis (i.e. $w << L$), the virtual work performed by internal forces on the beam axis is approximately

$$\delta W_{int} = \int_0^L \left(Z\delta\epsilon_z + X\delta\gamma_{zx} + M\delta\chi\right) dz \tag{A.2}$$

where M is the bending moment acting on the beam cross-section. In eq. (A.2), ϵ_z is the direct engineering strain with respect to the z-axis and γ_{zx} is the shear strain, both expressed in global axes. Finally, $\chi := d\theta/dr$ is the curvature of the beam.

For the axial strain, the usual definition holds:

$$\epsilon_z = w^I, \tag{A.3}$$

where the Roman numeral denotes differentiation with respect to z. Let the slope of the beam axis being denoted as $\phi := du/dr$. Considering again the geometrical approximations introduced in chapter 3 (see eq. (3.13)), one has $\phi \approx u^I$ for the slope of the beam axis and $\chi \approx \theta^I$ for the curvature. Hence, for shear strain that appear in eq. (A.2) one finds:

$$\gamma_{zx} = \frac{\partial u}{\partial z} + \frac{\partial w}{\partial x} = u^I - \theta. \tag{A.4}$$

Substituting eqs. (A.1), (A.3) and (A.4) into the internal virtual work in eq. (A.2) yields:

$$\delta W_{int} = \int_0^L \left[(N - T\theta)\, \delta w^I + (T + N\theta)\, \delta \left(u^I - \theta \right) + M \delta \theta^I \right] dz \tag{A.5}$$

Integrating by parts eq. (A.5) leads to the following expression of the internal virtual work:

$$\begin{aligned} \delta W_{int} = - \int_0^L \big[\left(N^I - \theta T^I - T\theta^I \right) \delta w + \left(T^I + \theta N^I + N\theta^I \right) \delta u + \\ + \left(M^I + T + N\theta \right) \delta \theta \big]\, dz. \end{aligned} \tag{A.6}$$

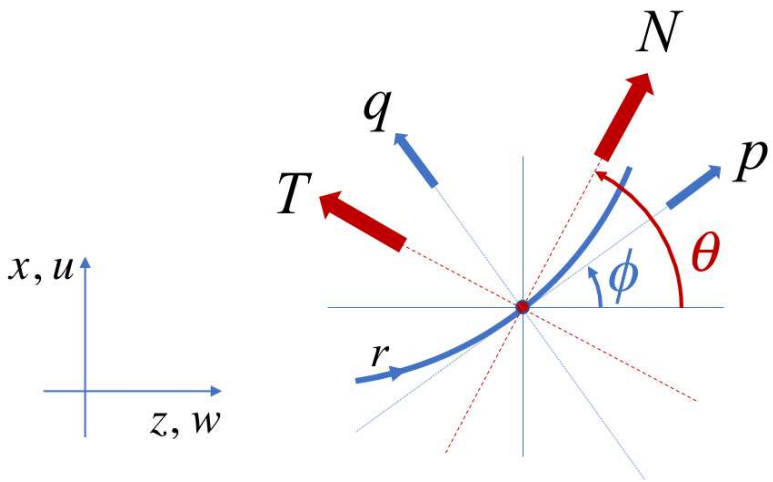


Figure A.1: Deformation and forces for a classical beam.

Similarly, the external work performed by the distributed external forces p and q shown in fig. A.1 is expressed as follows:

$$\delta W_{ext} = \int_0^L \left[(p - q\phi)\, \delta w + (q + p\phi)\, \delta u \right] dz. \tag{A.7}$$

Imposing $\delta W_{int} = \delta W_{ext}$ for any arbitrary set of virtual displacement/rotation fields $\{\delta w,\, \delta u,\, \delta\theta\}$ leads to the following set of non-linear ordinary differential equations:

$$\begin{aligned} N^I - (T\theta)^I + p - qu^I &= 0, \\ T^I + (N\theta)^I + q + pu^I &= 0, \\ M^I + T + N\theta &= 0. \end{aligned} \tag{A.8}$$

Considering a beam made of a linear elastic material, the constitutive equations read:

$$N = EAw^I, \quad T = \kappa GA\left(u^I - \theta\right), \quad M = EI\theta^I, \tag{A.9}$$

where A and I are the cross-sectional area and the second moment of area respectively; E and G are the Young's and shear moduli of the material constituting the beam, respectively. Finally, κ is the Timoshenko shear correction factor [162]. The constitutive relations from eq. (A.9) can be then substituted into the equilibrium conditions eq. (A.8). Performing the latter operation and invoking the d'Alembert's principle for the inertial forces lead to:

$$\begin{aligned} \rho A\ddot{w} &= EAw^{II} - \kappa GA\left[\theta\left(u^I - \theta\right)\right]^I + p - qu^I, \\ \rho A\ddot{u} &= \kappa GA\left(u^{II} - \theta^I\right) + EA\left(\theta w^I\right)^I + q + pu^I, \\ \rho I\ddot{\theta} &= EI\theta^{II} + \kappa GA\left(u^I - \theta\right) + EAw^I\theta. \end{aligned} \tag{A.10}$$

Eq. A.10 represents the governing equation for a Timoshenko beam with small rotation using the classical continuum mechanics formulation.

Appendix B

Riemann's Sum Approximation of Peridynamic Integrals

The expressions of the Riemann's sums that appear in eq. (3.62) are:

$$I_{ij}^{(1)} = \Delta z \sum_{j=i_1}^{i_{N_h}} v_{c(ij)} SCF_i \left[c_a \frac{w_j - w_i}{|z_j - z_i|} - c_s \left(\frac{u_j - u_i}{|z_j - z_i|} - \bar{\theta}_{ij} \frac{z_j - z_i}{|z_j - z_i|} \right) \bar{\theta}_{ij} \right],$$

$$I_{ij}^{(2)} = \Delta z \sum_{j=i_1}^{i_{N_h}} v_{c(ij)} SCF_i \left[c_s \left(\frac{u_j - u_i}{|z_j - z_i|} - \bar{\theta}_{ij} \frac{z_j - z_i}{|z_j - z_i|} \right) + c_a \frac{w_j - w_i}{|z_j - z_i|} \bar{\theta}_{ij} \right],$$

$$I_{ij}^{(3)} = \Delta z \sum_{j=i_1}^{i_{N_h}} v_{c(ij)} SCF_i \left\{ c_b \frac{\theta_j - \theta_i}{|z_j - z_i|} + \frac{1}{2} \left[c_s \left(\frac{u_j - u_i}{|z_j - z_i|} + \right. \right. \right.$$

$$\left. \left. \left. - \bar{\theta}_{ij} \frac{z_j - z_i}{|z_j - z_i|} \right) + c_a \frac{w_j - w_i}{|z_j - z_i|} \bar{\theta}_{ij} \right] (z_j - z_i) \right\}, \tag{B.1}$$

Where, $\bar{\theta}_{ij} = 1/2\,(\theta_i + \theta_j)$ is the average rotation for the i-th and j-th particles

Appendix C

Peridynamic Force at a Point

Let us consider the case where we are required to calculate the force in a peridynamic rod/beam at a given location z^*. Given a particle positioned at $z \leq z^*$, the resulting force due to the bonds originating at z and crossing the z^* point (see fig. C.1) is given by:

$$F^-(z^*) = \int_{z^*}^{z+r_h} f dz' \tag{C.1}$$

The total force at z^* is obtained by integrating $F^-(z^*)$ from eq. (C.1) for all the particles z with $z \leq z^*$, whose horizons cross z^*. Hence:

$$F(z^*) = \int_{z^*-r_h}^{z^*} \int_{z^*}^{z+r_h} f dz' dz \tag{C.2}$$

Approximating the integrals in eq. (C.2) as Riemann sums, the following equation is sought:

$$F(z^*) = \sum_{i=1}^{M^-} \sum_{j=1}^{M^+} f_{ij} \tag{C.3}$$

where the index i spans the M^- particles located at $z_i < z^*$ whose horizons cross z^*; similarly, the index j indicates the the M^+ particles with $z_j \geq z^*$ whose horizons comprise z^* .

Therefore, to calculate the axial and shear force at location z^*, the axial and shear force density is used to replace f_{ij} in eq. (C.3). The axial force density is defined as: $f_{axail} = c_a s_w$, where s_w and c_a are the axial stretch and

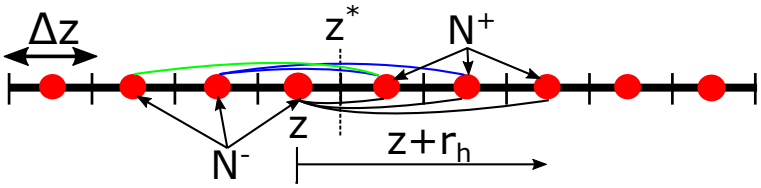


Figure C.1: Illustration for calculating bridging force across a delamination plane.

bond constant respectively and are defined in chapter 3. Thus replacing the definition into eq. (C.3), the axial force is given as:

$$F_{axial}(z^*) = 2EA\left(\frac{\Delta z}{r_h}\right)^2 \sum_{i=1}^{N^-}\sum_{j=1}^{N^+} \frac{w_j - w_i}{|z_j - z_i|} v_c(ij) SCF(i) \qquad \text{(C.4)}$$

Similarly, the shear force density is defined as: $f_{shear} = c_s s_\gamma$, where s_γ and c_s are the shear stretch and bond constant respectively and are defined in chapter 3. Thus replacing their definition into eq. (C.3), the shear force is given as:

$$F_{shear}(z^*) = 2\kappa GA\left(\frac{\Delta z}{r_h}\right)^2 \sum_{i=1}^{N^-}\sum_{j=1}^{N^+} \left[\frac{u_j - u_i}{|z_j - z_i|} - \frac{1}{2}(\theta_j + \theta_i)\frac{z_j - z_i}{|z_j - z_i|}\right] v_c(ij) SCF(i) \qquad \text{(C.5)}$$

References

[1] E. Greenhalgh. Failure analysis and fractography of polymer composites. Cambridge, UK : Woodhead Publishing ; Boca Raton, FL : CRC Press, 2009.

[2] Emile Greenhalgh and Matthew Hiley. The assessment of novel materials and processes for the impact tolerant design of stiffened composite aerospace structures, February 2003 2003. ID: 271638.

[3] K. N. Shivakumar, R. Panduranga, and M. Sharpe. Interleaved polymer matrix composites - a review. In AIAA/ASME/ASCE/AHS/ASC Structures, Structural Dynamics and Materials, 2013 2013.

[4] A. Morales. Structural stitching of textile preforms proc. 22nd int. sampe tech. conf. (6–8 nov. 1990), pp. 1217-1230. In Proc. 22nd Int. SAMPE Tech Conf., pages 1217–1230, 6-8 Nov. 1990 1990.

[5] G. Dell'Anno, J. W. G. Treiber, and I. K. Partridge. Manufacturing of composite parts reinforced through-thickness by tufting, February 2016 2016. ID: 271446.

[6] A. P. Mouritz. Review of z-pinned composite laminates. Comopsites Part A: applied science and manufacturing, (1):2383–1297, 2007.

[7] T. Kellner. These materials scientists are teaching robots awesome new tricks. Technical report, GE Reports, 2014.

[8] P. Chang. The Mechanical Properties and Failure Mechanisms of Z-Pinned Composites. PhD thesis, 2006.

[9] Roderick D. Sweeting and Rodney S. Thomson. The effect of thermal mismatch on z-pinned laminated composite structures, October–December 2004 2004. ID: 271517.

[10] D. D. R. Cartié, B. N. Cox, and N. A. Fleck. Mechanisms of crack bridging by composite and metallic rods. Composites Part A: Applied Science and Manufacturing, 35(11):1325–1336, 2004.

[11] B. Zhang, G. Allegri, M. Yasaee, and S. R. Hallett. Micro-mechanical finite element analysis of z-pins under mixed-mode loading. Composites Part A: Applied Science and Manufacturing, 78:424–435, 2015.

[12] Hao Cui, Mehdi Yasaee, Gordon Kalwak, Antonio Pellegrino, Ivana K. Partridge, Stephen R. Hallett, Giuliano Allegri, and Nik Petrinic. Bridging mechanisms of through-thickness reinforcement in dynamic mode i and ii delamination. Composites Part A: Applied Science and Manufacturing, 99:198–207, 8 2017.

[13] Hao Cui, Mehdi Yasaee, Stephen R. Hallett, Ivana K. Partridge, Giuliano Allegri, and Nik Petrinic. Dynamic bridging mechanisms of through-thickness reinforced composite laminates in mixed mode delamination, March 2018 2018. ID: 271638.

[14] Daniel Gay 1942-author. Composite Materials: Interests and Physical properties, pages 10–10. Composite materials : design and applications. CRC Press, Boca Raton, third edition, 2015.

[15] Daniel Gay 1942-author. Composite materials : design and applications. CRC Press, Boca Raton, third edition, 2015.

[16] Geoff Eckold. Design and manufacture of composite structures. Woodhead Publishing, Cambridge, 1994.

[17] L. Pilato 1934. Advanced composite materials. Springer-Verlag, Berlin, 1994.

[18] A. M. Amaro, P. N. B. Reis, and M. F. S. F. de Moura. Delamination effect on bending behaviour in carbon–epoxy composites. Strain, 47(2):203–208, 2011.

[19] P. N. B. Reis, J. A. M. Ferreira, F. V. Antunes, and M. O. W. Richardson. Effect of interlayer delamination on mechanical behavior of carbon/epoxy laminates. Journal of Composite Materials, 43(22):2609–2621, October 01 2009.

[20] K. Friedrich. Damage Mechanisms - Including Edge Effects - in Carbon Fibre-Reinforced Composite Materials, page 273. Application of Fracture Mechanics to Composite Materials. Elsevier Science, Amsterdam, 2012. ID: 1181892.

[21] Allen J. Fawcett and Gary D. Oakes. Boeing composite airframe damage tolerance and service experience.

[22] Kimberley Dransfield, Caroline Baillie, and Yiu-Wing Mai. Improving the delamination resistance of cfrp by stitching—a review. Composites Science and Technology, 50(3):305–317, 1994 1994. ID: 271518271518.

[23] L. Tong, A. P. Mouritz, and M. Bannister. 3D Fibre Reinforced Polymer Composites. Elsevier, 2002.

[24] A. P. Mouritz, M. K. Bannister, P. J. Falzon, and K. H. Leong. Review of applications for advanced three-dimensional fibre textile composites. Composites Part A: Applied Science and Manufacturing, 30(12):1445–1461, 12 1999.

[25] G. Freitas and et al. fibre insertion process for improved damage tolerance in aircraft. Journal of Advanced Materials, 25:36–43, 1994.

[26] D. D. R. Cartié and I. K. Partridge. Delamination behaviour of Z-pinned laminates, volume 27 of European Structural Integrity Society. 2000.

[27] P. Chang, A. P. Mouritz, and B. N. Cox. Properties and failure mechanisms of z-pinned laminates in monotonic and cyclic tension. Composites Part A: Applied Science and Manufacturing, 37(10):1501–1513, 2006.

[28] I. K. Partridge, D. D. R. Cartie, and T. Bonnington. Manufacture and performance of z-pinned composites. Advaced Polymeric Composites. FL: CRC Press, 2003.

[29] I. K. Partridge, D. D. R. Cartie, M. Troulis, M. Grassi, and X. Zhang. Evaluating the mechanical effectiveness of z-pinning. 2004.

[30] X. Zhang, L. Hounslow, and M. Grassi. Improvement of low-velocity impact and compression-after-impact performance by z-fibre pinning. Composites Science and Technology, 66(15):2785–2794, 2006.

[31] A. Rezai, D. Cartie, I. K. Partridge, and P. Irving. Interlaminar damage resistance of z-fibre reinforced structural cfrp. page ID 1477, 2001.

[32] D. D. R. Cartie. Effect of Z-fibres TM on the delamination behaviour of carbonfibre/epoxy laminates. PhD thesis, 2000.

[33] P. Chang, A. P. Mouritz, and B. N. Cox. Flexural properties of z-pinned laminates. Composites Part A: Applied Science and Manufacturing, 38(2):244–251, 2007.

[34] A. P. Mouritz. Compression properties of z-pinned composite laminates. Composites Science and Technology, 67(15-16):3110–3120, 2007.

[35] X. Zhang, Y. Li, Q. Chu, J. Xiao, and X. Dong. Influence of z-pins insertion pattern on in-plane compression properties of laminates. Hangkong Xuebao/Acta Aeronautica et Astronautica Sinica, 35(1):195–202, 2014.

[36] L. k. Anon. z-pins strengthen the super hornet, save weight and cost. The Integrator, (3):1–2, 2001.

[37] S. Mcbeath. Safety pins, 2001.

[38] I. K. Partridge and S. R. Hallett. Use of microfasteners to produce damage tolerant composite structures. Royal Society Philosophical Transactions, 2016.

[39] E. Greenhalgh. Characterisation of mixed-mode delamination growth in carbon fibre composites. PhD thesis, 1998.

[40] A. Davies. Fatigue life prediction of composite materials. Technical Report , DERA/ MSS/MSMA2/TR99068, 1999.

[41] E. Greenhalgh, A. Lewis, R. Bowen, and M. Grassi. Evaluation of toughening concepts at structural features in cfrp-part i: Stiffener pull-off. Composites Part A: Applied Science and Manufacturing, 37(10):1521–1535, 2006.

[42] John E. Masters. Improved impact and delamination resistance through interleafing. Mechanical and corrosion properties.Series A, Key engineering materials, 37:317–347, 1989. Cited By :78.

[43] S. Singh and I. K. Partridge. Mixed-mode fracture in an interleaved carbon-fibre/epoxy composite, 1995 1995. ID: 271518.

[44] Wen S. Chan. Delamination arrester - an adhesive inner layer in laminated composites. In ASTM Special Technical Publication, pages 176–196, 1986. Cited By :16.

[45] N. Sela, O. Ishai, and L. Banks-Sills. The effect of adhesive thickness on interlaminar fracture toughness of interleaved cfrp specimens, May 1989 1989. ID: 272911.

[46] R. F. Gibson, Y. Chen, and H. Zhao. Improvement of vibration damping capacity and fracture toughness in composite laminates by the use of polymeric interleaves. Journal of Materials and Technology, 123, 2001.

[47] F. Ozdil and L. A. Carlsson. (mode i interlaminar fracture of interleaved graphite/epoxy. Journal of Composite Materials, 26(3):432, 1992.

[48] S. H. Lee, H. Noguchi, Y-B Kim, and S-K Cheong. Effect of interleaved non-woven carbon tissue on interlaminar fracture toughness of laminated composites: Part ii - mode i. Journal of Composite Materials, 36(18):2169, 2002.

[49] S. H. Lee, H. Noguchi, Y-B Kim, and S-K Cheong. Effect of interleaved non-woven carbon tissue on interlaminar fracture toughness of laminated composites: Part i – mode ii. Journal of Composite Materials, 36(18):2153, 2002.

[50] Sunny S. Wicks, Roberto Guzman de Villoria, and Brian L. Wardle. Interlaminar and intralaminar reinforcement of composite laminates with aligned carbon nanotubes, January 2010 2010. ID: 271518.

[51] Enrique J. Garcia, Brian L. Wardle, and A. John Hart. Joining prepreg composite interfaces with aligned carbon nanotubes, June 2008 2008. ID: 271638.

[52] Sangwook Sihn, Ran Y. Kim, Wansoo Huh, Kwang-Hoon Lee, and Ajit K. Roy. Improvement of damage resistance in laminated composites with electrospun nano-interlayers, March 2008 2008. ID: 271518.

[53] Masahiro Arai, Yukihiro Noro, Koh ichi Sugimoto, and Morinobu Endo. Mode i and mode ii interlaminar fracture toughness of cfrp laminates toughened by carbon nanofiber interlayer, February 2008 2008. ID: 271518.

[54] Graham L. Warren, Luyi Sun, Viktor G. Hadjiev, Daniel Davis, Dimitris Lagoudas, and Hung-Jue Sue. B-staged epoxy/single-walled carbon nanotube nanocomposite thin films for composite reinforcement. Journal of Applied Polymer Science, 112(1):290–298, 04/05; 2019/04 2009. doi: 10.1002/app.29375; 05.

[55] Jin Zhang, Tong Lin, and Xungai Wang. Electrospun nanofibre toughened carbon/epoxy composites: Effects of polyetherketone cardo (pekc) nanofibre diameter and interlayer thickness, 15 October 2010 2010. ID: 271518.

[56] Paul Akangah, Shivalingappa Lingaiah, and Kunigal Shivakumar. Effect of nylon-66 nano-fiber interleaving on impact damage resistance of epoxy/carbon fiber composite laminates, May 2010 2010. ID: 271517.

[57] N. Sela and O. Ishai. Interlaminar fracture toughness and toughening of laminated composite materials: a review, September 1989 1989. ID: 272911.

[58] M. Yasaee, I. P. Bond, R. S. Trask, and E. S. Greenhalgh. Mode i interfacial toughening through discontinuous interleaves for damage suppression and control, January 2012 2012. ID: 271638.

[59] D. Liu. Delamination resistance in stitched and unstitched composite plates subjected to impact loading. Journal of Reinforced Plastics and Composites, 9(1):59, 1990.

[60] W. chang. Design approaches for edge delamination resistance in laminated composites. Journal of Composites, Technology and Research, 13(2):91, 1991.

[61] Lalit K. Jain and Yiu-Wing Mai. On the effect of stitching on mode i delamination toughness of laminated composites, 1994 1994. ID: 271518.

[62] A. P. Mouritz, K. H. Leong, and I. Herszberg. A review of the effect of stitching on the in-plane mechanical properties of fibre-reinforced polymer composites, 1997 1997. ID: 271638.

[63] Kimberley Dransfield, Caroline Baillie, and Yiu-Wing Mai. Improving the delamination resistance of cfrp by stitching—a review, 1994 1994. ID: 271518.

[64] C. Lee and D. Liu. Tensile strength of stitching joint in woven glass fabrics. Journal of Engineering Materials and Technology, 112(2):125, 1990.

[65] Sawyer JW. Effect of stitching on the strength of bonded composite single lap joints. AIAA Journal, 23(11):1744, 1985.

[66] L. Tong and L. K. Jain. Analysis of adhesive bonded composite lap joints with transverse stitching. Application of Composite Materials, 2:343, 1996.

[67] D. C. Jegley and W. A. Waters. Test and analysis of a stitched rfi graphite-epoxy panel with a fuel access door. Technical Report NASA-TM-108992, NAS 1.15:108992, NASA Langley Research Center, 1994.

[68] J. R. Reeder. Stitching vs. a toughened matrix: Compression strength effects. Journal of Composite Materials, 29(18):2464–2478, 1995.

[69] A. P. Mouritz, J. Gallagher, and A. A. Goodwin. Flexural strength and interlaminar shear strength of stitched grp laminates following repeated impacts, 1997 1997. ID: 271518.

[70] M. Colin de Verdiere, A. A. Skordos, M. May, and A. C. Walton. Influence of loading rate on the delamination response of untufted and tufted carbon epoxy non crimp fabric composites: Mode i, December 2012 2012. ID: 271088.

[71] M. Colin de Verdiere, A. A. Skordos, A. C. Walton, and Michael May. Influence of loading rate on the delamination response of untufted and tufted carbon epoxy non-crimp fabric composites/mode ii, December 2012 2012. ID: 271088.

[72] Giuseppe Dell'Anno, Denis D. Cartié, Ivana K. Partridge, and Amir Rezai. Exploring mechanical property balance in tufted carbon fabric/epoxy composites, November 2007 2007. ID: 271638.

[73] M. Colin de Verdiere, A. K. Pickett, A. A. Skordos, and V. Witzel. Evaluation of the mechanical and damage behaviour of tufted non crimped fabric composites using full field measurements, February 2009 2009. ID: 271518.

[74] Denis D. R. Cartié, Giuseppe Dell'Anno, Emilie Poulin, and Ivana K. Partridge. 3d reinforcement of stiffener-to-skin t-joints by z-pinning and tufting, November 2006 2006. ID: 271088.

[75] A. P. Mouritz, M. K. Bannister, P. J. Falzon, and K. H. Leong. Review of applications for advanced three-dimensional fibre textile composites. Composites Part A: Applied Science and Manufacturing, 30(12):1445–1461, 12 1999.

[76] V. I. Krasnov, V. A. Kuznetsov, and A. Yu. Automated method of transverse reinforcement of composites by short fibres. Mekh Kompozitnykh Mater, 3:449–504, 1987.

[77] V. T. Tomashevskii, V. N. Shalygin, D. A. Romanov, and S. Y. Sitnikov. Transversal reinforcement of composite materials using ultrasonic vibrations. Mekh Kompozitnykh Mater, 6:1068–1071, 1987.

[78] Joseph BOYCE S., Glenn FREITAS A., Constance MAGEE L., Thomas FUSCO M., John HARRIS J., and Edward KUNKLE. Ultrasonic fastening system and method, 09/07/1998 1998.

[79] J. K. Lander. Method of providing through-thickness reinforcement of a laminated material, 2012.

[80] Craig A. Steeves and Norman A. Fleck. In-plane properties of composite laminates with through-thickness pin reinforcement, May 2006 2006. ID: 271891.

[81] K. H. Leong, S. Ramakrishna, Z. M. Huang, and G. A. Bibo. The potential of knitting for engineering composites—a review, March 2000 2000. ID: 271638.

[82] G. L. Farley and L. C. Dickinson. Removal of surface loop from stitched composites can improve compression and compression-after-impact strengths. Journal of Reinforced Plastics and Composites, 11(6):633–642, 1992.

[83] M. Yasaee, J. K. Lander, G. Allegri, and S. R. Hallett. Experimental characterisation of mixed mode traction–displacement relationships for a single carbon composite z-pin. Composites Science and Technology, 94:123–131, 4/9 2014.

[84] B. N. Cox. Snubbing effects in the pullout of a fibrous rod from a laminate. Mechanics of Advanced Materials and Structures, 12(2):85–98, 03/01 2005. doi: 10.1080/15376490490493899.

[85] Mehdi Yasaee, Lawrence Bigg, Galal Mohamed, and Stephen R. Hallett. Influence of z-pin embedded length on the interlaminar traction response of multi-directional composite laminates, 5 February 2017 2017. ID: 313059.

[86] K. Pingkarawat and A. P. Mouritz. Comparative study of metal and composite z-pins for delamination fracture and fatigue strengthening of composites, March 2016 2016. ID: 271088.

[87] Beene M'membe, Mehdi Yasaee, Stephen R. Hallett, and Ivana K. Partridge. Effective use of metallic z-pins for composites' through-thickness reinforcement, 3 May 2019 2019. ID: 271518.

[88] Hun Ji, Jin-Hwe Kweon, and Jin-Ho Choi. Fatigue characteristics of stainless steel pin-reinforced composite hat joints, February 2014 2014. ID: 271517.

[89] Myung-Gyun Ko, Jin-Hwe Kweon, and Jin-Ho Choi. Fatigue characteristics of jagged pin-reinforced composite single-lap joints in hygrothermal environments, January 2015 2015. ID: 271517.

[90] Hong-Yuan Liu, Wenyi Yan, Xiao-Yan Yu, and Yiu-Wing Mai. Experimental study on effect of loading rate on mode i delamination of z-pin reinforced laminates, June 2007 2007. ID: 271518.

[91] B. N. Cox. Constitutive model for a fiber tow bridging a delamination crack. Mechanics of Composite Materials and Structures, 6:117–118, 1999.

[92] B. N. Cox and N. Sridhar. A traction law for inclined fiber tows bridging mixed-mode cracks. Mechanics of Advanced Materials and Structures, 9(4):299–331, 2002.

[93] L. C. Dickinson, G. L. Farley, and M. K. Hinders. Translaminar reinforced composites: A review. Journal of Composites Technology & Research, 21(1):3–15, 1999.

[94] Kimberley A. Dransfield, Laut K. Jain, and Yiu-Wing Mai. On the effects of stitching in cfrps—i. mode i delamination toughness, 1998 1998. ID: 271518.

[95] K. P. Plain and L. Tong. Traction law for inclined through-thickness reinforcement using a geometrical approach. Composite Structures, 88(4):558–569, 2009.

[96] L. Tong and X. Sun. Bending effect of through-thickness reinforcement rods on mode i delamination toughness of dcb specimen. i. linearly elastic and rigid-perfectly plastic models. International Journal of Solids and Structures, 41(24-25):6831–6852, 2004.

[97] L. Tong and X. Sun. Bending effect of through-thickness reinforcement rods on mode ii delamination toughness of enf specimen: Elastic and rigid-perfectly plastic analyses. Composites Part A: Applied Science and Manufacturing, 38(2):323–336, 2007.

[98] F. Bianchi and X. Zhang. Predicting mode-ii delamination suppression in z-pinned laminates. Composites Sci.Technol., 72(8):924–932, 2012.

[99] G. Allegri, M. Yasaee, I. K. Partridge, and S. R. Hallett. A novel model of delamination bridging via z-pins in composite laminates. International Journal of Solids and Structures, 51(19–20):3314–3332, 10/1 2014.

[100] Xi Zhang, Hong-Yuan Liu, Yiu-Wing Mai, and Xiao-Xue Diao. On steady-state fibre pull-outi the stress field, November 1999 1999. ID: 271518.

[101] Hong-Yuan Liu, Xi Zhang, Yiu-Wing Mai, and Xiao-Xue Diao. On steady-state fibre pull-outii computer simulation, November 1999 1999. ID: 271518.

[102] J. R. Rice and A. L. Ruina. Stability of steady frictional slipping. Journal of Applied Mechanics, 50:343–349, 1983.

[103] J. G. Ratcliffe and T. K. O'Brien. Discrete spring model for predicting delamination growth in z-fiber reinforced dcb specimens. Technical Report NASA/TM-2004-213019, ARL-TR-3190, 2004.

[104] L. W. Byrd and V. Birman. Effectiveness of z-pins in preventing delamination of co-cured composite joints on the example of a double cantilever test. Composites Part B: Engineering, 37(4-5):365–378, 2006.

[105] P. Robinson and S. Das. Mode i dcb testing of composite laminates reinforced with z-direction pins: a simple model for the investigation of data reduction strategies, February 2004 2004. ID: 271088.

[106] M. C. Song, B. V. Sankar, G. Subhash, and C. F. Yen. Analysis of mode i delamination of z-pinned composites using a non-dimensional analytical model. Composites Part B: Engineering, 43(4):1776–1784, 2012.

[107] M. Meo, F. Achard, and M. Grassi. Finite element modelling of bridging micromechanics in through-thickness reinfroced composite laminates. Composite Structures, 3-4(71):383–387, 2005.

[108] H. Cui, Yulong Li, S. Koussios, L. Zu, and A. Beukers. Bridging micromechanisms of z-pin in mixed mode delamination. Composite Structures, 93(11):2685–2695, 10 2011.

[109] I. K. Partridge and D. D. R. Cartié. Delamination resistant laminates by z-fiber® pinning: Part i manufacture and fracture performance. Composites Part A: Applied Science and Manufacturing, 36(1):55–64, 2005.

[110] D. D. R. Cartié, M. Troulis, and I. K. Partridge. Delamination of z-pinned carbon fibre reinforced laminates. Composites Science and Technology, 66(6):855–861, 2006.

[111] D. D. R. Cartié, G. Dell'Anno, E. Poulin, and I. K. Partridge. 3d reinforcement of stiffener-to-skin t-joints by z-pinning and tufting. Engineering Fracture Mechanics, 73(16):2532–2540, 2006.

[112] M. Grassi and X. Zhang. Finite element analyses of mode i interlaminar delamination in z-fibre reinforced composite laminates. Composites Science and Technology, 63(12):1815–1832, 2003.

[113] G. Allegri and X. Zhang. On the delamination and debond suppression in structural joints by z-fibre pinning. Composites Part A: Applied Science and Manufacturing, 38(4):1107–1115, 2007.

[114] Wenyi Yan, Hong-Yuan Liu, and Yiu-Wing Mai. Numerical study on the mode i delamination toughness of z-pinned laminates. Composites Science and Technology, 63(10):1481–1493, 8 2003.

[115] Wenyi Yan, Hong-Yuan Liu, and Yiu-Wing Mai. Mode ii delamination toughness of z-pinned laminates. Composites Science and Technology, 64(13–14):1937–1945, 10 2004.

[116] Venkata Dantuluri, Spandan Maiti, Philippe H. Geubelle, Rakesh Patel, and Hakan Kilic. Cohesive modeling of delamination in z-pin reinforced composite laminates. Composites Science and Technology, 67(3–4):616–631, 3 2007.

[117] Sergii Kravchenko, Oleksandr Kravchenko, Mathias Wortmann, Martin Pietrek, Peter Horst, and R. Byron Pipes. Composite toughness enhancement with interlaminar reinforcement. Composites Part A: Applied Science and Manufacturing, 54:98–106, 11 2013.

[118] Francesco Bianchi and Xiang Zhang. A cohesive zone model for predicting delamination suppression in z-pinned laminates. Composites Science and Technology, 71(16):1898–1907, 11/14 2011.

[119] Galal Mohamed, Giuliano Allegri, Mehdi Yasaee, and Stephen R. Hallett. Cohesive element formulation for z-pin delamination bridging in fibre reinforced laminates, February 2018 2018. ID: 271891.

[120] F. Baber, V. Ranatunga, and I. Guven. Peridynamic modeling of low-velocity impact damage in laminated composites reinforced with z-pins. Journal of Composite Materials, 52(25):3491–3508, 2018.

[121] A. Cemal Eringen. Nonlocal polar elastic continua, January 1972 1972. ID: 271480.

[122] A. Cemal Eringen and D. G. B. Edelen. On nonlocal elasticity, March 1972 1972. ID: 271480.

[123] I. A. Kunin. On foundations of the theory of elastic media with microstructure, 1984 1984. ID: 271480.

[124] Dominik Rogula. Non-classical material continua, 1985 1985. ID: 304402.

[125] S. A. Silling. Reformulation of elasticity theory for discontinuities and long-range forces, January 2000 2000. ID: 271504.

[126] S. A. Silling, M. Epton, O. Weckner, J. Xu, and E. Askari. Peridynamic states and constitutive modeling. Journal of Elasticity, 88(2):151–184, 2007. Cited By :568.

[127] S. A. Silling and F. Bobaru. Peridynamic modeling of membranes and fibers, March–April 2005 2005. ID: 271594.

[128] John A. Mitchell. A nonlocal, ordinary, state-based plasticity model for peridynamics. Technical Report SAND2011-3166, Sandia National Laboratories, 2011.

[129] B. Killic. Peridynamic theory for progressive failure prediction in homogeneous and heterogeneous materials. PhD thesis, 2008.

[130] John A. Mitchell. A non-local, ordinary-state-based viscoelasticity model for peridynamics. Technical Report SAND2011-8064, Sandia National Laboratories, 2011.

[131] M. J. Taylor. Numerical simulation of thermo-elasticity, inelasticity and rupture in membrane theory. PhD thesis, 2008.

[132] J. T. Foster, S. A. Silling, and W. W. Chen. Viscoplasticity using peridynamics. International Journal for Numerical Methods in Engineering, 81(10):1242–1258, 2010. Cited By :117.

[133] F. Bobaru and W. Hu. The meaning, selection, and use of the peridynamic horizon and its relation to crack branching in brittle materials. International Journal of Fracture, 176(2):215–222, 2012. Cited By :68.

[134] S. A. Silling and E. Askari. A meshfree method based on the peridynamic model of solid mechanics. Computers and Structures, 83(17-18):1526–1535, 2005. Cited By :650.

[135] E. Madenci and E. Oterkus. Peridynamic Theory and Its Applications. Springer, New York, NY, 2014.

[136] S. A. Silling, M. Zimmermann, and R. Abeyaratne. Deformation of a peridynamic bar. Journal of Elasticity, 73(1-3):173–190, 2003. Cited By :156.

[137] M. Polleschi. Stability and applications of the peridynamic method. PhD thesis, 2010.

[138] F. Bobaru, M. Yang, L. F. Alves, S. A. Silling, E. Askari, and J. Xu. Convergence, adaptive refinement, and scaling in 1d peridynamics. International Journal for Numerical Methods in Engineering, 77(6):852–877, 2009. Cited By :173.

[139] F. Bobaru and Y. D. Ha. Adaptive refinement and multiscale modeling in 2d peridynamics. International Journal for Multiscale Computational Engineering, 9(6):635–659, 2011. Cited By :78.

[140] K. Yu, X. J. Xin, and K. B. Lease. A new adaptive integration method for the peridynamic theory. Modelling and Simulation in Materials Science and Engineering, 19(4), 2011. Cited By :14.

[141] P. Seleson, S. Beneddine, and S. Prudhomme. A force-based coupling scheme for peridynamics and classical elasticity. Computational Materials Science, 66:34–49, 2013. Cited By :60.

[142] G. Lubineau, Y. Azdoud, F. Han, C. Rey, and A. Askari. A morphing strategy to couple non-local to local continuum mechanics. Journal of the Mechanics and Physics of Solids, 60(6):1088–1102, 2012. Cited By :60.

[143] W. Liu and J. W Hong. A coupling approach of discretized peridynamics with finite element method. Computer Methods in Applied Mechanics and Engineering, 245-246:163–175, 2012. Cited By :59.

[144] E. Oterkus, E. Madenci, O. Weckner, S. Silling, P. Bogert, and A. Tessler. Combined finite element and peridynamic analyses for predicting failure in a stiffened composite curved panel with a central slot. Composite Structures, 94(3):839–850, 2012. Cited By :87.

[145] B. Kilic and E. Madenci. An adaptive dynamic relaxation method for quasi-static simulations using the peridynamic theory. Theoretical and Applied Fracture Mechanics, 53(3):194–204, 2010. Cited By :97.

[146] J. T. Foster, S. A. Silling, and W. Chen. An energy based failure criterion for use with peridynamic states. International Journal for Multiscale Computational Engineering, 9(6):675–687, 2011. Cited By :58.

[147] Y. D. Ha and F. Bobaru. Characteristics of dynamic brittle fracture captured with peridynamics. Engineering Fracture Mechanics, 78(6):1156–1168, 2011. Cited By :151.

[148] P. N. Demmie and S. A. Silling. An approach to modeling extreme loading of structures using peridynamics. Journal of Mechanics of Materials and Structures, 2(10):1921–1945, 2007. Cited By :35.

[149] E. Askari, J. Xu, and S. Silling. Peridynamic analysis of damage and failure in composites. In Collection of Technical Papers - 44th AIAA Aerospace Sciences Meeting, volume 2, pages 1123–1134, 2006. Cited By :71.

[150] J. Xu, A. Askari, O. Weckner, and S. Silling. Peridynamic analysis of impact damage in composite laminates. Journal of Aerospace Engineering, 21(3):187–194, 2008. Cited By :88.

[151] A. Askari, K. Nelson, O. Weckner, J. Xu, and S. Silling. Hail impact characteristics of a hybrid material by advanced analysis techniques and testing. Journal of Aerospace Engineering, 24(2):210–217, 2011. Cited By :14.

[152] W. Hu, Y. D. Ha, and F. Bobaru. Peridynamic model for dynamic fracture in unidirectional fiber-reinforced composites. Computer Methods in Applied Mechanics and Engineering, 217-220:247–261, 2012. Cited By :114.

[153] E. Oterkus, A. Barut, and E. Madenci. Damage growth prediction from loaded composite fastener holes by using peridynamic theory. In Collection of Technical Papers - AIAA/ASME/ASCE/AHS/ASC Structures, Structural Dynamics and Materials Conference, 2010. Cited By :14.

[154] J. Xu, A. Askari, O. Weckner, H. Razi, and S. Silling. Damage and failure analysis of composite laminates under biaxial loads. In Collection of Technical Papers - AIAA/ASME/ASCE/AHS/ASC Structures, Structural Dynamics and Materials Conference, volume 7, pages 7450–7458, 2007. Cited By :37.

[155] B. Kilic, A. Agwai, and E. Madenci. Peridynamic theory for progressive damage prediction in center-cracked composite laminates. Composite Structures, 90(2):141–151, 2009. Cited By :128.

[156] C. Diyaroglu, E. Oterkus, S. Oterkus, and E. Madenci. Peridynamics for bending of beams and plates with transverse shear deformation, September 2015 2015. ID: 271891.

[157] Cong Tien Nguyen and Selda Oterkus. Peridynamics formulation for beam structures to predict damage in offshore structures, 1 February 2019 2019. ID: 271462.

[158] Richard W. Macek and Stewart A. Silling. Peridynamics via finite element analysis, November 2007 2007. ID: 271101.

[159] Philip Underwood. DYNAMIC RELAXATION., pages 245–265. Comput Methods for Transient Anal. 1983. Cited By :202.

[160] B. Kilic and E. Madenci. An adaptive dynamic relaxation method for quasi-static simulations using the peridynamic theory. Theoretical and Applied Fracture Mechanics, 53(3):194–204, 2010. Cited By :98.

[161] V. V. Nishawala and M. Ostoja-Starzewski. Peristatic solutions for finite one- and two-dimensional systems. Mathematics and Mechanics of Solids, 22(8):1639–1653, 2017.

[162] S. P. Timoshenko. On the transverse vibrations of bars of uniform cross-section. The London, Edinburgh, and Dublin Philosophical Magazine and Journal of Science, 43:253:125–131, 1922.

[163] P. Chang, A. P. Mouritz, and B. N. Cox. Properties and failure mechanisms of z-pinned laminates in monotonic and cyclic tension, October 2006 2006. ID: 271638.

[164] Y. Mahadik. Personal communication between mr. hussein hijazi and dr yusuf mahadik at university of bristol., 15/02/2019.

[165] Robert Gerlach, Christian Kettenbeil, and Nik Petrinic. A new split hopkinson tensile bar design, December 2012 2012. ID: 271452.

[166] M. M. Fert. AN INVESTIGATION OF THE MECHANICAL PERFORMANCE OF Z-PIN REINFORCED COMPOSITES. PhD thesis, 2016.

[167] Denis D. R. Cartié, Manos Troulis, and Ivana K. Partridge. Delamination of z-pinned carbon fibre reinforced laminates, May 2006 2006. ID: 271518.

[168] Y. Zhou, D. Jiang, and Y. Xia. Tensile mechanical behavior of t300 and m40j fiber bundles at different strain rate. Journal of Materials Science, 36(4):919–922, 2001.

[169] A. Ruina. Slip instability and state variable friction laws. Journal of Geophysical Research, 88:10359–10370, 1983.

[170] M. L. Benzeggagh and M. Kenane. Measurement of mixed-mode delamination fracture toughness of unidirectional glass/epoxy composites with mixed-mode bending apparatus, 1996 1996. ID: 271518.

[171] S. T. Pinho, P. Robinson, and L. Iannucci. Fracture toughness of the tensile and compressive fibre failure modes in laminated composites, October 2006 2006. ID: 271518.

[172] M. J. Laffan. Development of translaminar fracture toughness testing methods for composite materials. PhD thesis, 2011.